

HYDROUS COBALT-IRIDIUM OXIDE TWO-DIMENSIONAL NANOFRAMES AS  
HIGH ACTIVITY AND STABILITY ACIDIC OXYGEN EVOLUTION CATALYSTS

by

Yuanfang Ying, M.S.

A dissertation submitted to the Graduate Council of  
Texas State University in partial fulfillment  
of the requirements for the degree of  
Doctor of Philosophy  
Materials Science, Engineering, and Commercialization  
August 2020

Committee Members:

Christopher P. Rhodes, Chair

Jennifer Irvin

Benjamin Martin

Gary Beall

Craig Hanks

**COPYRIGHT**

by

Yuanfang Ying

2020

## **FAIR USE AND AUTHOR'S PERMISSION STATEMENT**

### **Fair Use**

This work is protected by the Copyright Laws of the United States (Public Law 94-553, section 107). Consistent with fair use as defined in the Copyright Laws, brief quotations from this material are allowed with proper acknowledgement. Use of this material for financial gain without the author's express written permission is not allowed.

### **Duplication Permission**

As the copyright holder of this work I, Yuanfang Ying, refuse permission to copy in excess of the "Fair Use" exemption without my written permission.

## **ACKNOWLEDGEMENTS**

This work was supported by Office of Naval Research (N00014-19-1-2071). The author would like to thank to Dr. Fernando Godinez-Salomon and Dr. Christopher P. Rhodes who contributed to this work. Dissertation committee members to be recognized for significant constructive input are Dr. Benjamin Martin, Dr. Jennifer Irvin, Dr. Gary Beall, Dr. Craig Hanks and most of all Dr. Christopher P. Rhodes.

## TABLE OF CONTENTS

	<b>Page</b>
ACKNOWLEDGEMENTS .....	iv
LIST OF TABLES .....	vii
LIST OF FIGURES .....	viii
LIST OF ABBREVIATIONS .....	xii
ABSTRACT .....	xiv
CHAPTER	
I. INTRODUCTION .....	1
1.1. Hydrogen – A Renewable Energy .....	1
1.1.1. Hydrogen Resource Status and Challenge .....	1
1.1.2. Proton Exchange Membrane Water Electrolyzer: Background and Research Needs .....	2
1.2. Oxygen Evolution Reaction in Acid Electrolyte .....	3
1.3. Electrocatalysts for Oxygen Evolution Reaction.....	5
1.3.1. Ruthenium, Iridium, Ruthenium Oxide and Iridium Oxide Catalysts .....	5
1.3.2. Supported Iridium Catalysts.....	7
1.3.3. Iridium-Non-noble Transition Metal Catalysts .....	9
1.3.4. Two-Dimensional (2D) Iridium Alloys.....	13
1.3.5. Prior Work on Cobalt-Iridium Catalysts .....	14
1.4. Effect of Temperature Treatment on Iridium-based Catalysts .....	17
1.5. Project Motivation and Objectives .....	23
1.6. Principles of Experimental Methods Utilized .....	26
1.6.1. X-ray Diffraction Characterization .....	26
1.6.2. Rotating Disk Electrode Measurement .....	26
1.6.3. Cyclic Voltammetry .....	28
1.6.4. Carbon Monoxide Stripping.....	28
1.6.5. Pseudocapacitance Measurements .....	29
1.6.6. Tafel Plots .....	30
II. EXPERIMENTAL METHODS.....	32

2.1. Chemicals .....	32
2.2. Material Synthesis .....	32
2.3. Physical and Structural Characterization.....	34
2.4. Electrochemical Characterization.....	35
III. RESULTS AND DISCUSSION.....	38
3.1. Overview of Synthesis Approach.....	38
3.2. Characterization of cobalt-iridium electrocatalyst and precursor materials ...	39
3.2.1. Analysis of the morphology, surface area and elemental composition of cobalt-iridium catalyst and precursor materials.....	39
3.2.2. X-ray Diffraction Characterization of cobalt-iridium catalyst and precursor materials.....	47
3.2.3. Infrared Spectroscopic Characterization of cobalt-iridium catalyst and precursor material .....	49
3.2.4. Characterization of CoIr300-CL Using Cyclic Voltammetry and Carbon Monoxide Stripping Voltammetry .....	51
3.2.5. Evaluation of Electrochemical Oxygen Evolution Activity and Stability of CoIr300-CL .....	54
3.3. Effect of heat treatment temperature on catalytic activity and stability of cobalt-iridium oxygen evolution reaction electrocatalyst .....	63
3.3.1. Analysis of the morphology, porosity and elemental composition of heat-treated precursors and catalysts. ....	63
3.3.2. X-ray Diffraction Characterization of heat-treated precursors and catalysts.....	70
3.3.3. Characterization of Catalysts Using Cyclic Voltammetry and Carbon Monoxide Stripping Voltammetry .....	74
3.3.4. Evaluation Electrochemical Oxygen Evolution Activity of Cobalt-iridium nanoframes Catalysts .....	78
3.3.5. Evaluation Electrochemical Oxygen Evolution Stability of Cobalt-iridium nanoframes Catalysts .....	83
IV. CONCLUTIONS .....	95
V. FUTURE RESEARCH DIRECTIONS .....	98
LITERATURE CITED.....	99

## LIST OF TABLES

Table	Page
1. Average Brunauer-Emmett-Teller (BET) surface areas, cumulative pore volumes, and mean pore diameters of precursors and catalyst materials.....	43
2. Inductively Coupled Plasma Mass Spectrometry (ICP-MS) analysis of iridium in electrolytes after electrochemical oxidation (EO) and after accelerated durability testing (ADT) of CoIr300-CL and commercial IrO <sub>2</sub> . ....	61
3. Comparison of electrode loadings and oxygen evolution reaction (OER) mass activities (normalized for mass of Ir) at 1.51 V <sub>RHE</sub> and 1.55 V <sub>RHE</sub> for electrocatalysts tested in this study and previously reported values. ....	62
4. Average Brunauer-Emmett-Teller (BET) surface areas, cumulative pore volumes, and mean pore diameters of precursors. ....	65
5. Relative elemental composition and ratios of Ir and Co within catalysts determined by Energy Dispersive x-ray Spectroscopy (EDS).....	70
6. Summary of Peak Positions and Crystallographic Parameters of CoIr200-CL, CoIr300-CL, CoIr400-CL and Reference Standards Obtained from the Crystallography Open Database (COD). ....	73
7. Comparison of Tafel slopes of CoIr200-CL, CoIr300-CL and CoIr400-CL after electrochemical oxidation (EO) and after accelerated durability testing (ADT)..	86
8. Inductively Coupled Plasma Mass Spectrometry (ICP-MS) analysis of iridium from CoIr200-CL, CoIr300-CL and CoIr400-CL in electrolytes after electrochemical oxidation (EO) and after accelerated durability testing (ADT). ....	93
9. Comparison of electrochemical surface areas (ECSA), oxygen evolution reaction (OER) mass activities, and OER specific activities of IrO <sub>2</sub> -AA (Alfa Aesar), CoIr200-CL <sub>EO</sub> , CoIr300-CL <sub>EO</sub> and CoIr400-CL <sub>EO</sub> .....	94

## LIST OF FIGURES

Figure	Page
1. Wind/electrolysis System.....	2
2. Schematic of the operating principle of a proton exchange membrane (PEM) electrolysis cell.....	3
3. Schematic illustrate of the Gibbs free energy of the reactive species and intermediates in the four steps of oxygen evolution reaction.....	5
4. OER performance in form of overpotential and metal dissolution rates at $5 \text{ mAcm}^{-2}$ geometric current density of different metal electrodes. ....	6
5. Constant current stability test of $\text{IrO}_x/\text{ATO}$ , $\text{IrO}_x/\text{C}$ and $\text{IrO}_x/\text{Commercial ATO}$ electrocatalysts for OER. ....	9
6. Schematic illustration of reaction paths for OER, indicating alloying iridium with nickel and/or cobalt leads to the barrier of reaction path decreasing.....	12
7. Scanning electron microscopy (SEM) image (A), and tomography high-angle annular dark-field scanning transmission electron microscopy (HAADF-STEM) image (B) of the hydrous iridium-nickel oxide. ....	14
8. XRD patterns of the Ir-Co nanowires with different Ir composition (wt. % Ir). ....	16
9. Comparison of specific activity, mass activity and electrochemical surface area of iridium-nickel, iridium-cobalt, metallic iridium and iridium oxide as oxygen evolution reaction electrocatalyst. ....	17
10. OER performance of thin-film Ir oxide model catalysts in form of overpotential and Ir dissolution as a function of the calcination temperature.....	18
11. Schematic models describing the segregation of Pt and Ni atoms in octahedral $\text{Pt}_{0.5}\text{Ni}_{0.5}$ NPs (a) as-prepared and after annealing from 25 to $500^\circ\text{C}$ in the following $\text{H}_2$ (1 bar). ....	19
12. XRD patterns of the $\text{IrO}_2\text{-Ta}_2\text{O}_5$ electrodes calcined at three different temperatures compare with standard PDF of Ti, rutile $\text{IrO}_2$ and rutile $\text{TiO}_2$ .....	20

13. Polarization curves (A), and lifetime (black square) and Ir loss rate during accelerated lifetime tests (blue triangle) (B) of the IrO <sub>2</sub> -Ta <sub>2</sub> O <sub>5</sub> catalysts calcined at different temperatures. ....	22
14. Solution movement caused by rotation of an RDE.....	27
15. Schematic layout of the experimental steps for the synthesis of two-dimensional (2D) cobalt – iridium nanoframe catalysts. ....	39
16. Representative secondary electron images obtained by scanning electron microscopy (SEM) of Co(OH) <sub>2</sub> nanosheet precursor (A), as-prepared Co(OH) <sub>2</sub> :Ir (B), after thermal treatment under H <sub>2</sub> /Ar at 300 °C (CoIr300) (C), and CoIr300-CL after chemical leaching(D). ....	41
17. Isotherm (A) and pore-size distribution (PSD) plot (B) of CoIr300-CL obtained from nitrogen physisorption. ....	42
18. Scanning electron microscopy (SEM) images and energy-dispersive x-ray spectroscopy (EDS) mapping analysis of Co(OH) <sub>2</sub> :Ir (A-D) and CoIr (E-H) showing iridium, cobalt, and oxygen within the structures. ....	44
19. Scanning electron microscopy (SEM) images and energy-dispersive x-ray spectroscopy (EDS) mapping analysis of CoIr300-CL showing iridium, cobalt, and oxygen within the structure. ....	45
20. Low-magnification (A) and high resolution (B) HAADF-STEM images of CoIr300-CL catalyst; the yellow square indicates the HAADF-STEM intensity profile and remarks the interplanar distance associated with (111) lattice plane (C); FFT pattern (D). ....	46
21. X-ray diffraction (XRD) patterns of as-prepared catalysts and their corresponding references: α-Co(OH) <sub>2</sub> , Co <sub>3</sub> O <sub>4</sub> , Co, and Ir. ....	49
22. Transmission Fourier-transform infrared spectra (FT-IR) of (a) CoIr300; and (b) CoIr300-CL obtained using KBr pellets. ....	50
23. Initial and after electrochemical oxidation cyclic voltammograms (CVs) of CoIr-CL (A) and (B) carbon monoxide (CO) stripping voltammetry of CoIr300-CL. ....	52

24. Cyclic voltammetry (CV) scans after Au-disk background correction of CoIr300-CL <sub>EO</sub> and commercial IrO <sub>2,EO</sub> . .....	53
25. Current in the oxygen evolution reaction (OER) voltage region determined from chronoamperometry measurements of CoIr300-CL <sub>EO</sub> and commercial IrO <sub>2,EO</sub> before and accelerated durability testing in O <sub>2</sub> -free 0.1 M HClO <sub>4</sub> . .....	55
26. Cyclic voltammetry (CV) scans after Au-disk background correction of CoIr300-CL <sub>EO</sub> before and after accelerated durability testing used to determine pseudocapacitive charge. ....	56
27. Tafel slopes before and after accelerated durability testing determined by chronoamperometry. ....	57
28. Comparison of OER mass activities at 1.51 V <sub>RHE</sub> before and after accelerated durability testing (A); and comparison of OER specific activities at 1.51 V <sub>RHE</sub> before and after accelerated durability testing (B). ....	60
29. Scanning electron microscopy (SEM) images of thermal and chemical treated materials CoIr200(A), CoIr300(B), CoIr400(C), CoIr200-CL(D), CoIr300-CL(E) and CoIr400-CL(F). ....	64
30. Nitrogen physisorption isotherm and pore-size distribution plot of CoIr200 (A-B), CoIr300 (C-D), CoIr400 (E-F). ....	66
31. Scanning electron microscopy (SEM) images and energy-dispersive x-ray spectroscopy (EDS) mapping analysis of CoIr200 (A-D); CoIr300 (E-H); CoIr400 (I-L), showing iridium, cobalt, and oxygen within the structures. ....	67
32. Scanning electron microscopy (SEM) images and energy-dispersive x-ray spectroscopy (EDS) mapping analysis of CoIr200-CL (A-D); CoIr300-CL (E-H); CoIr400-CL (I-L), showing iridium, cobalt, and oxygen within the structures....	69
33. X-ray diffraction (XRD) patterns of CoIr materials after different thermal and chemical treatments (CoIr200, CoIr300, CoIr400, CoIr200-CL, CoIr300-CL, CoIr400-CL and their corresponding references: Co <sub>3</sub> O <sub>4</sub> , Co, and Ir). ....	72
34. Initial cyclic voltammograms (CVs) of CoIr200-CL, CoIr300-CL and CoIr400-CL (A); CO Stripping of CoIr200-CL, CoIr300-CL, CoIr400-CL (B). ....	76

35. Cyclic voltammetry (CV) scans of CoIr200-CL <sub>EO</sub> , CoIr300-CL <sub>EO</sub> , CoIr400-CL <sub>EO</sub> and commercial IrO <sub>2,EO</sub> .....	77
36. Cyclic voltammetric (CV) scans after Au-disk background correction of CoIr200-CL <sub>EO</sub> , CoIr300-CL <sub>EO</sub> and CoIr400-CL <sub>EO</sub> used to determine pseudocapacitive charge.....	78
37. Current in the oxygen evolution reaction (OER) voltage region determined from chronoamperometry measurements of CoIr200-CL <sub>EO</sub> , CoIr300-CL <sub>EO</sub> , CoIr400-CL <sub>EO</sub> and commercial IrO <sub>2</sub> after electrochemical oxidation in O <sub>2</sub> -free 0.1 M HClO <sub>4</sub> .....	79
38. Tafel slopes determined by chronoamperometry.....	81
39. Comparison of OER mass activities treated with different temperatures at 1.51 V <sub>RHE</sub> (A); comparison of OER specific activities treated with different temperatures at 1.51 V <sub>RHE</sub> (B).....	83
40. Current in the oxygen evolution reaction (OER) voltage region determined from chronoamperometry measurements of CoIr200-CL <sub>EO</sub> , CoIr300-CL <sub>EO</sub> , CoIr400-CL <sub>EO</sub> and commercial IrO <sub>2</sub> before and accelerated durability testing in O <sub>2</sub> -free 0.1 M HClO <sub>4</sub> .....	84
41. Tafel slopes before and after accelerated durability testing determined by chronoamperometry.....	85
42. Comparison of OER mass activities at 1.51 V <sub>RHE</sub> before and after accelerated durability testing (A); comparison of OER specific activities at 1.51 V <sub>RHE</sub> before and after accelerated durability testing (B).....	88
43. Cyclic voltammetric (CV) scans after Au-disk background correction of CoIr200-CL <sub>ADT</sub> , CoIr300-CL <sub>ADT</sub> , CoIr400-CL <sub>ADT</sub> used to determine pseudocapacitive charge.....	90
44. Comparison of cyclic voltammetry (CV) scans of CoIr200-CL <sub>EO</sub> and CoIr200-CL <sub>ADT</sub> (A); CoIr300-CL <sub>EO</sub> and CoIr300-CL <sub>ADT</sub> (B); CoIr400-CL <sub>EO</sub> and CoIr400-CL <sub>ADT</sub> (C).....	92

## LIST OF ABBREVIATIONS

<b>Abbreviation</b>	<b>Description</b>
PEMWE	Proton exchange membrane water electrolysis
OER	Oxygen evolution reaction
2D	Two-dimensional
EG	Ethylene glycol
BET	Brunauer–Emmett–Teller
RDE	Rotating disk electrode
CV	Cyclic voltammetry
CO stripping	Carbon monoxide stripping
XRD	X-ray powder diffraction
FTIR	Fourier-transform infrared spectroscopy
SEM	Scanning electron microscope
EDS	Energy Dispersive X-ray Spectroscopy
TEM	Transmission electron microscopy
ICP-MS	Inductively coupled plasma mass spectroscopy
RDE	Rotating disk electrode
ECSA	Electrochemical surface area
$H_{\text{upd}}$	Hydrogen underpotential deposition
CA	Chronoamperometry
EO	Electrochemical oxidation

LSV

Linear sweep voltammetry

ADT

Accelerated durability test

RDS

Rate determining step

## ABSTRACT

Acidic oxygen evolution reaction (OER) electrocatalysts that have high activity, extended durability, and lower costs are needed to further the development and wide-scale adoption of proton-exchange membrane water electrolyzers. In this work, hydrous cobalt-iridium oxide two-dimensional nanoframes were demonstrated to exhibit higher oxygen evolution activity and similar stability compared with commercial IrO<sub>2</sub>. Self-supported iridium–cobalt oxide was synthesized by heat treatment of iridium decorated Co(OH)<sub>2</sub> nanosheets followed by an acid leaching step. The synthesis process resulted in interconnected cobalt-iridium alloy domains within an unsupported, carbon-free porous nanostructure that allows three-dimensional molecular access to the catalytically active surface sites. After electrochemical conditioning within the OER potential range, the predominately bimetallic alloy surface was transformed to oxide/hydroxide surface. Oxygen evolution activities determined using a rotating disk electrode configuration showed that the hydrous cobalt-iridium oxide nanoframes provided ~17 times higher OER mass and specific activities compared with those of commercial IrO<sub>2</sub>. The higher OER activities are attributed the interaction of Ir with Co within the hydrous iridium-cobalt oxide surface and subsurface CoIr alloy that tunes the surface atomic and electronic structure. In addition to higher activity, the CoIr nanoframes exhibited similar stability as commercial IrO<sub>2</sub> using an accelerated durability testing protocol.

The effect of heat treatment on the structure and the electrocatalytic activity and stability toward the oxygen evolution reaction were studied. The Co(OH)<sub>2</sub>:Ir was treated

under H<sub>2</sub>/Ar atmosphere at 200°C, 300°C and 400°C, followed by an acid leaching step. The heat treatment temperature was shown to significantly influence the morphological, structural properties as well as the OER catalytic activity and stability of cobalt-iridium catalysts. The Scanning electron microscope/energy dispersive X-ray spectroscopy (SEM/EDS) images show that the iridium to oxygen atomic ratio in the catalyst treated at 400°C was 1:2 which is lower than 1:1 obtained for the catalysts treated at 200 and 300 °C. X-ray diffraction analysis of the CoIr catalysts confirmed a lattice compression compared to iridium. The lattice constant decreased, and the particle size increased as the treatment temperature increased. The catalyst treated at 200°C was found to have the highest electrochemical surface area. Catalytic activity and accelerated durability tests of the investigated catalysts indicate that the catalyst treated at 300°C had the best performance on activity and stability. Thus, 300°C was determined as the best heat treatment temperature regarding electrocatalytic activity and stability. This work supports that appropriately designed Co-Ir bimetallic oxyhydroxide structures can provide high activity and stability as acidic OER electrocatalysts, and the heat treatment temperature has a significant influence in the structure and electrocatalytic performance of the catalysts.

# I. INTRODUCTION

## 1.1. Hydrogen – A Renewable Energy

### 1.1.1. Hydrogen Resource Status and Challenge

The continuous increase in global energy demand and the decrease in the availability of fossil fuels have led to energy supply concerns.<sup>1</sup> Moreover, the energy sector now still depends mostly on fossil fuels, whose combustion gives rise to greenhouse gas emissions. Sustainability and environmental concerns are key drivers for the research in clean energy. Nowadays, conventional renewables energy (e.g., wind and solar power) play an important role in the green energy sector. However, the discontinuous availability of the renewable resource throughout the day during different seasons and in different areas is the main issue to be faced.<sup>2</sup> Hydrogen is a promising solution for energy storage of renewable energy systems at off-peak hours. However, great amounts of energy are required to split water molecules. Hydrogen is a carrier of energy; once hydrogen is separated from composed molecules it can be stored in large quantities for long periods of time. One of the benefits of hydrogen is its reversible quality that allows it to return its stored chemical energy back into electrical energy by means of a fuel cell stack. The designed energy cycle is shown in Figure 1. A water electrolysis cell consumes electricity to produce hydrogen, and a fuel cell can use that hydrogen and oxygen from air to generate electricity later.<sup>2</sup>

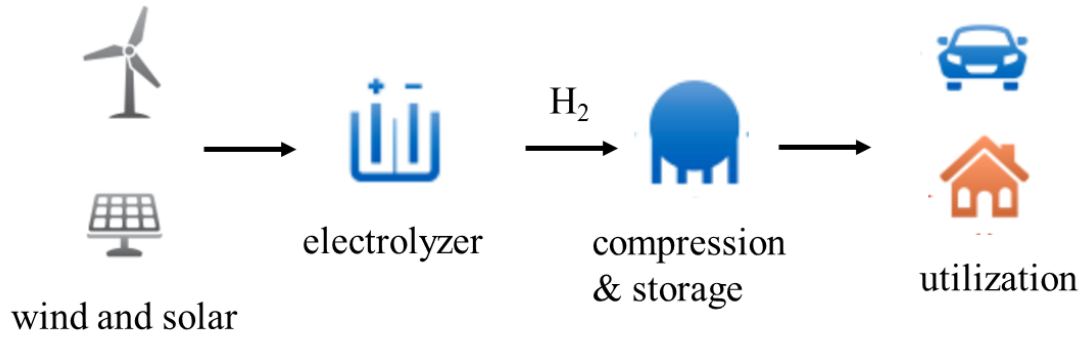
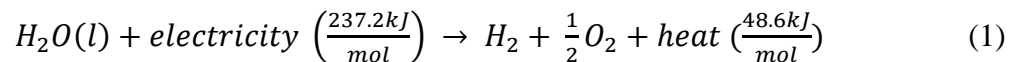


**Figure 1.** Wind/electrolysis System.

### 1.1.2. Proton Exchange Membrane Water Electrolyzer: Background and Research Needs

Water electrolysis is a promising technology for hydrogen production that started around two centuries ago.<sup>3</sup> Water electrolysis to provide hydrogen has various benefits including being pollution-free, utilizing simple reactions and relying on water resources which are abundantly available.<sup>4</sup> In the 1970s, the proton exchange membrane (PEM) electrolyzer was developed with limited use in small gas production capacities due to high cost materials and a short lifetime.<sup>3</sup> When a water molecule passes through electrochemical process, water molecules split to hydrogen and oxygen molecules. Input electricity is required for splitting the hydrogen and oxygen elements in water. The overall cell reaction is written as Equation 1:



When a voltage is applied to an electrolysis cell, hydrogen and oxygen gas bubbles are released at the cathode and anode respectively. At room temperature, due to the very poor ionic conductivity of pure water, an acid or base electrolyte is required to improve the conductivity of electrolyte. KOH, NaOH, H<sub>2</sub>SO<sub>4</sub> and HClO<sub>4</sub> aqueous solutions are the

most widely used electrolytes.<sup>5</sup> The aqueous solution splits into cations and anions, and these ions readily conduct electricity in an aqueous solution by flowing from one electrode to the other. Figure 2 shows the fundamental principle for a PEM water electrolysis. The anode and cathode are connected by a proton exchange membrane (e.g. Nafion). The electrodes normally use different electrocatalysts: IrO<sub>2</sub> for anode and Pt for cathode.

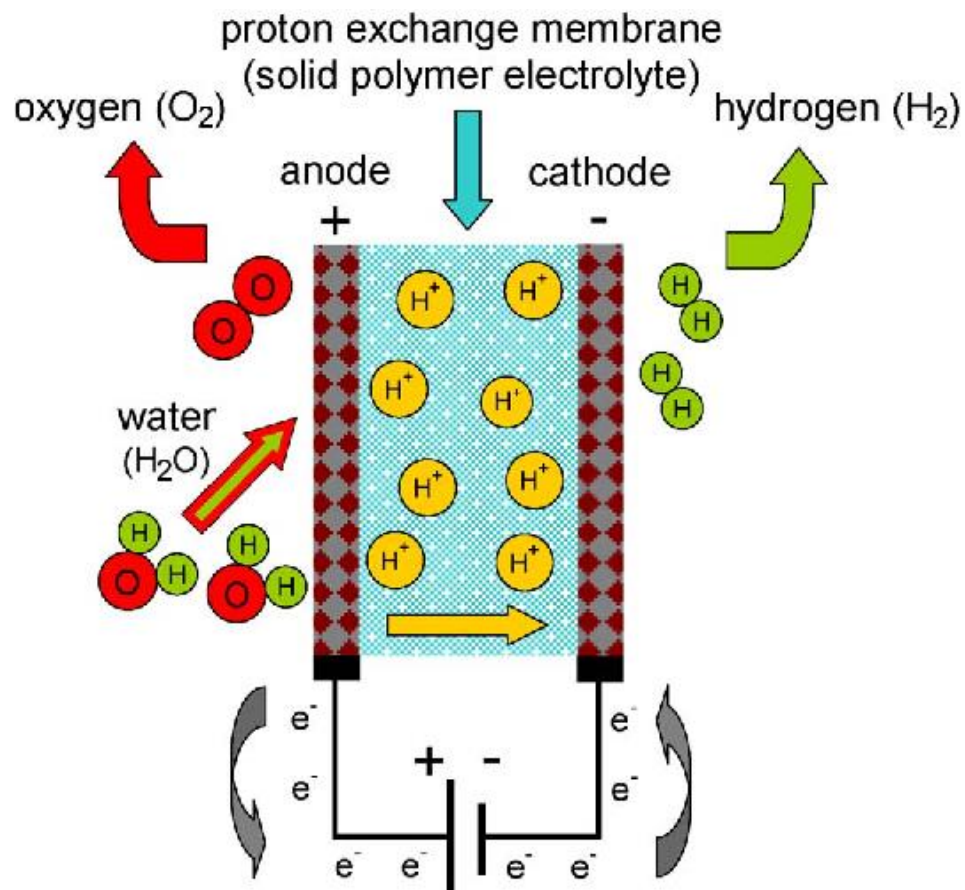


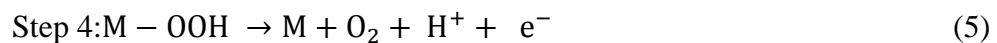
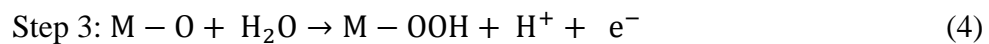
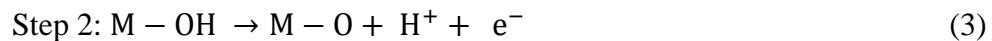
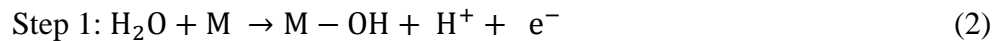
**Figure 2.** Schematic of the operating principle of a proton exchange membrane (PEM) electrolysis cell.<sup>6</sup> © [2012] IEEE.

### 1.2. Oxygen Evolution Reaction in Acid Electrolyte

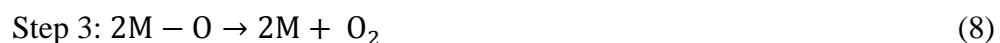
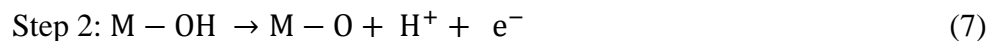
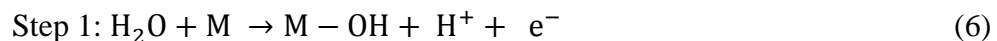
Proton exchange membrane water electrolysis (PEMWE) is a promising technology for sustainable hydrogen production due to its high-power density and

scalability.<sup>3,7,8</sup> However, PEMWE is greatly constrained by the kinetically sluggish oxygen evolution reaction (OER) because it is thermodynamically and kinetically unfavorable for removing four electrons to form oxygen–oxygen double bond.<sup>9</sup> A wider utilization of PEMWE requires increased efficiency, durability and further reduced cost.<sup>10</sup> Furthermore, the low pH, large potential (> 1.5 V) and high oxygen concentration operating environment at the anode also requires the use of electrocatalyst with significant stability.<sup>11</sup>

Different reaction mechanisms have been proposed for the OER on heterogeneous electrocatalysts, based on kinetic studies<sup>12</sup> or density functional theory (DFT) calculations.<sup>13,14</sup> However, none of the OER mechanisms has been fully validated based on experimental results. Rossmeisl et al.<sup>13,14</sup> proposed a peroxide path OER mechanism based on thermochemical analysis using DFT calculations as follows:



Bockris proposed a electrochemical oxide path<sup>15</sup> that involves the same initial two steps is described below:



Free energy diagrams for two hypothetical (‘real’ and ‘ideal’) catalysts are plotted at different potentials in Figure 3.<sup>16</sup> The horizontal lines represent the free adsorption

energies of the intermediates in each step. For a typical electrocatalyst, the reaction energies for each step will differ due to irregular variations in the adsorption energies of the intermediate species.<sup>17</sup> All steps in the reaction are thermodynamically unfavorable at potentials below the reversible potential, with  $\Delta G_i > 0$ . As the potential is increased, the free energies of the intermediates shift negatively so that the reaction steps eventually become thermodynamically favorable with  $\Delta G_i \leq 0$ .

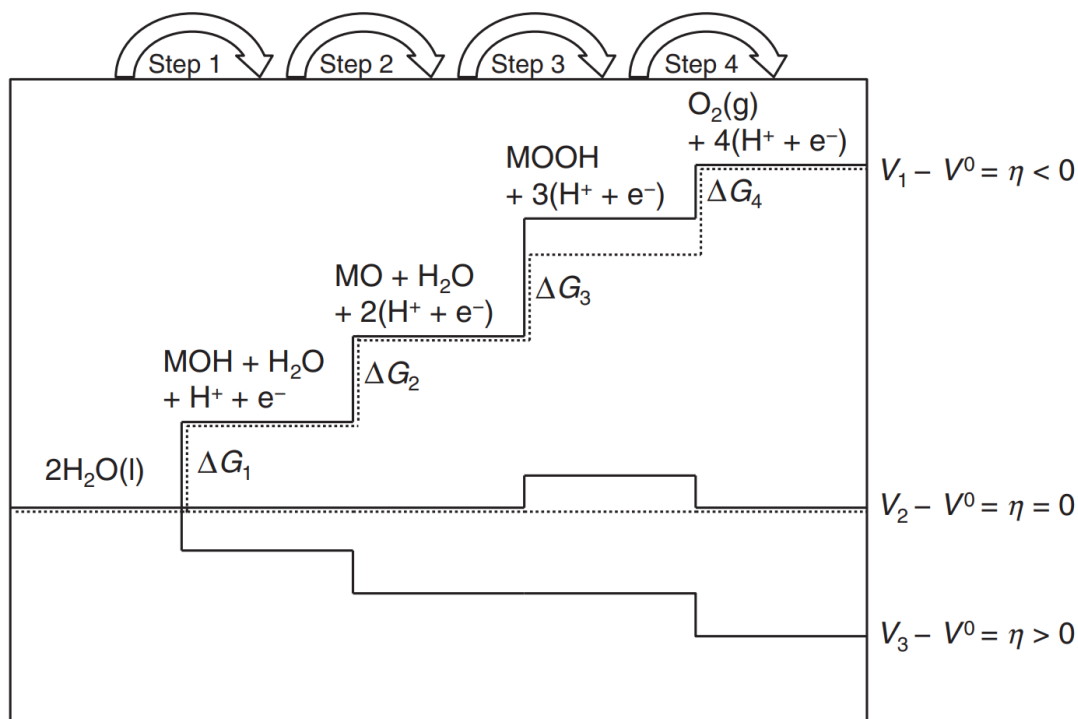


**Figure 3.** Schematic illustrate of the Gibbs free energy of the reactive species and intermediates in the four steps of oxygen evolution reaction.<sup>16</sup> © Springer International Publishing Switzerland 2016.

### 1.3. Electrocatalysts for Oxygen Evolution Reaction

#### 1.3.1. Ruthenium, Iridium, Ruthenium Oxide and Iridium Oxide Catalysts

Significant efforts have been devoted to developing catalysts for water electrolysis. Noble metal (Ru, Ir and Pt) have been investigated as OER catalysts.<sup>18-20</sup> As

shown in Figure 4, Cherevko et al. found the OER on metal shows a general activity trend as follows: Ru > Ir > Rh > Pt > Au.<sup>21</sup> The stability of the metals follows a different trend: Pt > Rh > Ir > Au ≥ Ru. The activity trend was established based on the overpotential at 5 mAcm<sub>geo</sub><sup>-2</sup><sup>22</sup> and shows a tendency that less active OER catalysts have a higher stability.

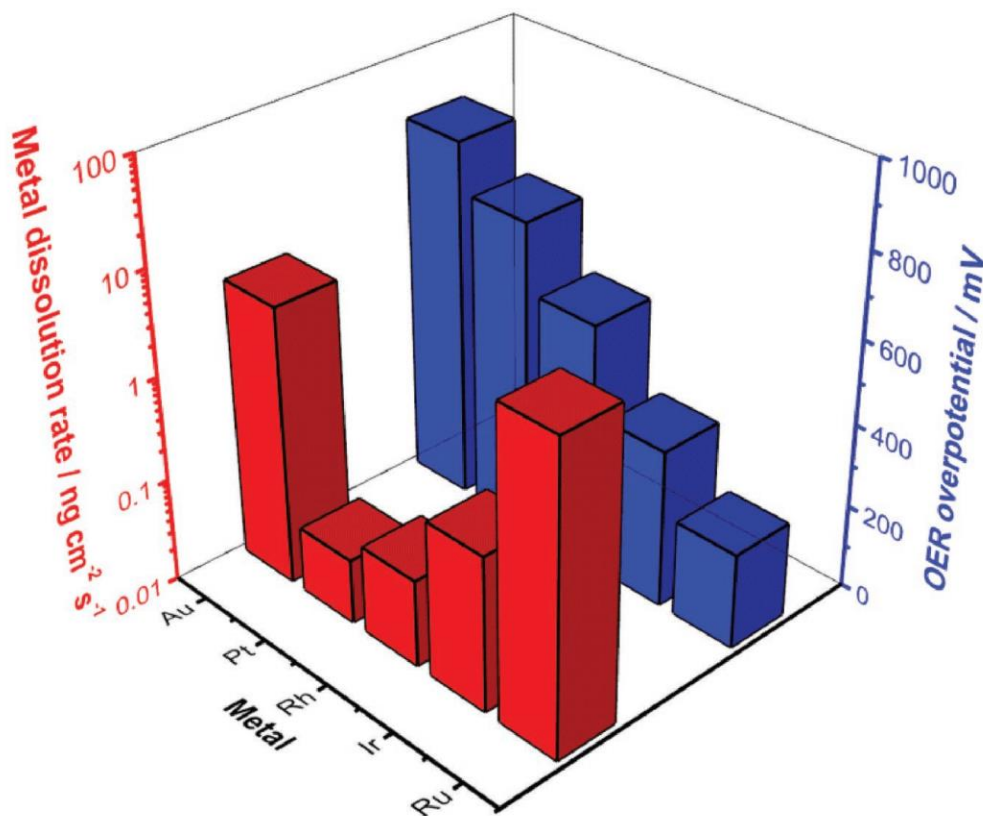


**Figure 4.** OER performance in form of overpotential and metal dissolution rates at 5 mA cm<sup>-2</sup> geometric current density of different metal electrodes.<sup>21</sup> © 2016 WILEY-VCH Verlag GmbH & Co. KGaA, Weinheim.

For oxides, iridium oxide (IrO<sub>2</sub>) and ruthenium oxide (RuO<sub>2</sub>) catalysts are considered the most active electrocatalysts for OER.<sup>23</sup> RuO<sub>2</sub> nanoparticles have slightly higher intrinsic and mass OER activities than IrO<sub>2</sub>.<sup>24</sup> Cherevko et. al conducted an OER performance comparison of well-defined Ru, RuO<sub>2</sub>, Ir and IrO<sub>2</sub> thin-film electrodes in

basic and acidic electrolyte.<sup>25</sup> It was found that the activity decreases as  $\text{Ru} > \text{Ir} \approx \text{RuO}_2 > \text{IrO}_2$ , while the dissolution of catalyst increases as  $\text{IrO}_2 \ll \text{RuO}_2 < \text{Ir} \ll \text{Ru}$ . The dissolution of these metals in both basic and acidic solutions is 2~3 orders of magnitude higher compared to their respective oxides.<sup>25</sup> Although Ru shows the outstanding OER performance, the very low stability prevents its practical utilization. Ir shows a high activity and a sufficient stability.<sup>20</sup> Ir based catalysts have many advantages, including good catalytic activities<sup>19</sup>, metallic conductivity<sup>26</sup> and especially stability towards high anodic potentials in an acidic environment.<sup>27</sup> Unfortunately, iridium is one of the rarest elements in the earth's crust with an average mass fraction of 0.001 ppm.<sup>28</sup> To make PEMWE feasible on a large scale, the Ir amount required must be reduced to a minimum. Also, the activity and stability of Ir needs to be further optimized.

### 1.3.2. Supported Iridium Catalysts

To improve the activity and stability of Ir-based catalysts, iridium can be dispersed on a support material. The support material is required to have a high electrical conductivity, a high surface area, and good corrosion stability under high potentials. Carbon is a widely used support material since it provides a high electrical conductivity and a high surface area.<sup>29</sup> However, carbon as a support material shows low stability under potentials which is required for operating a electrolyzer.<sup>30</sup> Since 0.207 V is the standard potential for the oxidation of carbon to  $\text{CO}_2$ , carbon based materials are thermodynamically unstable under the PEM electrolyzer anode potentials.<sup>30</sup>

Catalyst corrosion is a significant issue that limited wide utilization of electrolyzers, partially because the water electrolyzer is operated at high voltages.<sup>11</sup> This corrosion can create a loss of electrical contact necessary for the transportation of

electrons, thus decreasing the performance. Some supports have been used in electrocatalysis because they are inert and non-corrosive. Specifically, titanium dioxide has been investigated as a support for OER catalyst.  $\text{TiO}_2$  was investigated as stable support for different multimetallic nanoparticles i.e., Pt:Ru, Pt:Ir, Pt:Ru:Ir, Ir:Ru<sup>31</sup> and  $\text{IrO}_2$ <sup>32</sup>. The improved activity and stability of supported catalysts in comparison to pure catalysts is due to small, well-dispersed catalyst nanoparticles,<sup>31</sup> and the stabilization of small particles on  $\text{TiO}_2$  was related to particle-support interactions between  $\text{IrO}_2$  and  $\text{TiO}_2$  and/or high iridium oxidation states.<sup>32</sup>

However, the problem with titanium dioxide for electrochemical applications is the low conduction of electrons at low temperatures.<sup>33</sup> One way to improve the conductivity of  $\text{TiO}_2$  is increasing the ratio of electrocatalytically active material.<sup>34</sup> A  $\text{TiO}_2$  supported  $\text{IrO}_2$  OER catalyst with an  $\text{IrO}_2/\text{TiO}_2$  weight ratio of 0.6 and the specific surface of  $10 \text{ m}^2 \text{ g}^{-1}$  was observed to show good performance. This was obtained by covering  $\text{IrO}_2$  onto  $\text{TiO}_2$  in an amount sufficient to exceed their percolation level, thus providing the entire material with sufficient electron conductivity.<sup>35</sup> This approach requires the high amount of expensive, electrocatalytically active material to achieve good conductivity. Another method to ensure the electrical conductivity of  $\text{TiO}_2$  is doping of  $\text{TiO}_2$  for instance with Nb or Ta. Nb doped  $\text{TiO}_2$  can be synthesized with a comparably large BET surface and shows a good stability under OER operation.<sup>36</sup>

Metal oxide support interactions can improve the activity and stability of OER catalysts.<sup>37</sup> As shown in Figure 5, the potential need to drive the reaction on antimony-doped tin oxide (ATO)-supported  $\text{IrO}_x$  is slightly lower than carbon-supported  $\text{IrO}_x$ . Additionally, the potential increased dramatically after 9 hours on carbon-supported  $\text{IrO}_x$ ,

whereas ATO-supported  $\text{IrO}_x$  did not change a lot. The improved stability of ATO-supported  $\text{IrO}_x$  can be explained by metal/metal-oxide support interactions (MMOSI) which are not present in unsupported  $\text{IrO}_x$ . ATO-supported  $\text{IrO}_x$  presents a lower Ir oxidation state ( $\text{Ir}^{3.2+}$ ) after electrochemical oxidation compared to carbon supported  $\text{IrO}_x$  ( $\text{Ir}^{4+}$ ) due to the MMOSI effect which was reported to hinder the transformation of metallic Ir to  $\text{IrO}_x$  during operation.<sup>37</sup>

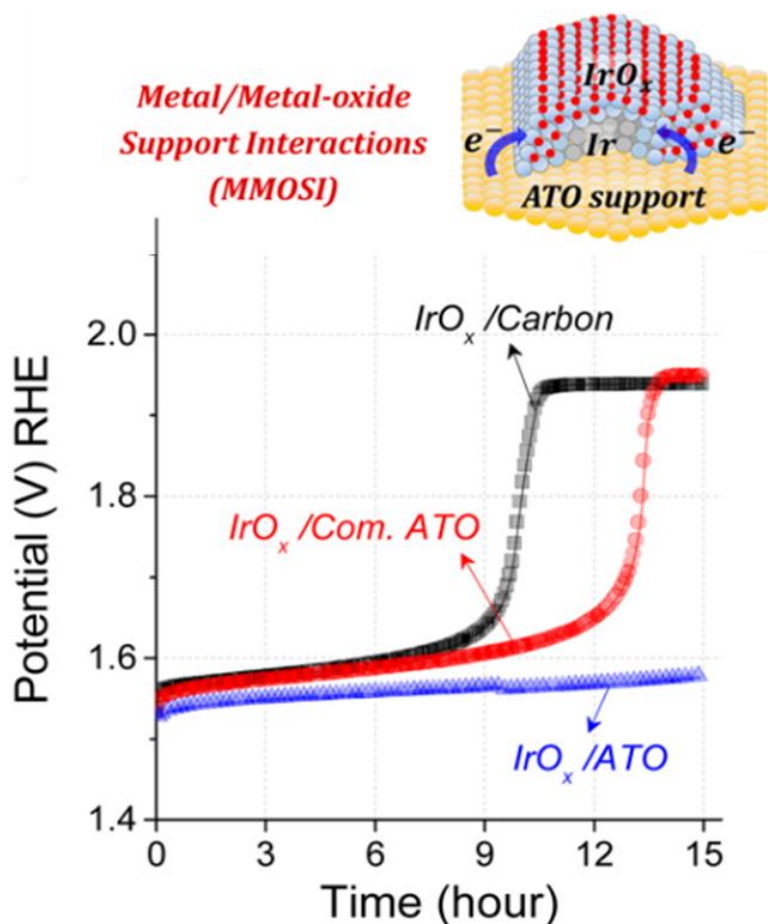


**Figure 5.** Constant current stability test of  $\text{IrO}_x/\text{ATO}$ ,  $\text{IrO}_x/\text{C}$  and  $\text{IrO}_x/\text{Commercial ATO}$  electrocatalysts for OER. Reprinted with permission from<sup>37</sup>. Copyright (2016) American Chemical Society.

### 1.3.3. Iridium-Non-noble Transition Metal Catalysts

In order to reduce the overpotential of Ir-based catalysts, Ir has been combined

with second or third metal. The interaction of non-noble metals within precious metal oxides such as IrO<sub>2</sub> has also been experimentally proven to significantly increase their OER activity.<sup>38</sup> Halck et al. have shown that the binding energies can be tuned by doping the iridium oxide surface with a second metal like Co or Ni.<sup>39</sup> Nong et al. synthesized IrO<sub>x</sub>@IrNi core shell nanoparticles which contained a lowered Ir amount in the OER catalyst.<sup>40</sup> The electrochemically leached out part of the Ni from the mixed oxides is expected to create Ni vacancies.<sup>38</sup> On the surface of catalyst, O species are partially replaced by OH species due to charge compensation, resulting in a hydroxide surface termination. The structure with OH species is less strongly bound compared to the prior structure since OH groups are coordinated by a smaller number of metal atoms, which was identified as a reason for the improved surface specific OER activity.<sup>38</sup> Also, to compensate the negative charge introduced by Ni vacancies, part of the O<sup>2-</sup> species are converted into O<sup>1-</sup> species. Based on prior work, the electrophilic O<sup>1-</sup> species provide an easier nucleophilic attack of water which is responsible for the improved OER activity.<sup>32</sup>

Many metals have been used to improve the catalytic OER performance of iridium and mixtures with non-precious metals of Cu<sup>41</sup>, Fe<sup>42</sup>, Os<sup>43</sup>, Ni<sup>38, 44, 45</sup> and Co<sup>46-48</sup> have been reported. In experimental work, Park et al. demonstrated that etched IrOsO<sub>x</sub> showed outstanding activity and stability for PEM electrolyzers.<sup>43</sup> IrOsO<sub>x</sub> black was synthesized using a solvent-free synthesis method, and an electrochemically activated Ir oxide with a high surface area was produced by the electrochemical etching of Os oxide for IrOsO<sub>x</sub>. They propose that the electrochemically activated Ir oxide black is highly active and stable and that this catalyst is not restricted by the traditional inverse relationship between OER activity and stability.

Substitution with nonprecious metals also has been demonstrated in theory as an approach to improve the activity of platinum-group metals toward the OER reaction.<sup>49</sup> Density functional theory (DFT) calculations showed that doping RuO<sub>2</sub> with Co or Ni within bridging sites resulted in lower overpotentials for OER, which was attributed to promoting proton transfer from M-OH or M-OOH reaction intermediates during the OER reaction.<sup>39</sup> In the case of IrO<sub>2</sub>, it has been shown that the insertion of a foreign element into its crystal structure can improve the catalytic activity through changing the resulting electronic structure.<sup>50</sup> Doping of Co within IrO<sub>2</sub> was shown from DFT calculations to tune the electron density and adjust the binding energies of intermediates which resulted in lower activation energies.<sup>51</sup> Figure 6 shows that the OER on pure Ir has a high reaction energy due to strong absorption of intermediates. After doping with Ni or Co, the catalyst has a weaker absorption, thus lower free energy. From a previous study, binding energies of oxygen intermediates follow the order of IrCoNi < IrCo < IrNi < Ir.<sup>52</sup>

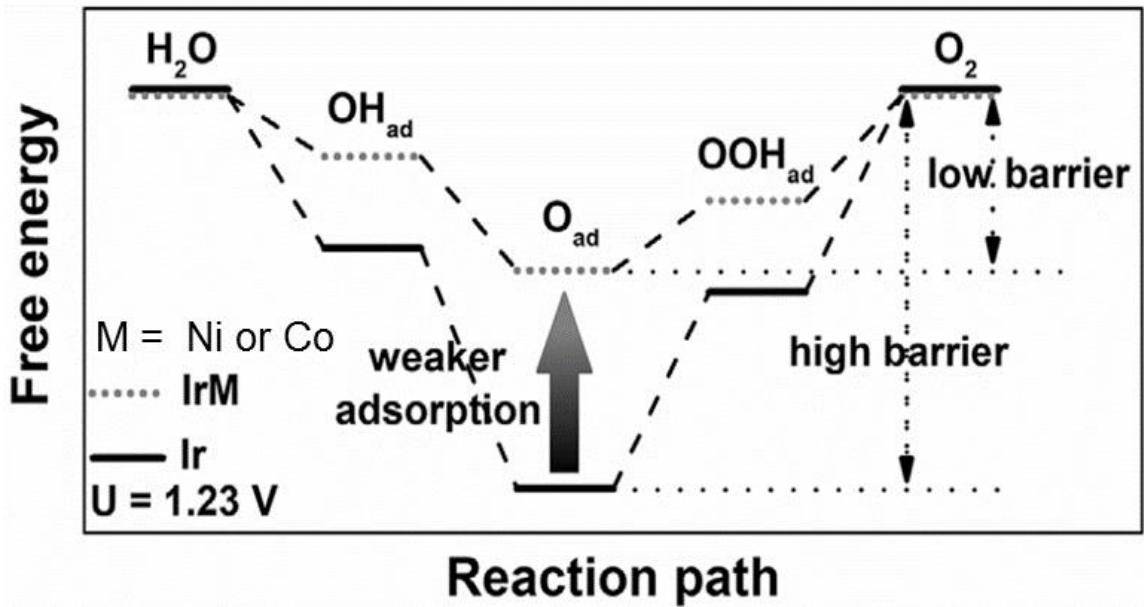


**Figure 6.** Schematic illustration of reaction paths for OER, indicating alloying iridium with nickel and/or cobalt leads to the barrier of reaction path decreasing.<sup>52</sup> © 2017 WILEY-VCH Verlag GmbH & Co. KGaA, Weinheim.

However, 3d metals may be dissolved in the highly corrosive conditions with the PEM water electrolysis, and a dissolution has been identified as the most serious problem impeding long-term operation.<sup>20</sup> Developing methods to enhance the OER activity while minimizing the loss of Ir based catalyst is needed. So far, many methods have been reported to leach out unstable elements, including electrochemical selective etching process, acid selective leaching and chemical selective leaching.<sup>53, 54</sup> Selective leaching can also create an Ir enriched porous structure on the surface at the same time.<sup>55</sup> Furthermore, according to the study by Strasser et al., the leaching of Ni atoms acts as promoter for the formation of structurally flexible, reactive OH groups, while reducing the less reactive oxide surface termination involving stable, unreactive divalent O surface oxygen species.<sup>38</sup> The surface OH groups act as reactive surface intermediates on active sites of the catalytic process. Thus, the ratio of weakly bonded surface hydroxyls was

found to be directly related to the surface specific catalytic OER activity of Ir oxides.<sup>38</sup>

#### 1.3.4. Two-Dimensional (2D) Iridium Alloys

Nanostructuring is another method to improve the performance of electrocatalysts, including the control of size and shape of the catalyst.<sup>56</sup> The nanoarchitecture of the catalyst can increase the utilization of the active metal. Small particles provide a large surface area, and thus can reduce the amount of the scarce Ir catalyst. However, OER needs a high potential and the nanostructured catalyst might be quickly dissolved.

Godinez et al. reported a carbon-free, self-supported hydrous iridium-nickel oxide with two-dimensional nanoframe structure.<sup>57</sup> As shown in Figure 7(A), the catalyst nanoarchitecture contains an interconnected network of metallic iridium-nickel alloy. Figure 7(B) is a high-angle annular dark-field scanning transmission electron microscopy (HAADF-STEM) image of the hydrous iridium-nickel oxide which shows the structure exhibited a IrO<sub>2</sub> shell and a metallic Ir–Ni core structure. The catalyst exhibits a unique catalytic nanoarchitecture that results in dramatically higher OER electrocatalytic activity compared with IrO<sub>2</sub> and other Ir-based OER electrocatalysts. However, the stability of the catalyst was lower than IrO<sub>2</sub>.

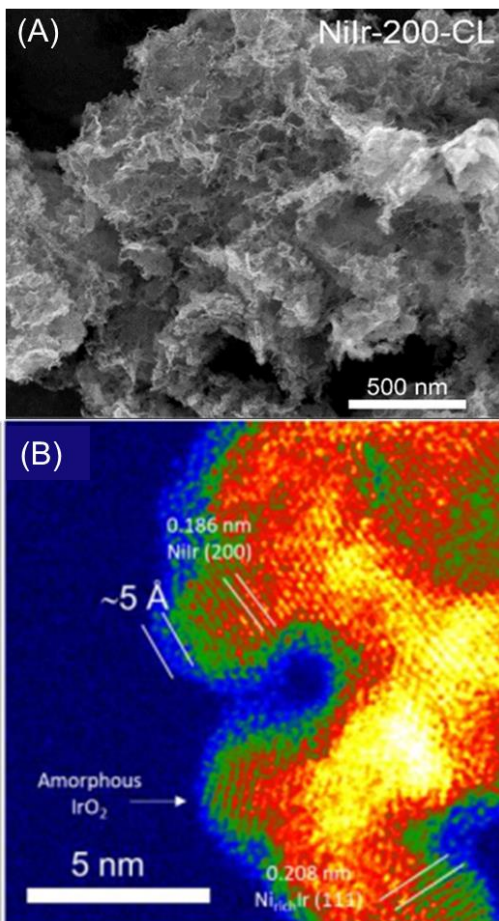


**Figure 7.** Scanning electron microscopy (SEM) image (A), and tomography high-angle annular dark-field scanning transmission electron microscopy (HAADF-STEM) image (B) of the hydrous iridium-nickel oxide.<sup>57</sup> Copyright © 2018, American Chemical Society.

### 1.3.5. Prior Work on Cobalt-Iridium Catalysts

Hu and Xu et al. prepared a porous Ir–Co and Ir–Ni binary oxide electrocatalyst<sup>58, 59</sup> with a Ir/Co molar ratio of about 0.7:0.3 through repeated Co-selective leaching of Co-rich composite oxide. The binary oxide catalyst exhibits the macro/mesoscale porous structure with a solid network. The catalyst exhibits much lower charge transfer resistance and higher stability for the OER than does the Ir–Co binary oxide of similar composition and the pure IrO<sub>2</sub>. These works demonstrate the ability of selective-leaching for shaping a porous and precious metal-surface-enriched oxide

catalyst.

Feng et al. introduced a general method for synthesizing a class of IrCo, IrNi, and IrCoNi multimetallic porous hollow nanocrystals<sup>52</sup> with hollow structure and porous features, through etching the IrM (M = Co, Ni) using Fe<sup>3+</sup>, as highly efficient bifunctional catalysts for overall water splitting catalysis. The DFT calculations reveal that alloying Ir with 3d transition metals can weaken the adsorption of oxygen-based intermediates by tuning the d-band center, resulting in the highly 3d transition metal-dependent OER activity. Particularly, the IrCoNi/CFP-based overall water splitting device can achieve a current density of 2 mAcm<sup>-2</sup> at a low potential of 1.56 V with only 8 mV polarization curve shift after 1000 cycles.

Alia et al. synthesized iridium–nickel and iridium–cobalt nanowires by a galvanic displacement method and studied their performance as oxygen evolution reaction electrocatalysts.<sup>60</sup> Figure 8 shows the XRD patterns of the iridium–cobalt nanowires with different amount of Ir. After acid leaching which removed the most of Co, the lattice constant is comparable with bulk Ir, indicating the Ir lattice compression was eliminated compared to the precursor. The XRD patterns also confirmed the presence of cobalt with different crystal structures and a Co<sub>3</sub>O<sub>4</sub> phase.

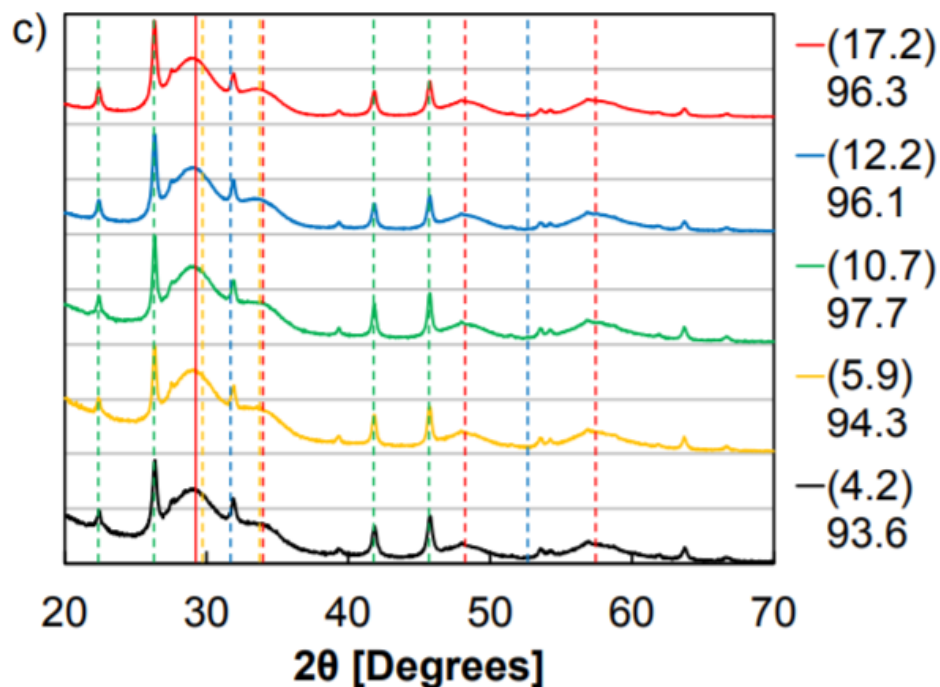


**Figure 8.** XRD patterns of the Ir-Co nanowires with different Ir composition (wt. % Ir). The weight percentage of Ir in each catalyst was listed in the figure legends and the weight percentage of Ir in as synthesized materials (before acid leaching) was listed in parentheses. Vertical lines correspond to Ir fcc (red), Co fcc (blue),  $\text{Co}_3\text{O}_4$  monoclinic (green), and Co hcp (yellow).<sup>60</sup> Copyright © 2018, American Chemical Society.

As shown in Figure 9, according to Alia's study, both Ni and Co were found to have positive impacts on catalytic performance of Ir.<sup>60</sup> The Ir-Ni nanowires have better performance compared to Ir-Co since it provides higher electrochemical surface area and better mass activity. The nanowire catalysts also showed improved durability after acid leaching.

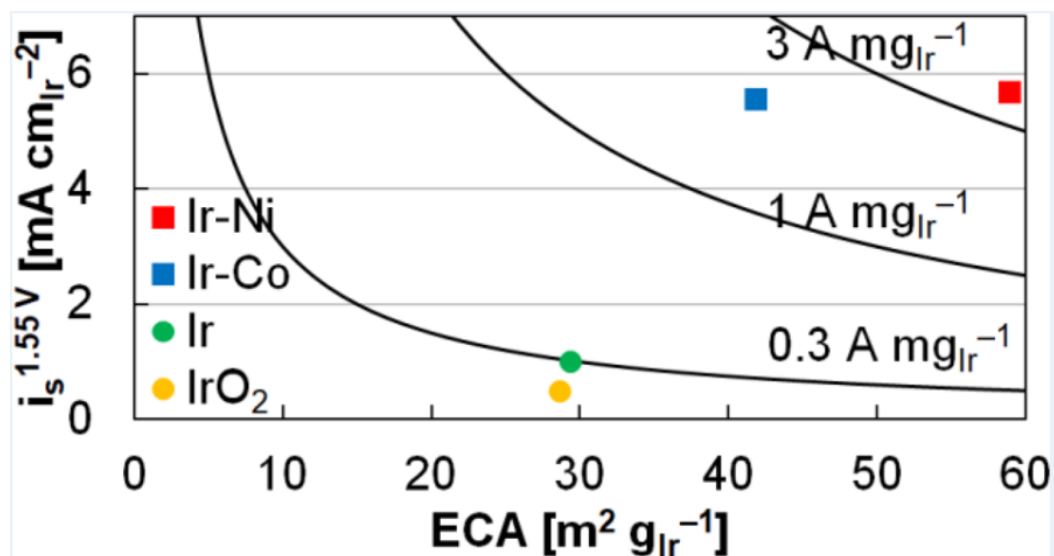


**Figure 9.** Comparison of specific activity, mass activity and electrochemical surface area of iridium-nickel, iridium-cobalt, metallic iridium and iridium oxide as oxygen evolution reaction electrocatalyst.<sup>60</sup> Copyright © 2018, American Chemical Society.

CoIr nanoframes have been physically combined with NiPt nanoframes and evaluated as bifunctional electrocatalysts for ORR and OER.<sup>61</sup> The interaction of Co and Ir has been shown to significantly increase the OER activity.<sup>61</sup>

#### 1.4. Effect of Temperature Treatment on Iridium-based Catalysts

A variety of synthesis methods have been studied to tailor the physical and chemical properties of Ir-based catalysts. The thermal treatment condition is one parameter which significantly influences the properties of the catalyst. The modification of composition, structure and morphology of the catalysts can be used to optimize the performance of electrocatalysts.<sup>62</sup> The overpotential and the stability toward OER of thin film Ir oxide catalysts were found to be strongly affected by the calcination temperature as can be seen in Figure 10.<sup>21</sup> The overpotential is small at low calcination temperatures and then increases at higher calcination temperatures. The film calcined at 350 °C has the lowest stability. The stability increases with increasing calcination temperature.

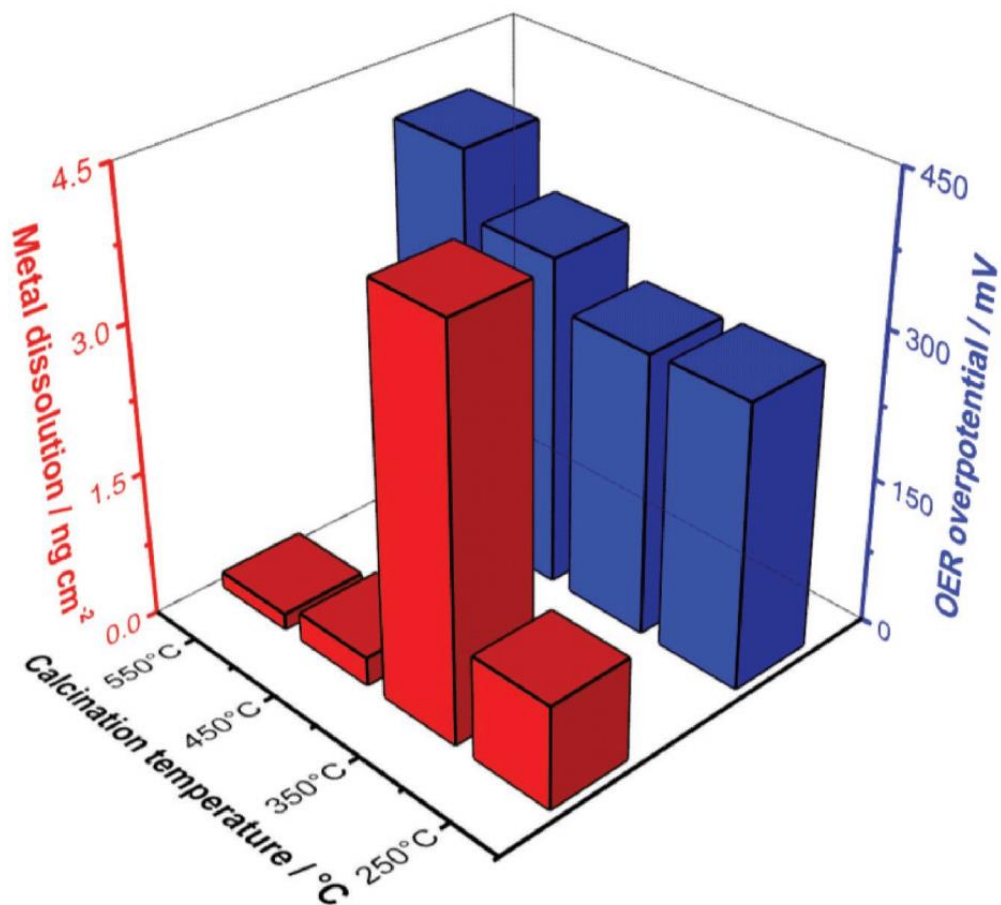


**Figure 10.** OER performance of thin-film Ir oxide model catalysts in form of overpotential and Ir dissolution as a function of the calcination temperature.<sup>21</sup> © 2016 WILEY-VCH Verlag GmbH & Co. KGaA, Weinheim.

Ahmadi et al. studied the effect of thermal treatment on morphological and chemical stability of shape-selected octahedral Pt<sub>0.5</sub>Ni<sub>0.5</sub> nanoparticles (NPs) supported on highly oriented pyrolytic graphite (HOPG).<sup>63</sup> They demonstrated that the mobility and long-range atomic segregation and composition of Pt<sub>0.5</sub>Ni<sub>0.5</sub> NPs were strongly affected by treatment environment. As shown in Figure 11, by annealing in hydrogen at ~300 °C, the reduction of Pt oxides occurs, and the consequential interdiffusion of Pt and Ni atoms leads to the formation of a uniform PtNi alloy. At high temperature, the alloy has a more extensive Ni and Pt reduction, combined with the formation of a Ni oxide core and a Pt

rich shell structure. The influence of temperature on surface segregation on nickel-based bimetallic alloy has also been theoretically predicted by using both the theoretical models and atomistic simulations based on a nano-thermodynamical model.<sup>64, 65</sup>

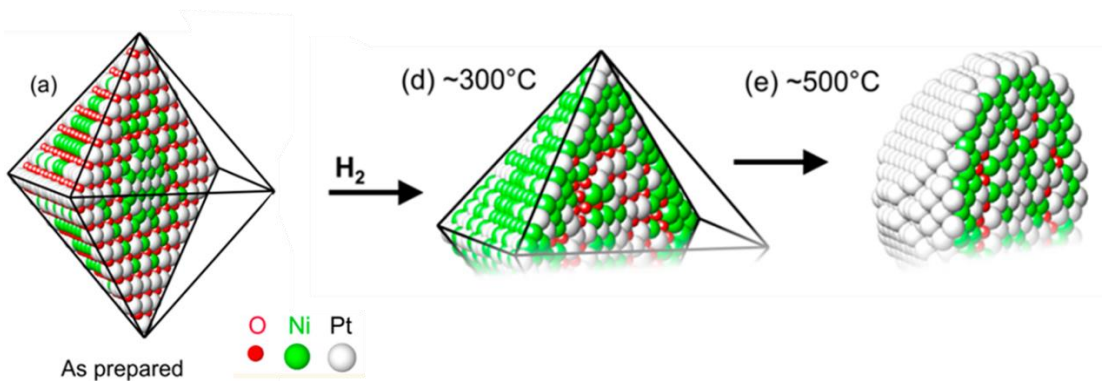


**Figure 11.** Schematic models describing the segregation of Pt and Ni atoms in octahedral  $\text{Pt}_{0.5}\text{Ni}_{0.5}$  NPs (a) as-prepared and after annealing from 25 to 500 °C in the following  $\text{H}_2$  (1 bar).<sup>63</sup> Copyright © 2013, American Chemical Society.

Reier et al. investigated the effect of calcination temperature on interacting between Ir oxide film and Ti substrate and its electrocatalytic oxygen evolution reaction (OER) activity.<sup>66</sup> The result shows that the amorphous catalyst treated at low temperature provided a higher intrinsic OER activity than the crystalline high temperature catalyst. The best Ir utilization was achieved at calcination temperatures of 250°C and 350°C. At 550°C, a Ti oxide interlayer was formed and Ti oxide migrated into the Ir oxide layer resulting in the lowest electrocatalytic OER activity.<sup>66</sup> The overpotential and the stability toward OER of thin film Ir oxide catalysts are strongly affected by the calcination temperature, and the overpotential and the stability increases with increasing calcination temperature.<sup>21</sup> Chandra et al., found that a simple annealing treatment between 300 and 350 °C can tune composition and crystallinity of the  $\text{IrO}_x$  nanostructure and the  $\text{IrO}_x(\text{OH})_y$  thin film with terminal hydroxo and bridging oxo motifs that are beneficial to

OER activity.<sup>67</sup>

Xu et al. reported that the crystallinity and the preferred orientation of IrO<sub>2</sub> crystallites can be changed by different temperature treatment of commercial IrO<sub>2</sub>-Ta<sub>2</sub>O<sub>5</sub> leading to different electrocatalytic activity for the oxygen evolution reaction (OER).<sup>68</sup> Figure 12 shows the XRD pattern of the Ti supported Ta<sub>2</sub>O<sub>5</sub> electrode calcined at different temperatures.<sup>68</sup> As the calcination temperature increased, the peaks belonging to IrO<sub>2</sub> become more narrow, indicating the degree of crystallinity increases with increasing calcination temperature. Furthermore, the catalysts calcined at low or moderate temperature showed preferred (101) planes of IrO<sub>2</sub>, whereas the catalyst calcined at high temperature showed preferred (110) orientation.

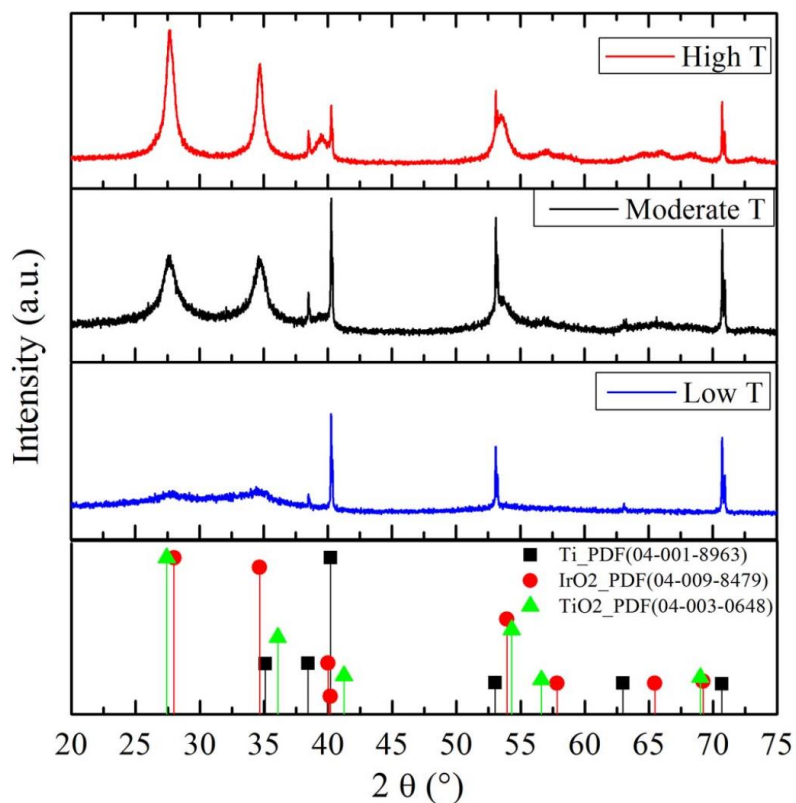


**Figure 12.** XRD patterns of the IrO<sub>2</sub>-Ta<sub>2</sub>O<sub>5</sub> electrodes calcined at three different temperatures compare with standard PDF of Ti, rutile IrO<sub>2</sub> and rutile TiO<sub>2</sub>.<sup>68</sup> © W. Xu et al. 2017. <https://creativecommons.org/licenses/by/4.0/>

As shown in Figure 13(A), the catalyst calcined at low temperature had the best catalytic activity toward OER, whereas the one calcined at high temperature was much lower. The higher activity of the catalyst treated at low temperature supports that the amorphous IrO<sub>2</sub> provides more active sites than the IrO<sub>2</sub> crystalline structure. Regarding the accelerated lifetime and Ir loss rate of the catalysts in Figure 13(B), a moderate temperature was suggested as the best calcination temperature due to its long accelerated lifetime and low Ir loss rate. Thus, the preferred orientation of IrO<sub>2</sub> can influence the catalytic stability.

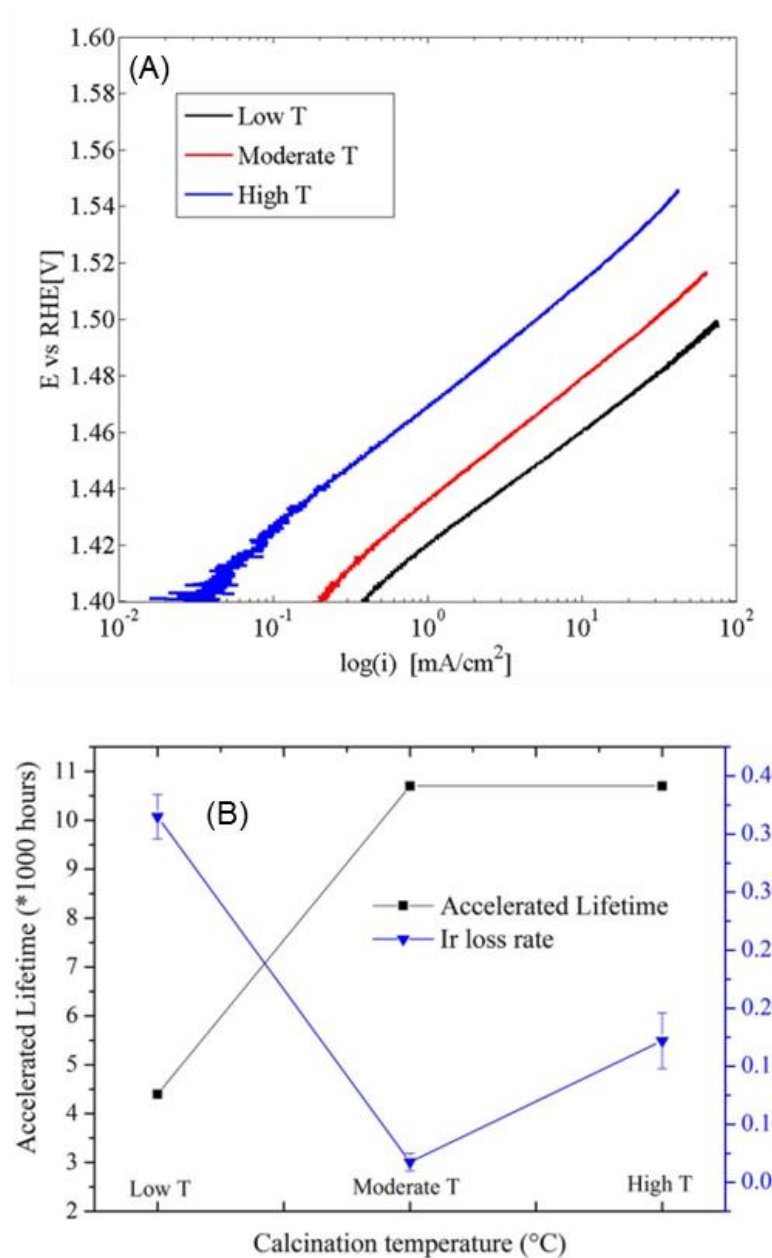


**Figure 13.** Polarization curves (A), and lifetime (black square) and Ir loss rate during accelerated lifetime tests (blue triangle) (B) of the IrO<sub>2</sub>-Ta<sub>2</sub>O<sub>5</sub> catalysts calcined at different temperatures.<sup>68</sup> © W. Xu et al. 2017. <https://creativecommons.org/licenses/by/4.0/>

Godinez et al. reported that thermal reduction temperature strongly influenced the electrocatalyst surface area, OER activity and stability of Ni-Ir 2D nanoframes; however, the Ni-Ir catalysts showed significantly lower stability relative to IrO<sub>2</sub>.<sup>57</sup>

## 1.5. Project Motivation and Objectives

Acidic oxygen evolution reaction (OER) electrocatalysts that have high activity, extended durability, and lower costs are needed to promote the development and wide utilization of proton-exchange membrane water electrolyzers. In this study, an unsupported (self-supported) cobalt-iridium electrocatalyst with a porous structure was investigated to provide high activity, avoid support degradation, and reduce active metal dissolution. The overall objective was to investigate bimetallic cobalt and iridium-based OER catalysts to obtain high activity and high stability. The interaction of iridium with the transition metal cobalt was used to tune the electron density of the catalyst active site and improve the activity of the catalyst. The highly porous two-dimensional nanoframe structure was investigated to promote the mass transport of reactants, intermediates, and products to the active sites of catalyst surface. Furthermore, the effect of temperature treatment on the physical and chemical properties and catalytic performance of electrocatalyst was evaluated. Especially, stability remains a critically important but significantly less studied relative to activity within acidic OER catalysts.<sup>69, 70</sup> The effect of temperature on the structure, activity and stability was investigated in this project. The purpose of the project was to build a correlation between morphological and structural properties of CoIr based catalyst and its activity and durability toward oxygen evolution reaction.

Objective 1 was the syntheses of Ir-decorated  $\text{Co}(\text{OH})_2$  nanosheets, and performing thermal treatment and acid leaching to obtain porous cobalt-iridium nanoframe catalysts. The specific objectives were to: i) decorate  $\text{Co}(\text{OH})_2$  nanosheet with iridium using a microwave assisted method; ii) use heat treatment and acid leaching to

tailor the morphology and structure of catalyst; and iii) evaluate the OER activity and stability of CoIr catalyst. The hypotheses of the objective were 1) thermal annealing could be used to redistribute elements, remove contaminants and change the catalytic performance of catalyst; and 2) acid leaching could be used to remove the non-noble metal and the contamination species and form a skeleton-type structure.

Prior work by our research group recently reported unsupported, hydrous iridium-nickel oxide two-dimensional (2D) nanoframes exhibit 14 times higher OER mass activity than commercial  $\text{IrO}_2$ .<sup>57</sup> However, the stability of the hydrous iridium-nickel oxide nanoframes was substantially lower than  $\text{IrO}_2$ . In this work, rather than using nickel, cobalt was studied as substituent within iridium and take the advantage of highly porous 2D nanoframes structure reported by our group. Prior work on cobalt incorporated Ir-based electrocatalysts reported improved OER activity and stability within both alkaline and acidic conditions.<sup>41, 71, 72</sup> The synthesis, structure, and OER activity and stability of hydrous iridium-cobalt oxide nanoframes was explored in this study.

Objective 2 was to determine the effect of temperature treatment on CoIr nanoframe catalysts. The specific objectives were to: i) perform heat treatment of  $\text{Co(OH)}_2\text{:Ir}$  in  $\text{H}_2/\text{Ar}$  atmosphere at 200°C, 300°C and 400°C; ii) evaluate the effect of heat treatment temperature on phase, crystallinity, composition, surface structure, and morphology of catalyst; and iii) evaluate the effect of heat treatment temperature on OER activity and stability. The hypotheses of this objective were 1) temperature treatment may change the segregation manner of Co and Ir and affect the following acid leaching step; 2) higher temperature may provide an enhanced interaction between Co and Ir but reduce porosity introduce phase segregation; and 3) lower temperature may

keep better nanostructure but create less interaction. The project considered that there may be an optimal temperature for obtaining high activity and maintaining the nanostructured morphology of the catalyst. In many reports, the effect of temperature on supported Ir based OER electrocatalyst<sup>21, 66-68, 73</sup> and bimetal unsupported ORR electrocatalyst<sup>63-65</sup> are well studied. However, there is limited published literature<sup>57</sup> investigating the effects of heat-treatment on Ir-based unsupported OER catalyst.

To determine the structure of the materials, scanning electron microscopy (SEM) and Energy Dispersive X-ray Spectroscopy (EDS) elemental mapping were used to analyze the morphology and elemental composition, and structure of the materials. Brunauer–Emmett–Teller (BET) surface area and pore size distribution was acquired by nitrogen adsorption/desorption isotherms. High-angular dark-field scanning transmission electron microscopy (HAADF-STEM) was used to observe the morphology and phase segregation manner of catalyst treated in different temperatures. X-ray diffraction (XRD) was utilized to determine the crystal structures and phases of the materials. The crystal structure, lattice constant and particle size of samples treated in different temperatures were determined and compared. For electrochemistry measurements, cyclic voltammetry (CV) and carbon monoxide (CO) stripping were used to study the surface structure of the catalyst. Both CV and CO experiments can provide important information on surface composition, particle size, and shape. Rotating Disk Electrode (RDE) measurements were used to precisely evaluate the kinetic activity of the catalyst. The Tafel slopes were calculated to provide some mechanistic insight into the reaction mechanism. Accelerated Durability Test (ADT) that applied a constant potential of 1.6 V for 13.5 hours was performed to investigate the stability of the catalyst. Inductively coupled plasma mass

spectrometry (ICP-MS) analysis was used to test the dissolution of iridium.

## 1.6. Principles of Experimental Methods Utilized

### 1.6.1. X-ray Diffraction Characterization

X-ray diffraction is utilized to determine the crystal structures, phases and the degree of structural order of materials. Generated copper  $K\alpha$  x-ray waves penetrate the surveyed material and are diffracted towards a detector. Constructive and destructive interference is explained by the Bragg equation<sup>74</sup>:

$$2d\sin(\theta) = n\lambda \quad (9)$$

where  $d$  is the interlayer distance,  $\theta$  is the angle of diffraction,  $n$  is an integer value, and  $\lambda$  is the wavelength of incoming radiation. The lattice constant ( $a_o$ ) of a unit cell can be calculated from the  $d$  value (in angstroms) and the indexed plane values ( $hkl$ ) with the equation for a cubic structure being<sup>75</sup>:

$$a_o = d \times \sqrt{h^2 + k^2 + l^2} \quad (10)$$

The crystallite sizes can be estimated from the Scherrer equation<sup>76</sup> based on the full width at half maximum (FWHM):

$$\tau = \frac{K\lambda}{\beta \cos \theta} \quad (11)$$

where  $\tau$  (nm) is the crystalline size;  $K$  is the shape factor which is commonly taken as 0.9;  $\lambda$  (nm) is the X-ray wavelength;  $\beta$  is the peak full width at half maximum (FWHM) intensity in radian; and  $\theta$  is the Bragg angle of the peak.

### 1.6.2. Rotating Disk Electrode Measurement

The rotating disc electrode (RDE) is a hydrodynamic electroanalytical technique used to limit the diffusion layer thickness.<sup>77</sup> An electrochemical reaction involving a solution species is affected by mass transport of reactants and products on the electrode.

A constant flow regime will provide a controlled mass transport for the electrochemical reactions at the electrodes, and thus eliminate mass transport limitation effects for the reactions. Rotating disk electrodes can be used for transport calculations.<sup>78</sup>

In a typical RDE experiment, the electrode surface is facing down. When the electrode starts to rotate, the electrolyte is pulled up to the center of the electrode and flushed outwards across the surface of the disk (Figure 14).<sup>79</sup> A maximum limiting current at the electrode is obtained when the concentration of species at the electrode surface is zero if the reaction rate is controlled by mass-transport. RDE is also an efficient method to remove products from the reaction. Efficient gas removal is important as adhering gas bubbles can hinder mass and heat transfer, overpotential, limiting current and ohmic resistance, and deactivate parts of the electrode surface.

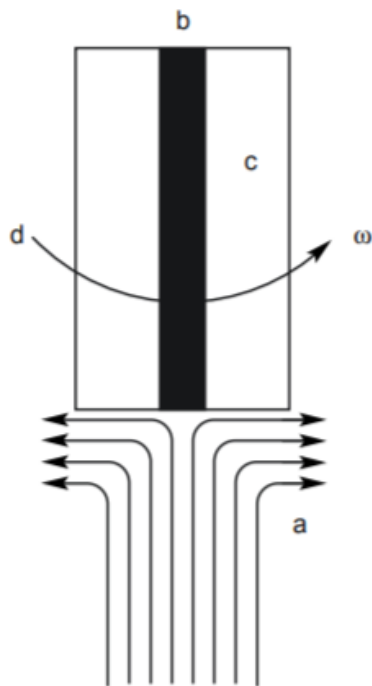


**Figure 14.** Solution movement caused by rotation of an RDE. a: flow of electrolyte solution; b: gold electrode; c: RDE body; d: direction of electrode rotation.<sup>79</sup> Copyright © 2000, American Chemical Society.

### 1.6.3. Cyclic Voltammetry

In cyclic voltammetry, the electrode potential is swept linearly between two potentials, and the current response is simultaneously recorded. Changing sweep rates can provide important information.<sup>80</sup> Cyclic voltammetry is usually a non-steady state technique, thus experiments are performed in unstirred solutions, where diffusion is the only significant contribution to mass transport. Thus, the concentration of reactants, intermediates and products are a function of both time and distance from the electrode.

Normally, if there are no redox-active couples in an aqueous solution, the observed current-potential behavior will correspond to the formation and dissolution of chemisorbed hydride and oxide layers on the electrode surface. If there are electrochemically active species in the solution, the current curve will be the sum of the curve for the electrode film processes that occur in solution without these species, and the current for the electrode reactions of the species in solution.<sup>81</sup>

### 1.6.4. Carbon Monoxide Stripping

Carbon monoxide (CO) stripping is a surface sensitive reaction which depends on surface conformation, composition, particle size and shape, thus, it has been used to characterize the catalyst surface. CO binds strongly to metallic surface atoms but can be electrochemically released in a known potential range.<sup>82</sup> The overall reaction<sup>83</sup> for removing adsorbed CO is:



The detection of a CO oxidation peak on iridium-based catalysts supports the presence of a metallic iridium phase. The electrochemical surface area of metallic iridium ( $\text{ECSA}_{\text{Ir}}$ ) determined from CO oxidation can be calculated using the following

equations:

$$Q_{CO} (C) = \frac{\int_a^b i dV}{dV/dt} \quad (13)$$

$$ECSA_{Ir}(m^2g_{Ir}^{-1}) = \left[ \frac{Q_{CO} (C)/2}{358 \mu C cm_{Ir}^{-2} L_{Ir}(mg_{Ir} cm^{-2})A_g(cm^2)} \right] 10^5 \quad (14)$$

The total charge,  $Q_{CO} (C)$ , is calculated from the integrated CO oxidation ( $\int_a^b i dV$ ) divided by the scan rate ( $dV/dt$ ) applied. In equation 14,  $i$  is the current in Amps. The Coulombic charge conversion factor is  $358 \mu C cm_{Ir}^{-2}$ .<sup>71</sup>

#### 1.6.5. Pseudocapacitance Measurements

The electrochemical surface area of iridium oxide ( $ECSA_{IrO_2}$ ) is an important factor, that will affect the iridium oxide catalyst performance including catalyst utilization and mass activity. However, iridium oxide does not have the same mechanism for underpotential deposition of hydrogen onto its surface or CO stripping as metallic iridium, which makes it difficult to determine the ECSA of iridium oxide. It has been reported that in cyclic voltammetry of iridium, the charge transferred during the iridium redox reaction is proportional to the number of iridium active sites which can be used as an estimation of the electrochemical surface area.<sup>66, 84, 85</sup> Electrochemical surface characterization was performed by cyclic voltammetry between 0.3 and 1.25  $V_{RHE}$  with a scan rate of  $50 mVs^{-1}$ . The electrochemical surface area was calculated by the pseudocapacitive charge and the coulombic conversion factor<sup>86</sup> of  $596 \mu C cm_{IrO_2}^{-2}$  using the equations:

$$Q_{oxidation scan} (C) = \frac{\int_{0.3}^{1.25} i dV}{dV/dt} \quad (15)$$

$$\text{ECSA}_{\text{IrO}_2}(\text{m}^2 \text{g}_{\text{Ir}}^{-1}) = \left[ \frac{Q_{\text{Oxidation Scan}} (C)}{596 \mu\text{C cm}_{\text{Ir}}^{-2} L_{\text{Ir}}(\text{mg}_{\text{Ir}} \text{cm}^{-2}) A_{\text{geo}}(\text{cm}^2)} \right] 10^5 \quad (16)$$

### 1.6.6. Tafel Plots

A Tafel slope is a commonly used factor for evaluating the activity of an electrocatalyst and can also give some mechanistic insight to the catalyzed reaction at the electrode.<sup>16</sup> The Tafel slope shows how much potential needs be applied to produce a resultant amount of current. The slope  $b$  of the Tafel plot is represented with the following equation:

$$b = \frac{\partial \eta}{\partial \log(i)} = \frac{2.303RT}{\alpha F} \quad (17)$$

where  $\alpha$  is the transfer coefficient for the anodic reaction,  $\eta$  is the ohmic-drop corrected overpotential,  $F$  is Faraday's constant,  $R$  is the gas constant, and  $T$  is the temperature.<sup>87</sup> It is noted in equation 17 the slope is dependent on  $\alpha$ , the transfer coefficient.<sup>87</sup> The transfer coefficient of a Rate Determining Step (RDS) in a multi-step mechanism can be expressed as:

$$\alpha = \frac{n_f}{v} + n_r \beta \quad (18)$$

where  $n_f$  is the number of electrons transferred prior to the RDS,  $v$  is the number of times the RDS occurs in one mechanistic cycle,  $n_r$  is the number of electrons transferred in a RDS, and  $\beta$  is a symmetry factor (usually approximated to 0.5<sup>88</sup>). The value  $n_r$  is one for any RDS that is not a chemical process; for a chemical process the value is zero. Applying these parameters:

$$\alpha(\text{RDS}_1) = \frac{0}{1} + 1(0.5) = 0.5 \quad (19)$$

$$\alpha(\text{RDS}_2) = \frac{1}{1} + 1(0.5) = 1.5 \quad (20)$$

$$\alpha(\text{RDS}_{chem}) = \frac{1}{1} + 0(0.5) = 1 \quad (21)$$

When the transfer coefficient is now substituted into equation 17, an approximated slope is found for each RDS. The Tafel slopes  $b$  calculated from the transfer coefficients  $\alpha(\text{RDS}_1)$ ,  $\alpha(\text{RDS}_2)$ , and  $\alpha(\text{RDS}_3)$  are 120, 40, and 60mV dec<sup>-1</sup> respectively.

## II. EXPERIMENTAL METHODS

### 2.1. Chemicals

Cobalt nitrate hexahydrate ( $\text{Co}(\text{NO}_3)_2 \cdot 6\text{H}_2\text{O}$ , 98 %), iridium chloride hydrate ( $\text{IrCl}_3 \cdot x\text{H}_2\text{O}$ , 99.8%) and urea ( $\text{N}_2\text{COH}_4$ , 99.3%) were purchased from Alfa Aesar. Ethylene glycol and isopropanol (HPLC grade) were purchased from VWR Analytical. Ultrapure water ( $\geq 18.2 \text{ M}\Omega\text{-cm}$ ) was obtained from an ELGA water purifier instrument (PURELAB Classic). All electrochemical measurements were carried out in 0.1 M  $\text{HClO}_4$  diluted from 70%  $\text{HClO}_4$  (Veritas Doubly Distilled) ( $0.000001\% \text{ Cl}^-$ ). Nafion perfluorinated resin (5 wt%, 15~20% water) was purchased from Sigma-Aldrich. All reagents were used without further purification.

### 2.2. Material Synthesis

$\alpha\text{-Co}(\text{OH})_2$  and  $\text{Co}(\text{OH})_2\text{:Ir}$  were prepared using a microwave-assisted hydrothermal synthesis method as reported by our group for preparing  $\alpha\text{-Ni}(\text{OH})_2$  and  $\text{Ni}(\text{OH})_2\text{:Ir}$ .<sup>89</sup> To prepare the  $\alpha\text{-Co}(\text{OH})_2$  nanosheets, 1.05 g of  $\text{Co}(\text{NO}_3)_2 \cdot 6\text{H}_2\text{O}$  (98 %, Alfa Aesar) was combined with 0.6486 g of urea (99.3 %, Alfa Aesar) in 21 mL of ethylene glycol (99%, VWR) and 3 mL of ultrapure water. The solution was then transferred into a microwave vial of 30 mL containing a magnetic stir bar. The reaction was conducted in a Discover SP Microwave reactor at standard reaction mode, 120 °C, 150 watts for 13 min with active stirring. The reaction was then allowed to cool down by venting the reaction chamber with air. The powder was separated by centrifugation (Sorvall ST16, Thermo) at 3000 RPM for 5 min, and rinsed five times with ultrapure water and two times with isopropanol (HPLC grade, VWR) prior to being dried at 60 °C. To synthesize Ir- decorated  $\text{Co}(\text{OH})_2$  nanosheets, 0.038 g (equivalent to 20 wt. % of Ir vs

Co(OH)<sub>2</sub> of IrCl<sub>3</sub>.xH<sub>2</sub>O (99.8%, Alfa Aesar) was completely dissolved in 25 mL of ultrapure water, then 0.1 g of  $\alpha$ -Co(OH)<sub>2</sub> was added. The mixture was then transferred into a 30 mL microwave vial containing a magnetic stir bar. The reaction was conducted using a same parameters as described above for synthesis of Co(OH)<sub>2</sub> nanosheets.

For the temperature treatment, 0.2g of Ir-decorated Co(OH)<sub>2</sub> nanosheets were thermally treated within a tube furnace at 200 °C, 300 °C or 400 °C, using a ramp rate of 10 °C/min from room temperature for 20 minutes under 100 mL/min flowing H<sub>2</sub>/Ar (5/95 vol. %). Then the reactor was lifted above the oven and allowed to cool under 10 mL/min flowing H<sub>2</sub>/Ar flow until room temperature was reached. Since the sample treated at 400 °C was very reactive, it was left in the furnace under 10 mL min<sup>-1</sup> flowing H<sub>2</sub>/Ar (5/95 vol. %) overnight to avoid reacting with oxygen in the air. The heat treated samples then underwent a chemical leaching step as previously reported by our group.<sup>57</sup> For chemical leaching, 0.2 g of the as-prepared materials were dispersed in 100 mL of 0.05 M HNO<sub>3</sub> which was diluted from 70% HNO<sub>3</sub> (99.999%, Aldrich). The solution was bubbled with Ar for 20 min then heated to 80 °C for 2 hours under magnetic stirring. After the reaction, the suspension was cooled to room temperature under bubbling Ar. The solid was separated by centrifugation at 6000 RPM for 10 min and rinsed five times with ultrapure water and two times with isopropanol prior to being dried at 60 °C. The samples were noted as Co(OH)<sub>2</sub> ( $\alpha$ -Co(OH)<sub>2</sub> nanosheets), Co(OH)<sub>2</sub>:Ir (decorated  $\alpha$ -Co(OH)<sub>2</sub> nanosheets with Ir nanoparticles), CoIr200, CoIr300, CoIr400 (Co(OH)<sub>2</sub>:Ir treated at 200, 300 and 400 °C under H<sub>2</sub>/Ar), and CoIr200-CL, CoIr300-CL, CoIr400-CL (after chemical leaching). Due to the COVID -19 crisis, access to the research lab was limited. Synthesis of a second batch of CoIr400-CL to obtain duplicated data and demonstration

the repeatability of experiments for this sample was not obtained due to limited access.

### 2.3. Physical and Structural Characterization

Scanning electron microscope (SEM) and Energy Dispersive X-ray Spectroscopy (EDS) elemental mapping were performed with a Helios NanoLab 400 DualBeam Field Emission Scanning Electron Microscope. The samples were prepared by dispersing the catalysts in isopropanol and then coating on an aluminum holder. Powder X-ray diffraction (XRD) patterns were recorded using a Bruker AXS D8 Advance powder X-ray diffractometer with a Cu K $\alpha$  ( $\lambda = 1.5406 \text{ \AA}$ ) radiation source, operating at 40 kV and 25 mA and a high resolution energy dispersive 1D Linxeye XE detector. The scan range of  $2\theta$  was  $20^\circ < 2\theta < 80^\circ$  with a  $0.01^\circ$  increment.

Brunauer–Emmett–Teller (BET) surface area and pore sizes was measured by nitrogen adsorption/desorption isotherms using a Micromeritics ASAP 2020 surface area and porosimetry analyzer. Samples were degassed at  $120^\circ\text{C}$  for 16 h prior to characterization. Transmission FTIR measurements were obtained using a Harrick Scientific (Pleasantville, NY) SplitPea ATR microsampling accessory coupled to a Bruker (Billerica, MA) Tensor II FT-IR spectrometer using potassium bromide (KBr) pellets prepared by combining the sample with dried KBr. Cs-corrected scanning transmission electron microscopy (STEM) was carried out by using a JEM-ARM200F (200 kV, JEOL) equipped with an energy-dispersed spectrometer (EDAX Silicon Drift detector). High-angle annular dark field STEM (HAADF-STEM) was obtained with a convergence angle of 26 mrad and collection semiangles from 50 to 180 mrad. The probe size used was about 0.09 nm with the probe current of 22 pA. Duplicated data of characterization of CoIr400-CL was not obtained due to limited access to the research

lab.

#### 2.4. Electrochemical Characterization

The electrochemical measurements were conducted at constant temperature (298 K) in a three-electrode cell equipped with a thin-film rotating disk electrode (TF-RDE) configuration including an Autolab PGSTAT128N bipotentiostat and rotation control (Pine Instruments). A gold disk electrode (RDE, Pine Research instrument, geometric area:  $0.196 \text{ cm}^2$ ) with a thin film of prepared catalyst was used as working electrode. A Pt electrode and a freshly prepared reversible hydrogen electrode (RHE) were used as counter and reference electrodes, respectively. All potentials were referred to the reversible hydrogen electrode. The 0.1 M  $\text{HClO}_4$  electrolyte was prepared by dilution of 70%  $\text{HClO}_4$  (Veritas Doubly Distilled, GFS Chemicals) ( $0.000001\% \text{ Cl}^-$ ) with ultrapure water ( $\geq 18 \text{ M}\Omega\text{-cm}$ ). The working electrode fabrication and RDE testing protocols were adapted from methods previously reported.<sup>71</sup> Catalyst inks were prepared by combining  $\sim 3 \text{ mg}$  of the catalysts with a corresponding volume of ultrapure water ( $\geq 18 \text{ M}\Omega\text{-cm}$ ) to yield a catalyst ink with concentration of  $\sim 0.37 \text{ mg}_{\text{cat}}/\text{mL}$ . The inks were sonicated (Fisher, 40 kHz) in an ice-bath for 30 minutes. The ink was then immersed in a controlled temperature bath ( $25 \text{ }^\circ\text{C}$ ) for 1 minute while maintaining agitation and then used immediately. 10  $\mu\text{L}$  inks were applied to a polished Au working electrode and allowed to dry under rotation (600 RPM) under ambient conditions. The loading of catalyst was  $17.1 \mu\text{g}_{\text{Ir}}\text{cm}_{\text{geo}}^{-2}$  for CoIr200-CL,  $18.8 \mu\text{g}_{\text{Ir}}\text{cm}_{\text{geo}}^{-2}$  for CoIr300-CL, and  $17.8 \mu\text{g}_{\text{Ir}}\text{cm}_{\text{geo}}^{-2}$  for CoIr400-CL, respectively. After the ink was dried, 10  $\mu\text{L}$  binder solution was applied over thin film of prepared catalyst and allowed to dry under ambient conditions. The stock binder solution was prepared by mixing 0.4 mL of Nafion suspension (Aldrich, 5 wt %,

1100 g equivalent weight), 20 mL of isopropanol, and 79.6 mL ultrapure water.

For the electrochemical tests, the electrodes were immersed in argon-saturated 0.1 M HClO<sub>4</sub> under potential control (0.1 V<sub>RHE</sub>). A conditioning process was performed before any measurements been taken by cycling 20 times from 0.05-1.0 V<sub>RHE</sub> at 100 mV s<sup>-1</sup> and 2500 rpm. The electrochemical surface area (ECSA) of metallic Ir was characterized by CO-stripping using a specific charge of 358 μC cm<sup>-2</sup> as the charge corresponding to a monolayer of adsorbed CO.<sup>71</sup> The working electrode was electrochemically oxidized by cycling between 0.05 to 1.5 V<sub>RHE</sub> for 60 cycles at a scan rate of 100 mV s<sup>-1</sup> in argon-saturated 0.1 M HClO<sub>4</sub> prior to the OER activity analysis. The electrochemical surface area of IrO<sub>2</sub> (ECSA<sub>IrO2</sub>) was determined by measuring the pseudocapacitive charge between 0.3 V and 1.25 V with a scan rate of 50 mV s<sup>-1</sup>, and the contribution of the Au disk current collector was subtracted. The electrochemical surface area was calculated using the background subtracted pseudocapacitive charge and the coulombic conversion factor of 596 μC cm<sub>IrO2</sub><sup>-2</sup>.<sup>86</sup>

To determine the oxygen evolution reaction activity, the electrode was conditioned by 10 cycles between the potential range 1.2-1.8 V<sub>RHE</sub> at 100 mV s<sup>-1</sup> and 2500 rpm. Linear sweep voltammetry (LSV) in the potential range of 1.2-1.8 V<sub>RHE</sub> was performed using a scan rate of 20 mV s<sup>-1</sup> and a rotation rate of 2500 rpm. Steady-state (iR-corrected) chronoamperometric measurements were then performed by gradually stepping the potential at steps of 0.01 V from 1.3 to 1.6 V<sub>RHE</sub> while holding for 5 seconds at each potential and rotating the working electrode at 2500 rpm. The internal resistance (iR) values (23-27 Ω) was determined previous to every evaluation using current interruption method at 1.6 V<sub>RHE</sub>. The data obtained from chronoamperometric

measurements were used for the Tafel plots and for determining the OER mass activity and specific activity. The mass-normalized OER activity was determined by the current at a specific voltage from the chronoamperometric measurements divided by the Ir mass on the electrode. Inspection of the Tafel plots for linear behavior within specific voltage ranges was used to evaluate that the electrode was not within a mass-transport limited regime within the specific voltage range. Tafel slopes were determined using current obtained from chronoamperometry measurements using the  $iR$ -corrected potential between 1.47 V to 1.52  $V_{RHE}$ . After the evaluation of the electrocatalyst in the OER potential range, CV measurements were again obtained to determine the nature of the surface condition after exposure to OER potentials of up to 1.8  $V_{RHE}$ .

Following the measurements of the OER activity, an accelerated durability test (ADT) was carried out by maintaining the electrode at a constant potential of 1.6  $V_{RHE}$  for 13.5 hours under a rotation rate of 2500 rpm. After the constant potential step was completed, the electrolyte was replaced and purge with argon for 30 minutes to remove bubbles.<sup>90</sup> After the ADT test, cyclic voltammetry (CV), LSV, and chronoamperometry measurements were obtained as described above. During LSV and chronoamperometry tests, to account for solution resistance the internal resistance was corrected by the potentiostat using a resistance of 25  $\Omega$ . After the stability tests, pseudocapacitive charge was also measured. The Ir dissolution in the electrolyte solution during the electrochemical oxidation and the accelerated durability test operation was determined by analysis of Ir in the electrolyte using Inductive Coupled Plasma Mass Spectroscopy (ICP-MS, PerkinElmer NexIon 2000). Duplicated data of electrochemical characterization of CoIr400-CL was not obtained due to limited access to the research lab.

### III. RESULTS AND DISCUSSION

#### 3.1. Overview of Synthesis Approach

The CoIr catalyst was synthesized through a four step process as summarized in Figure 15, following a synthesis protocol previously reported by our group.<sup>91</sup> The first step was formation of the template  $\alpha$ -Co(OH)<sub>2</sub> nanosheets using an accelerated microwave assisted process. The nanosheets provided a large surface for dispersion of Ir nanoparticles. The second step was deposition of metallic Ir nanoparticles on  $\alpha$ -Co(OH)<sub>2</sub> nanosheets. The third step was thermal treatment under controlled atmosphere (H<sub>2</sub>/Ar, 5/95 vol %) and different temperature 200 °C, 300 °C and 400 °C. During this thermal treatment step, a complex process consisting of several reactions and structural reorganization occurred during this step and involved the reduction of  $\alpha$ -Co(OH)<sub>2</sub>, water release, pore formation and Co-Ir alloying formation.. The last step consisted of chemical leaching in nitric acid (0.05 M HNO<sub>3</sub>) to remove the unstable metallic Co and to modify the porous structure.

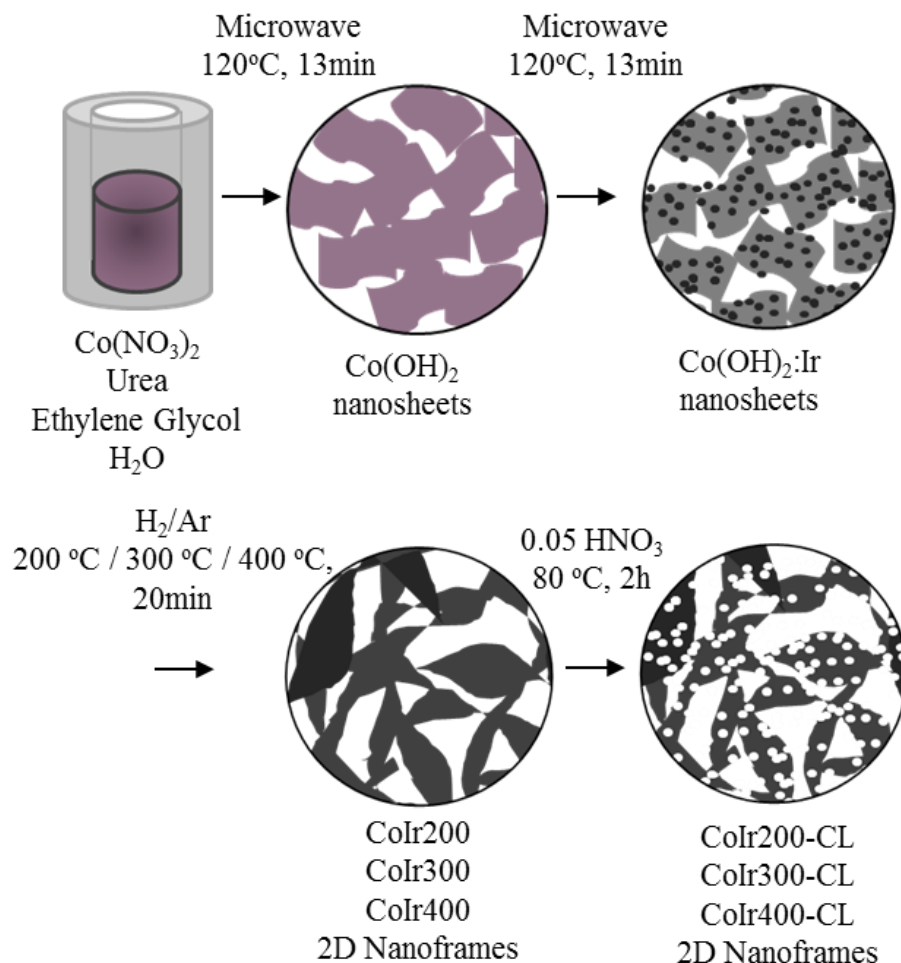


**Figure 15.** Schematic layout of the experimental steps for the synthesis of two-dimensional (2D) cobalt – iridium nanoframe catalysts.

### 3.2. Characterization of cobalt-iridium electrocatalyst and precursor materials

#### 3.2.1. Analysis of the morphology, surface area and elemental composition of cobalt-iridium catalyst and precursor materials.

The SEM image of the as-prepared Co(OH)<sub>2</sub> precursor (Figure 16A) consisted of extended ultra-thin nanosheets with lateral size in the range of 2-5 μm and estimated thickness of around 10 nm. The BET surface area of Co(OH)<sub>2</sub> was measured to be 70.3 ± 11 m<sup>2</sup>/g with a pore size of 18.0 ± 1.3 nm (Table 1). Similar results were obtained with α-

Ni(OH)<sub>2</sub> nanosheets synthesized using the same protocol.<sup>91</sup> After the Ir deposition step, the morphology of Co(OH)<sub>2</sub> nanosheets (Figure 16B) remained very similar. Furthermore, higher magnifications revealed a high density of well distributed Ir nanoparticles. The BET surface area of Co(OH)<sub>2</sub>: Ir showed a decrease to  $43.3 \pm 4.6$  m<sup>2</sup>/g with a pore size of  $13.4 \pm 1.1$  nm (see Table 1). The thermal treatment in hydrogen (i.e. H<sub>2</sub>/Ar, 300 °C) resulted in significant morphological and structural changes. As mentioned above, a complex process that involved water release, incorporation of Co into the Ir phase and pore formation, was carried out during the process. The process resulted in the formation of 2D Co-Ir nanoframe structure, consisted of short nanofilaments randomly connected to form a bidimensional network (Figure 16C). The hydrogen reduction treatment resulted in a decrease of BET surface area to  $32.3 \pm 0.7$  m<sup>2</sup>/g. The final process consisted in the leaching of unstable Co phase within the structure (Figure 16D). This step did not modify the 2D-nanoframe morphology but promoted the formation of micropores as detected by STEM, discussed below and increased the BET surface area to  $66.8 \pm 4.7$  m<sup>2</sup>/g (Table 1).

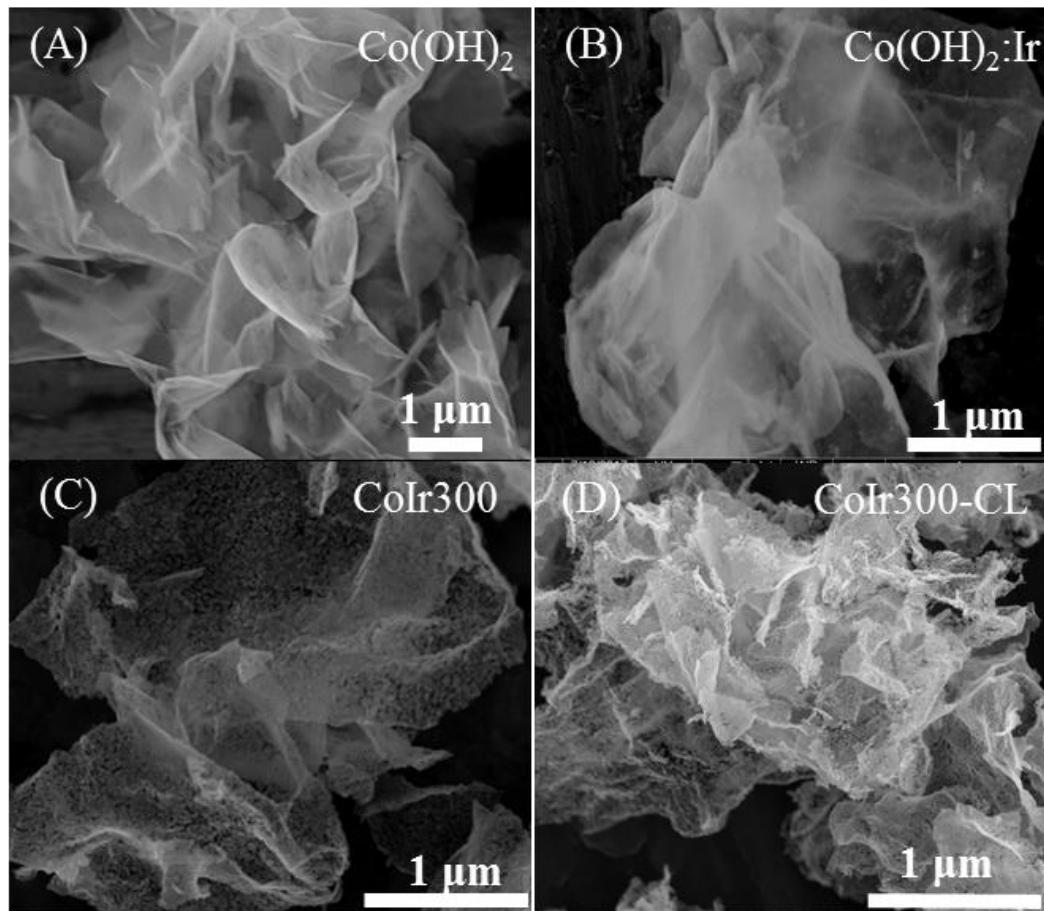


**Figure 16.** Representative secondary electron images obtained by scanning electron microscopy (SEM) of  $\text{Co(OH)}_2$  nanosheet precursor (A), as-prepared  $\text{Co(OH)}_2\text{:Ir}$  (B), after thermal treatment under  $\text{H}_2/\text{Ar}$  at  $300\text{ }^\circ\text{C}$  (CoIr300) (C), and CoIr300-CL after chemical leaching(D).

The adsorption and desorption isotherms and the pore volume and pore size distribution plots of CoIr300-CL are shown in Figure 17. The pore size distribution plot supports that the CoIr300-CL nanoframes contain both mesopores (pores with diameters between 2 and 50 nm) and macropores (pores with diameters  $>50$  nm), which are desirable for mass transport.<sup>92,93</sup>

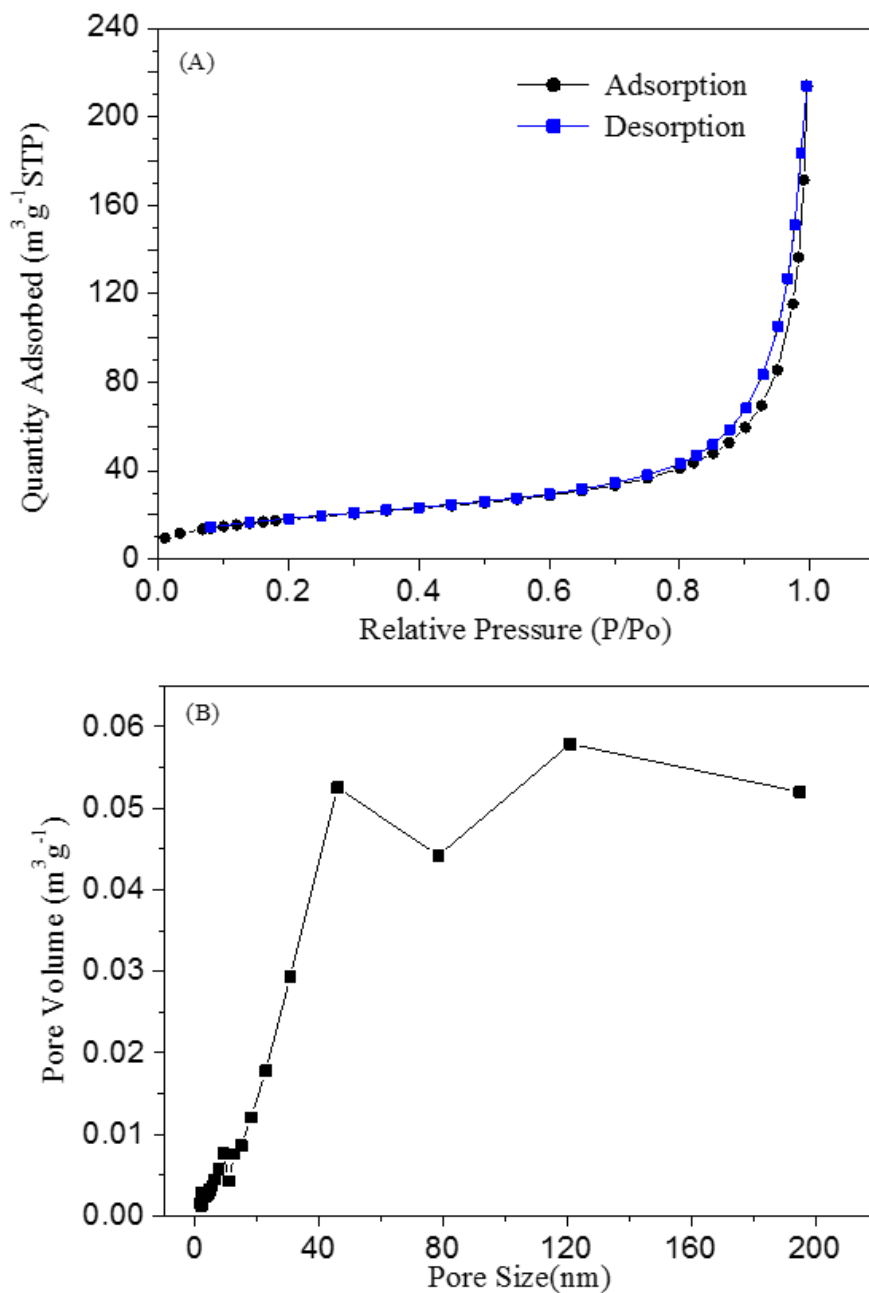


**Figure 17.** Isotherm (A) and pore-size distribution (PSD) plot (B) of CoIr300-CL obtained from nitrogen physisorption.

**Table 1.** Average Brunauer-Emmett-Teller (BET) surface areas, cumulative pore volumes, and mean pore diameters of precursors and catalyst materials.

<b>Material ID</b>	<b>BET surface area (m<sup>2</sup> g<sup>-1</sup>)</b>	<b>Cumulative pore volume (cm<sup>3</sup> g<sup>-1</sup>)</b>	<b>Mean pore diameter (nm)</b>
Co(OH) <sub>2</sub> -as prep	70 ± 11	0.31 ± 0.05	18 ± 1
Co(OH) <sub>2</sub> :Ir	43 ± 5	0.15 ± 0.03	13 ± 1
CoIr300	32 ± 1	0.15 ± 0.03	18 ± 3
CoIr300-CL	67 ± 5	0.33 ± 0.01	18 ± 1

The distribution and changes of elemental composition throughout the synthesis pathway were followed by EDS (Figure 18). In general, the as-prepared, intermediates and final catalyst showed very homogeneous distribution of Co and Ir at this scale. The Co(OH)<sub>2</sub>:Ir sample contained 23.1 ± 3.5 wt. % of Ir, very close to the estimated nominal weight ratio (i.e. 20 wt. %), highlighting good reaction efficiency. After thermal treatment at 300 °C, the iridium content increased to 36.0 ± 1.8 wt. %, while the oxygen decreased to 17.3 ± 4.3 wt. % which is attributed to remove of water from the structure due to hydrogen treatment.

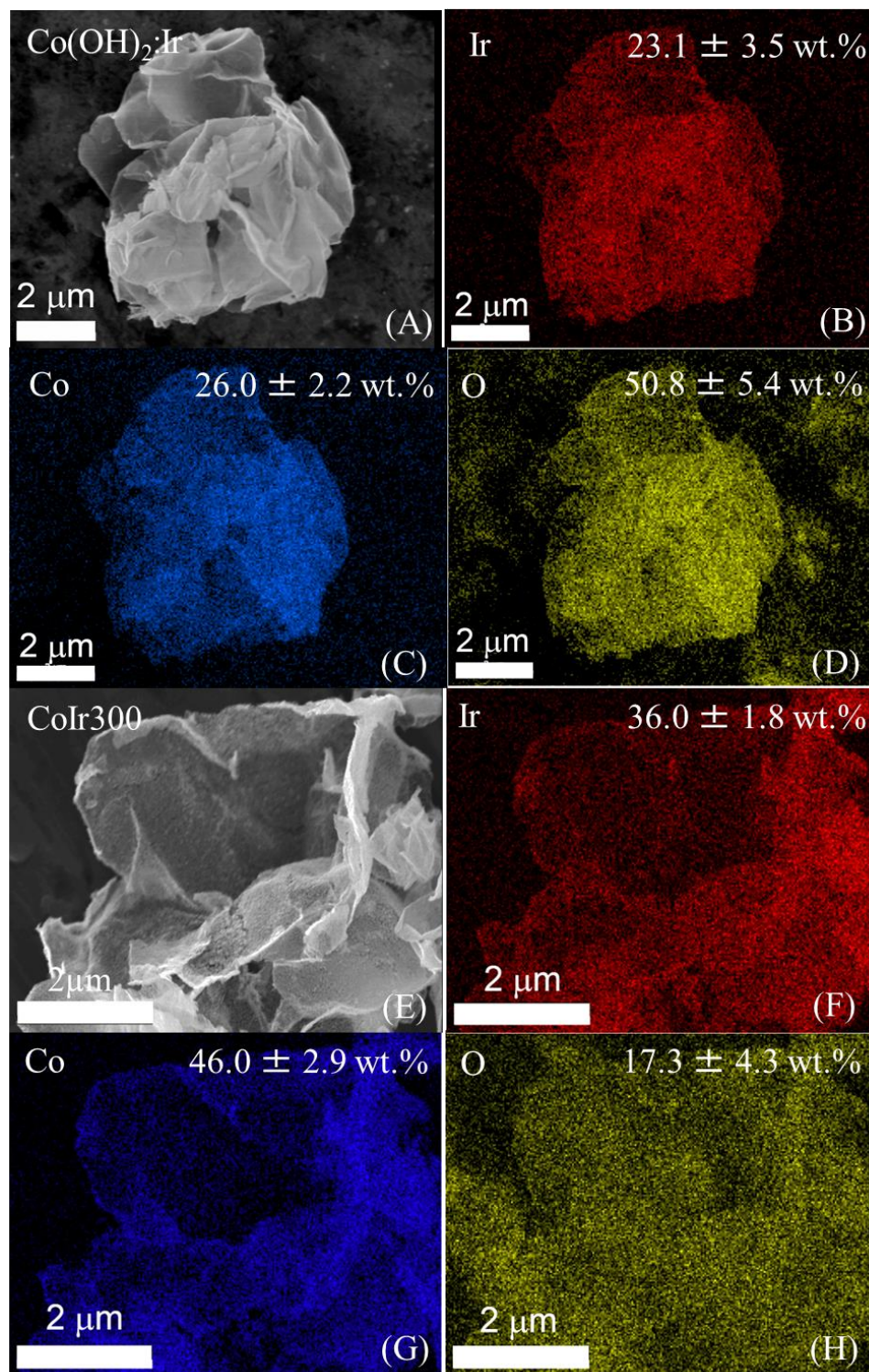


**Figure 18.** Scanning electron microscopy (SEM) images and energy-dispersive x-ray spectroscopy (EDS) mapping analysis of  $\text{Co(OH)}_2\text{:Ir}$  (A-D) and  $\text{CoIr}$  (E-H) showing iridium, cobalt, and oxygen within the structures.

As shown in Figure 19, after the acid leaching, the selective removal of Co yielded a final content of  $88.3 \pm 1.5$  wt. % of Ir,  $5.2 \pm 0.6$  wt. % of Co and  $6.3 \pm 2.0$  wt. % of oxygen. These results were confirmed by inductively coupled plasma atomic emission spectroscopy (ICP-AES) analysis, which yield a content of  $9.3 \pm 1.0$  wt. % Co and  $83 \pm 2.7$  wt. % Ir. Metallic Co is thermodynamically unstable in acid.<sup>94</sup> However, Co may be stabilized from dissolution in acidic electrolyte through interaction with Ir in CoIr300-CL.<sup>95</sup>

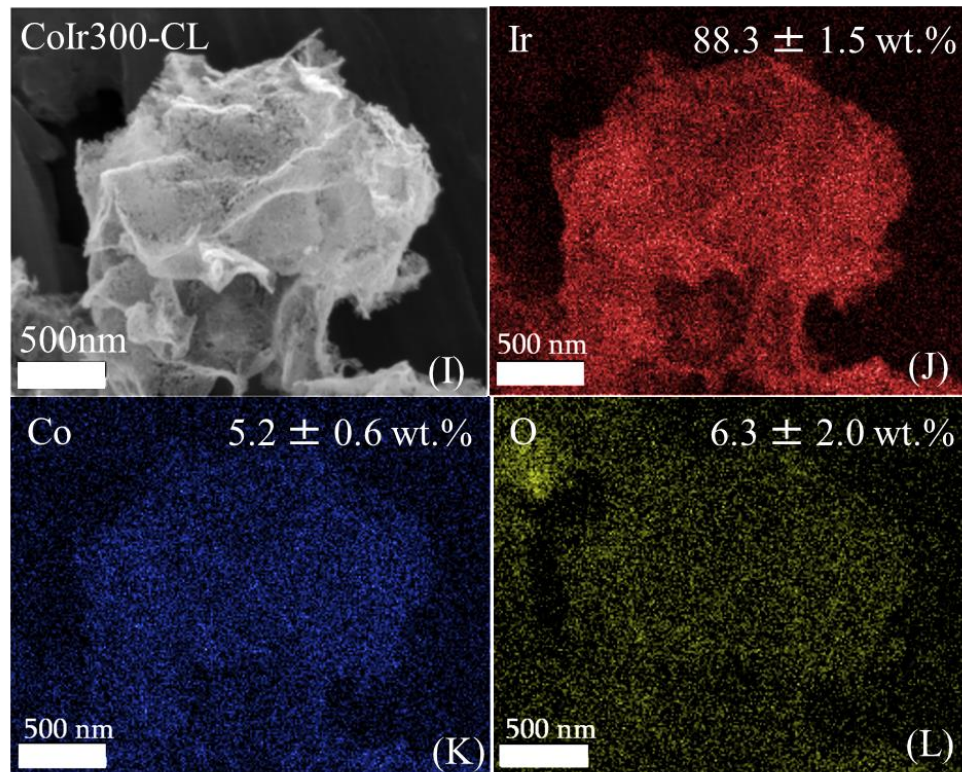


**Figure 19.** Scanning electron microscopy (SEM) images and energy-dispersive x-ray spectroscopy (EDS) mapping analysis of CoIr300-CL showing iridium, cobalt, and oxygen within the structure.

Figure 20 shows the high-angular dark-field scanning TEM (HAADF-STEM) images of CoIr300-CL after chemical leaching. The low magnification STEM image

(Figure 20A) confirmed the extended 2D framework created by interconnected domains forming nanofilaments and a high porous network. The presence of a high variety of pore sizes might play an important role during kinetic reaction and mass transport processes. The mesopores (2 ~ 50 nm) within the structure provide high surface areas for the catalyst and are accessible to the electrolyte and reactants at rapid timescales.<sup>92, 93</sup> The high-resolution HAADF-STEM image (Figure 20B) and selected-area fast Fourier transform (FFT) pattern (Figure 20D), demonstrated the single-crystalline nature of the domains within the material. The intensity profile showed an averaged lattice spacing of  $0.213 \pm 0.009$  nm attributed to the (111) facet of bimetallic CoIr<sub>300</sub>-CL with fcc iridium phase.

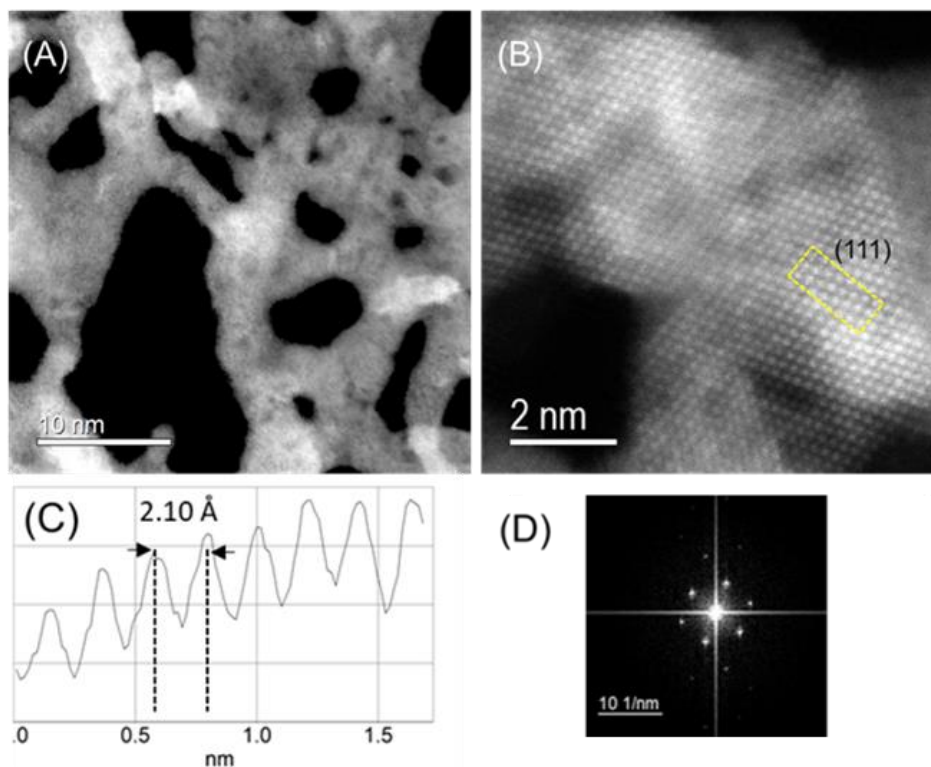


**Figure 20.** Low-magnification (A) and high resolution (B) HAADF-STEM images of CoIr<sub>300</sub>-CL catalyst; the yellow square indicates the HAADF-STEM intensity profile and remarks the interplanar distance associated with (111) lattice plane (C); FFT pattern (D).

### 3.2.2. X-ray Diffraction Characterization of cobalt-iridium catalyst and precursor materials

The transformation of the structures upon the synthesis was followed by XRD as shown in Figure 21. Diffraction patterns of reference materials of  $\alpha$ -Co(OH)<sub>2</sub>(COD-01-074-1057), Co<sub>3</sub>O<sub>4</sub>(COD-00-042-1467), metallic Co(COD-00-015-0806) and metallic Ir(COD-00-006-0598) phases are also shown. The XRD pattern of the Co(OH)<sub>2</sub> nanosheets exhibited a strong reflection at a  $2\theta$  value of 12.1°, assigned to the (001) basal plane due to preferential orientation of the nanosheets.<sup>96</sup> The slight differences of the diffraction angles of the synthesized  $\alpha$ -Co(OH)<sub>2</sub> compared with a prior study<sup>96</sup> may be related with changes of the interlayer spacing and structural disorder produced by the presence of different intercalated anions and/or water content.<sup>96-99</sup>

After Ir deposition, the XRD pattern of Co(OH)<sub>2</sub>:Ir showed the strong peak associated with the (001) basal plane of Co(OH)<sub>2</sub> disappeared, while small peaks around 18° and 60° associated with a Co<sub>3</sub>O<sub>4</sub> phase showed up. The disappearance of the (001) peak and the formation of cubic Co<sub>3</sub>O<sub>4</sub> phase might be linked to the displacement of oxygen by Ir species due to the galvanic displacement, which modify the oxygen stoichiometry due to oxygen depletion.<sup>100</sup>

After thermal treatment, significant structural modifications and phase changes were observed in the XRD patterns of CoIr300. The XRD pattern of CoIr300 showed wide peaks between 40° to 50° that can be assigned to a poorly crystalline metallic CoIr phase. In addition to metallic Co, some Co<sub>3</sub>O<sub>4</sub> still remained (18°, 32°, 37° and 65°).<sup>96</sup>

After the acidic treatment, within CoIr300-CL most of the Co species not incorporated within the Ir structure were removed as shown from EDS analysis (Figure

19). Within the XRD pattern of CoIr300-CL, the peaks at  $41.2^\circ$  and  $46.9^\circ$  were associated with (111) ( $2\theta = 40.66^\circ$ ) and (200) ( $2\theta = 47.31^\circ$ ) of metallic Ir. The peak position of the Ir(111) reflection revealed a shift from a characteristically Ir lattice to higher  $2\theta$  values. The analysis of lattice constant from the (111) peak revealed a change into the iridium lattice constant from  $3.831 \text{ \AA}$ , considered as standard, to  $3.772 \text{ \AA}$  in the CoIr300-CL material. This lattice change corresponded to  $\sim 1.6 \%$  lattice contraction. These observations showed a lattice disruption of iridium likely due to the inclusion of residual Co within Ir structure, in agreement with STEM data (Figure 20). In addition, a very low intensity peak around  $36^\circ$  and  $60^\circ$  assigned to trace  $\text{Co}_3\text{O}_4$  as impurity was still observed.

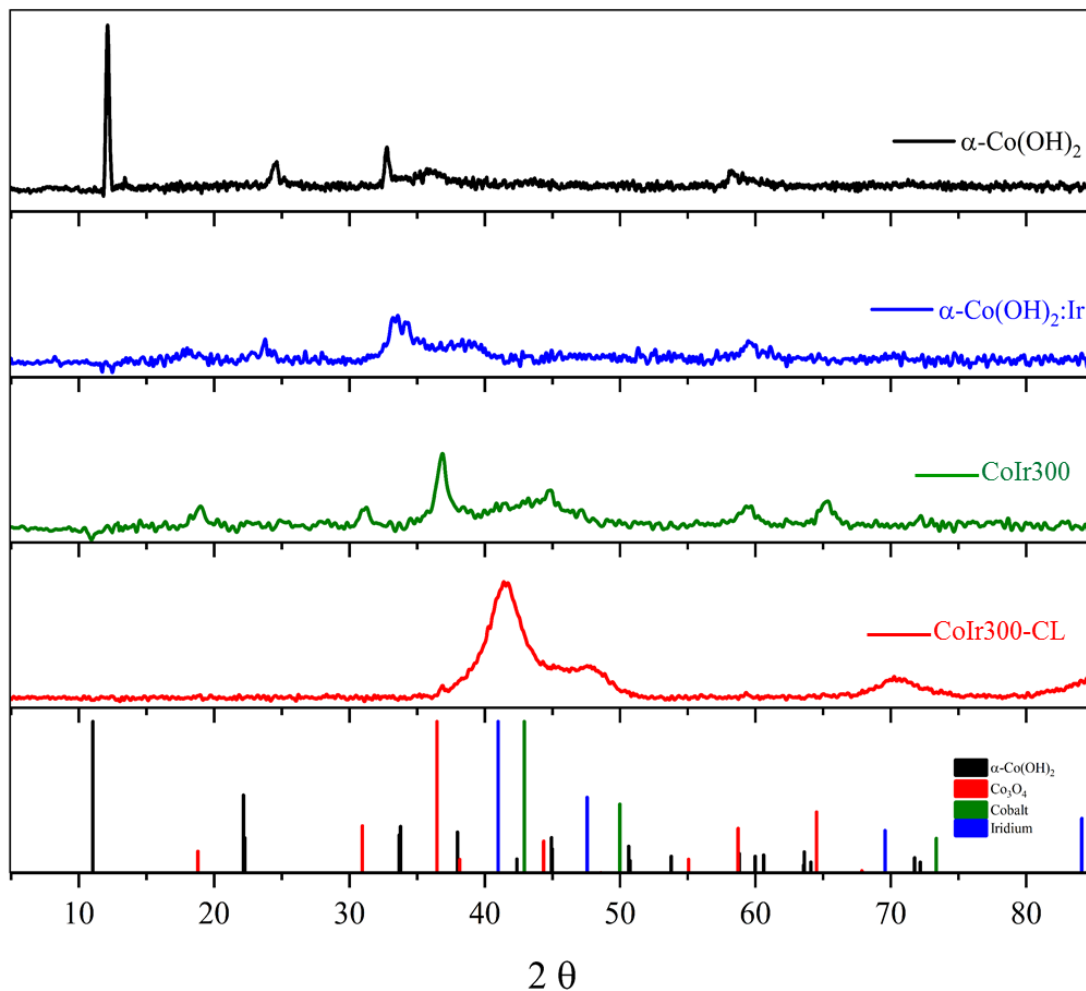


**Figure 21.** X-ray diffraction (XRD) patterns of as-prepared catalysts and their corresponding references:  $\alpha$ -Co(OH)<sub>2</sub>, Co<sub>3</sub>O<sub>4</sub>, Co, and Ir.

### 3.2.3. Infrared Spectroscopic Characterization of cobalt-iridium catalyst and precursor material

Figure 22 shows the transmission FTIR spectra of CoIr300 and CoIr300-CL. The FTIR spectrum of CoIr has only two defined peaks at 670 and 578 cm<sup>-1</sup> which are consistent with Co<sub>3</sub>O<sub>4</sub> modes based on a prior study that reported two distinct and sharp bands at 568 ( $\nu_1$ ) and 664 ( $\nu_2$ ) cm<sup>-1</sup> which originate from the stretching vibrations of the Co–O bonds within Co<sub>3</sub>O<sub>4</sub> spinel oxide.<sup>102</sup> The  $\nu_1$  band is characteristic of Co<sup>3+</sup>–O

vibration in the octahedral site, and  $\nu_2$  band is attributed to  $\text{Co}^{2+}\text{-O}$  vibration in tetrahedral site in the spinel lattice.<sup>103</sup> The X-ray diffraction data (Figure 21) showed the presence of peaks consistent with  $\text{Co}_3\text{O}_4$ . It is also possible that the  $578\text{ cm}^{-1}$  band originated from a Ir-O stretching mode based on a prior study;<sup>104</sup> however, our X-ray diffraction data did not show the presence of any  $\text{IrO}_x$  phase.

The FTIR spectrum of CoIr300-CL has no observable peaks, suggesting that the chemical leaching process removes cobalt oxide to yield a metallic CoIr phase. The absence of the  $646\text{ cm}^{-1}$  absorption was consistent with XRD data which indicated that most of the  $\text{CoO}_x$  not incorporated into the Ir structure was removed following acid treatment.

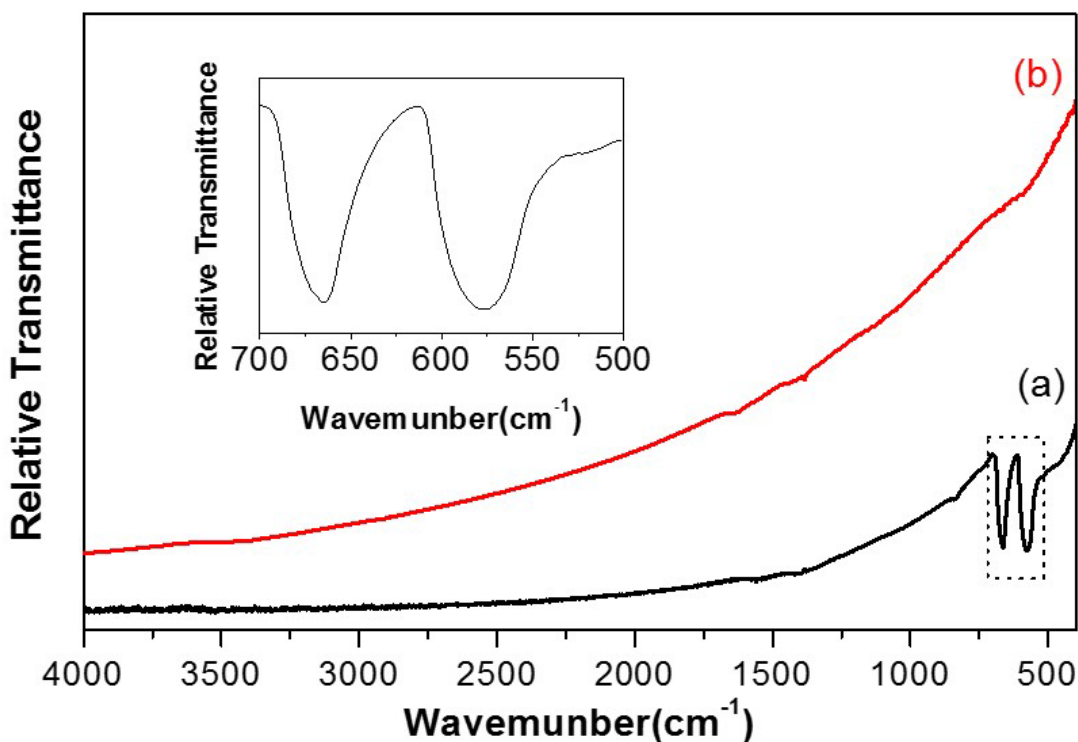


**Figure 22.** Transmission Fourier-transform infrared spectra (FT-IR) of (a) CoIr300; and (b) CoIr300-CL obtained using KBr pellets. Inset shows a magnification of the absorption bands at  $670\text{ cm}^{-1}$  and at  $578\text{ cm}^{-1}$  of CoIr300.

### 3.2.4. Characterization of CoIr300-CL Using Cyclic Voltammetry and Carbon Monoxide Stripping Voltammetry

Cyclic voltammetry (CV) was used to characterize the surface after chemical leaching and following an electrochemical oxidation protocol (Figure 23). After conditioning by cycling at low potential range ( $E \leq 1.0 \text{ V}_{\text{RHE}}$ ) in  $\text{O}_2$ -free 0.1 M  $\text{HClO}_4$ , the CoIr300-CL catalyst (Figure 23A, black curve) exhibited distinctive H-adsorption and H-desorption features associated with hydrogen underpotential deposition ( $\text{H}_{\text{upd}}$ ) on metallic Ir.<sup>105</sup> The presence of H-adsorption and H-desorption features supports that a stable metallic Ir-rich surface was formed after the chemical leaching step. In addition, oxidation/reduction peaks due to reversible  $\text{IrO}_x$  formation/reduction at  $E \geq 0.5 \text{ V}_{\text{RHE}}$  were also observed.<sup>105</sup> This is consistent with the metallic phase observed from STEM measurements (Figure 20).

For the CoIr300-CL material, the electrochemical surface area (ECSA) of Ir determined by CO-stripping (Figure 23B) was  $61.2 \pm 3.1 \text{ m}^2 \text{ g}^{-1}$  for CoIr-CL which is comparable with BET surface areas ( $66.8 \pm 4.7 \text{ m}^2 \text{ g}^{-1}$  for CoIr-CL) supporting the high segregation of Ir on the surface. Since our prior work on NiIr nanoframe OER catalysts shows that the metallic surface of the electrocatalyst is altered after cycling to the potentials required for OER,<sup>91</sup> an “electrochemical oxidation” step (notated with an “EO” subscript) comprising 60 scans between 0.05-1.5  $\text{V}_{\text{RHE}}$ , was carried out. This procedure allows the catalysts to have a more representative surface structure upon which the OER reaction takes place. The catalyst after the EO step is labeled as CoIr300-CL<sub>EO</sub> (Figure 23A-blue curve).

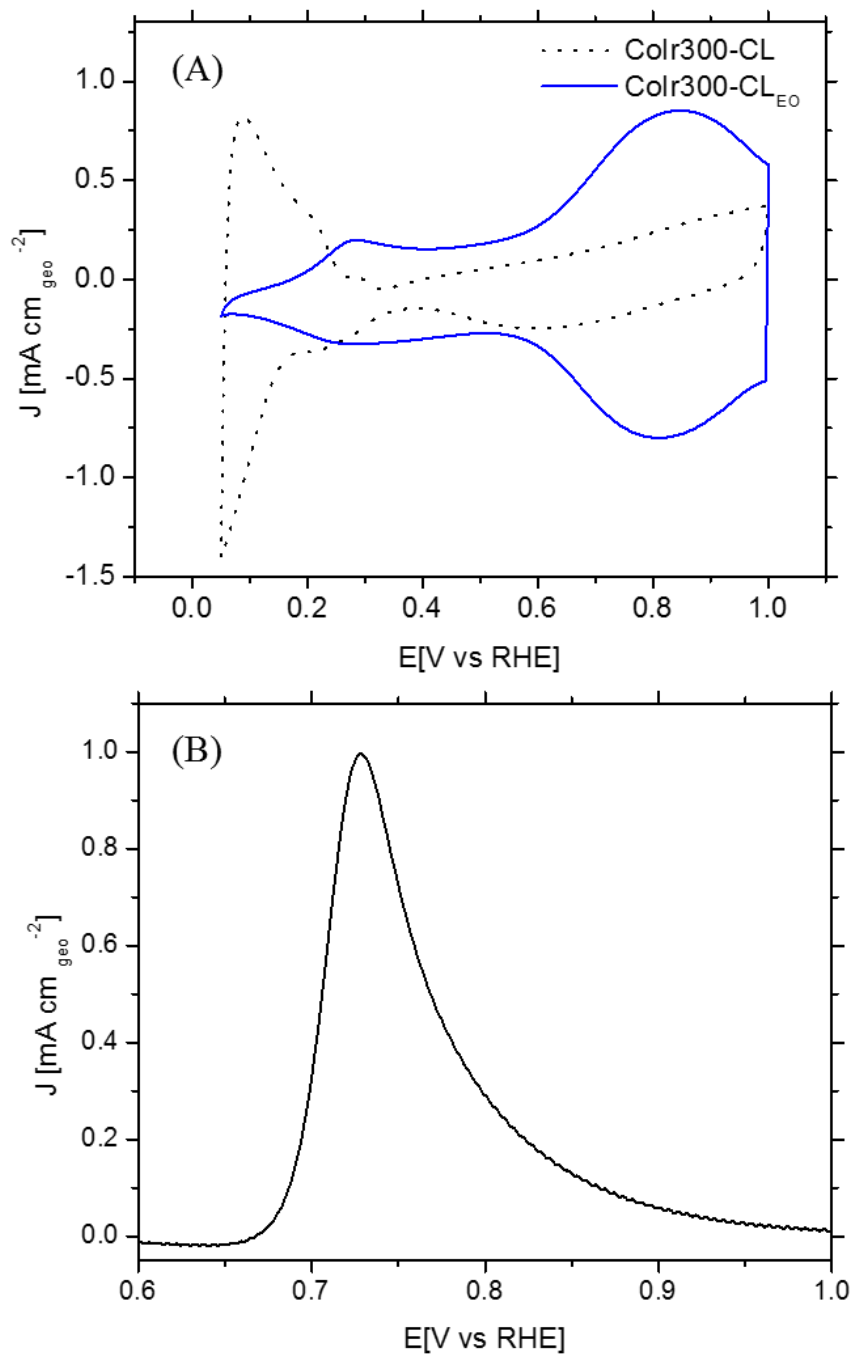


**Figure 23.** Initial and after electrochemical oxidation cyclic voltammograms (CVs) of CoIr-CL (A) and (B) carbon monoxide (CO) stripping voltammetry of CoIr300-CL.

After electrochemical oxidation, the peaks due to  $H_{\text{upd}}$  features were no longer observed, and instead, two broad peaks around  $0.27 V_{\text{RHE}}$  and  $0.82 V_{\text{RHE}}$  consistent with a

hydroxide/oxide surface were observed.<sup>105</sup> The anodic peaks centered  $\sim 0.27$  V<sub>RHE</sub> are attributed to the formation of Ir<sup>3+</sup>-OH species<sup>106</sup> and connected to the oxidation of Ir<sup>3+</sup>-OH<sub>2</sub> groups to Ir<sup>4+</sup>-OH groups,<sup>108</sup> while the peak at  $\sim 0.82$  V<sub>RHE</sub>, is attributed to the transition from Ir<sup>3+</sup> (iridium hydroxide) to Ir<sup>4+</sup> species (IrO<sub>2</sub> or IrO(OH)<sub>2</sub>).<sup>107, 108</sup>

The comparison of the CVs of CoIr300-CL<sub>EO</sub> with IrO<sub>2,EO</sub> (Figure 24) shows that both materials have peaks at lower potentials (0.2~0.5 V<sub>RHE</sub>), attributed to hydrated Ir<sup>3+</sup>-OH species. The anodic peak centered at  $\sim 0.27$  V<sub>RHE</sub> within CoIr300-CL<sub>EO</sub> occurs at a lower potential compared with the anodic peak within IrO<sub>2,EO</sub> that occurs at  $\sim 0.41$  V<sub>RHE</sub>. The differences in the potentials of peaks within CoIr300-CL<sub>EO</sub> with IrO<sub>2,EO</sub> suggests a different local chemical environment for the hydrated Ir<sup>3+</sup>-OH species at the surface of CoIr300-CL<sub>EO</sub> and IrO<sub>2,EO</sub>.

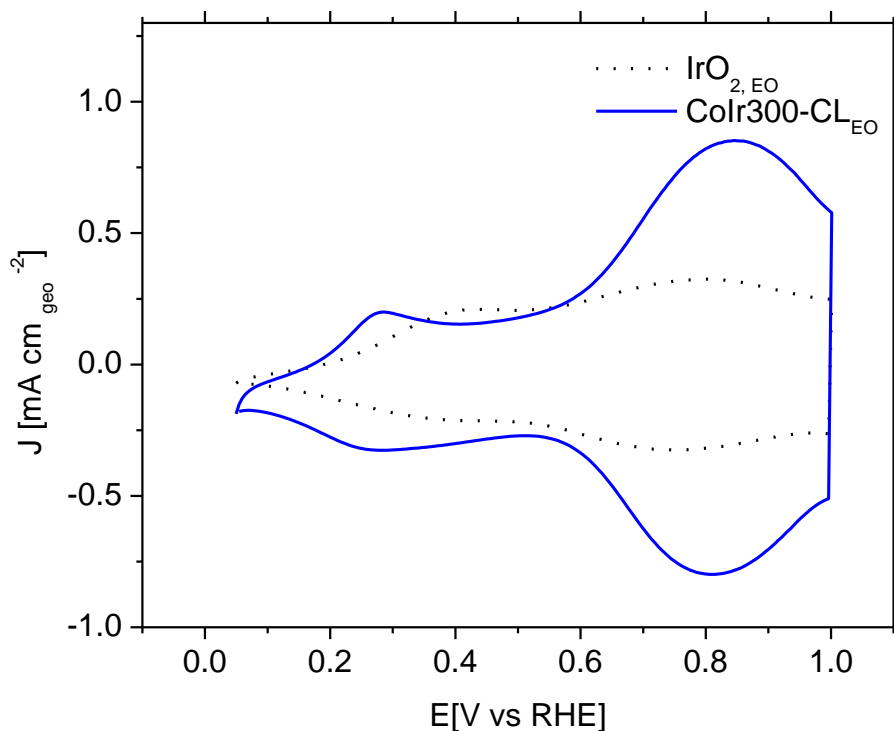


**Figure 24.** Cyclic voltammetry (CV) scans after Au-disk background correction of CoIr300-CL<sub>EO</sub> and commercial IrO<sub>2,EO</sub>.

### 3.2.5. Evaluation of Electrochemical Oxygen Evolution Activity and Stability of CoIr300-CL

Following the electrochemical oxidation step, the catalyst material was electrochemically tested in the OER potential region using a rotating disc electrode (RDE) configuration HClO<sub>4</sub> based on previously reported methods by our group<sup>91</sup> and other groups<sup>71</sup> and compared with commercial IrO<sub>2</sub> from Alfa Aesar. Figure 26 shows chronoamperometric polarization curves normalized versus mass of Ir determined by ICP analysis both after the electrochemical oxidation step and after an accelerated durability testing (ADT) protocol. Chronoamperometry rather than linear sweep voltammetry was used to reduce the contribution of electrochemical double layer capacitance.<sup>57</sup> The CoIr300-CL<sub>EO</sub> catalyst shows a lower onset potential of OER compared to commercial IrO<sub>2,EO</sub> indicating less energy is needed to initiate the reaction on the surface of CoIr300-CL<sub>EO</sub>. Additionally, the CoIr300-CL<sub>EO</sub> catalyst provides a higher current density at high potentials in comparison with commercial IrO<sub>2,EO</sub>.

For catalyst stability testing, an accelerated durability test (ADT) applying a constant potential of 1.6 V for 13.5 hours was used. This protocol had been previously utilized to evaluate the durability of a number of iridium-based catalysts.<sup>60, 110</sup> As shown in Figure 26, both of CoIr300-CL<sub>EO</sub> and commercial IrO<sub>2,EO</sub> exhibited a drop of current density after ADT.

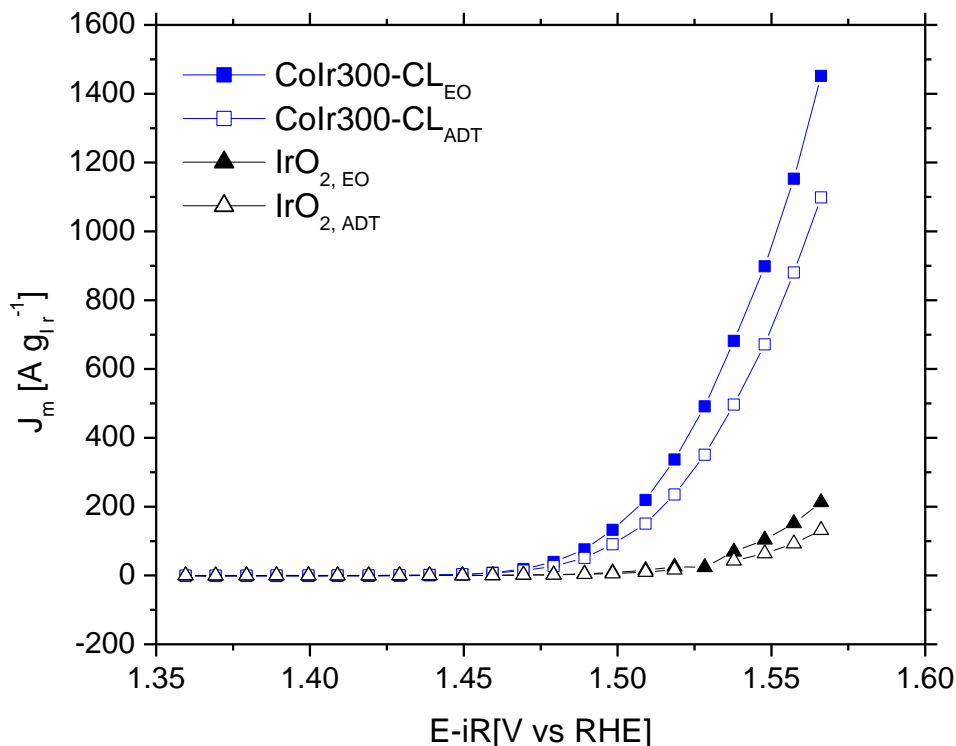


**Figure 25.** Current in the oxygen evolution reaction (OER) voltage region determined from chronoamperometry measurements of CoIr300-CL<sub>EO</sub> and commercial IrO<sub>2,EO</sub> before and accelerated durability testing in O<sub>2</sub>-free 0.1 M HClO<sub>4</sub>. The stability was carried out using a potentiostatic procedure by holding the working electrode at 1.6 V<sub>RHE</sub>-iR-corrected for 13.5 hours under rotation at 2500 rpm.

In order to determine the specific activity, the analysis of ECSA after electrochemical oxidation was carried out by determining the pseudocapacitance following previous reports.<sup>93, 111</sup> The ECSA<sub>IrO<sub>2</sub></sub> value of CoIr300-CL<sub>EO</sub> determined from pseudocapacitance measurements (data shown in Figure 25) was determined to be  $20.1 \pm 2.49 \text{ m}^2 \text{ g}^{-1}$  which is much lower than the calculated ECSA<sub>Ir</sub> ( $61.2 \pm 3.12 \text{ m}^2 \text{ g}^{-1}$ ). It is possible that agglomeration of particles on the 3D structure and/or growth of the oxide/hydroxide film hinders electrolyte and reactant access to the catalyst surface.<sup>92, 112</sup> The ECSA<sub>IrO<sub>2</sub></sub> of commercial IrO<sub>2,EO</sub> was determined to be  $25.3 \pm 1.5 \text{ m}^2 \text{ g}^{-1}$ , which is

similar to the  $\text{ECSA}_{\text{IrO}_2}$  values of CoIr300-CL<sub>EO</sub>. The IrO<sub>2</sub> electrochemical surface area of CoIr300-CL<sub>EO</sub> after ADT determined from pseudocapacitance measurements in Figure 25 is  $12.0 \pm 3.1 \text{ m}^2 \text{ g}^{-1}$  which exhibited  $59.7 \pm 7 \%$  retention which is associated with the loss of active site and may come from dissolution of catalyst or nanostructure growth.<sup>113</sup>

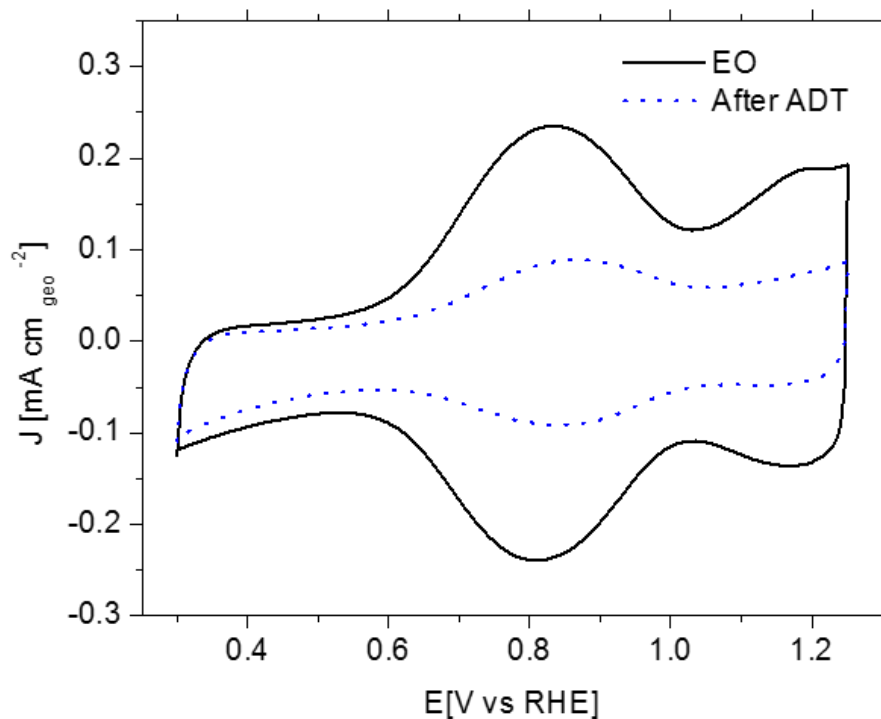


**Figure 26.** Cyclic voltammetry (CV) scans after Au-disk background correction of CoIr300-CL<sub>EO</sub> before and after accelerated durability testing used to determine pseudocapacitive charge. Pseudocapacitive charge was determined using the oxidation scan.

A Tafel slope is a commonly used factor for evaluating the activity of an electrocatalyst and can also give some mechanistic insight to the catalyzed reaction at the electrode.<sup>16</sup> The Tafel slope (Figure 27) of CoIr300-CL<sub>EO</sub> ( $45 \pm 4 \text{ mV dec}^{-1}$ ) is similar to the Tafel slopes of IrO<sub>2,EO</sub> ( $37 \pm 3 \text{ mV dec}^{-1}$ ), suggesting similar reaction mechanisms. The measured Tafel slope of CoIr300-CL<sub>EO</sub> ( $45 \pm 4 \text{ mV dec}^{-1}$ ) supports the second

electron transfer step as the rate determining step<sup>114</sup> based on the four step reaction mechanism proposed by Rossmeisl et al.<sup>115</sup> The Tafel slopes of CoIr300-CL<sub>EO</sub> and IrO<sub>2,EO</sub> do not change significantly after ADT which suggests that the reaction mechanism and possibly the nature of active sites on the surface remained similar before and after ADT.

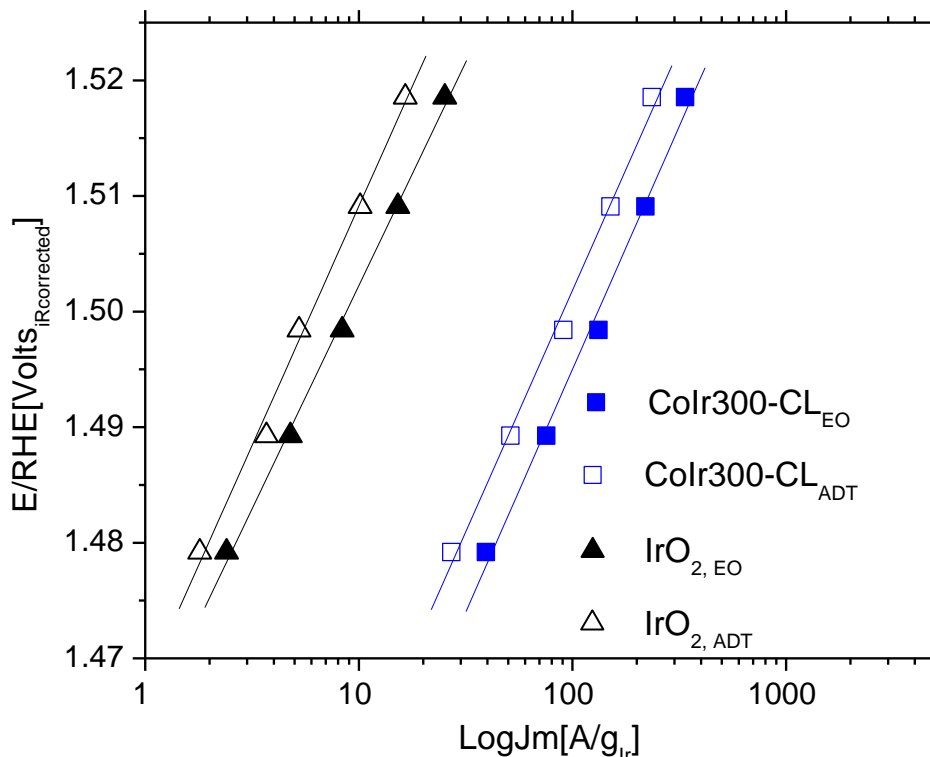


**Figure 27.** Tafel slopes before and after accelerated durability testing determined by chronoamperometry. The potential (iR-corrected) was set between 1.47 V<sub>RHE</sub> to 1.52 V<sub>RHE</sub> to reduce the mass transport contribution.

The CoIr300-CL<sub>EO</sub> material exhibited a significantly higher mass-normalized current than the commercial IrO<sub>2,EO</sub> material in Figure 26. To evaluate the mass activity, the current at 1.51 V<sub>RHE</sub> was normalized for the Ir mass determined by ICP-MS analysis (83 ± 2.7 wt. %). A potential of 1.51 V<sub>RHE</sub> was used since the Tafel plot (Figure 27) still shows linear behavior within this voltage region, and lower overpotentials relative to the

thermodynamic potential of the reaction also minimize the contributions of mass transport. The mass-normalized OER activities of the CoIr300-CL<sub>EO</sub>, and IrO<sub>2,EO</sub> at 1.51 V<sub>RHE</sub> are compared in Figure 28(A). The CoIr300-CL<sub>EO</sub> catalyst showed significantly higher mass activity than the commercial IrO<sub>2,EO</sub> catalyst. At a potential of 1.51 V<sub>RHE</sub>, the mass activity of CoIr300-CL<sub>EO</sub> ( $211 \pm 24 \text{ A gr}^{-1}$ ) is 14 times higher than the mass activity of IrO<sub>2</sub> ( $15 \pm 3 \text{ A gr}^{-1}$ ). The OER specific activity was determined by normalizing the current to the electrochemical surface area determined from pseudocapacitance. As shown in Figure 28(B), the OER specific activity at 1.51 V<sub>RHE</sub> was  $1.05 \pm 0.15 \text{ A cm}_{\text{IrO}_2}^{-2}$  for CoIr300-CL<sub>EO</sub> which is significantly higher (17 times higher) than the OER specific activity of  $0.049 \pm 0.015 \text{ A cm}_{\text{IrO}_2}^{-2}$  for commercial IrO<sub>2</sub>.

The significantly higher mass activity of CoIr-CL<sub>EO</sub> compared with IrO<sub>2</sub> was driven by a higher intrinsic activity and higher Ir utilization. The higher activity of CoIr300-CL<sub>EO</sub> versus the commercial IrO<sub>2</sub> catalyst and may be attributed to the presence of a high concentration of Ir-OH surface species which is supported by cyclic voltammetry of CoIr300-CL<sub>EO</sub> and/or interaction of Ir with Co within the structure which is in agreement with XRD and STEM of CoIr300-CL.<sup>106</sup> The anodic peak (~0.27 V) within the cyclic voltammetry of CoIr300-CL<sub>EO</sub> (Figure 24) supports the presence of surface hydrated Ir<sup>3+</sup>-OH species within CoIr300-CL<sub>EO</sub>.<sup>106</sup> A similar peak was observed at higher potential (~0.4 V) on IrO<sub>2</sub>. The difference of anodic potential of the oxidation processes occurring on both CoIr300-CL<sub>EO</sub> and IrO<sub>2</sub> catalysts suggests the surface oxidation reactions have different local chemical potentials and electron densities between the catalysts which may influence the OER activities. The presence of surface hydroxide species has been shown to play an important role in improving the OER

activity.<sup>38, 116</sup>

After the ADT protocol, the specific activity of IrO<sub>2</sub> was reduced by ~25%; however, the specific activity of CoIr300-CL<sub>ADT</sub> showed a slight increase of ~2% (Figure 28B). The reduction of the specific activity of IrO<sub>2</sub> after ADT can be only partially explained by the reduction of ECSA; therefore, other factors must also be involved. In contrast with IrO<sub>2</sub>, CoIr300-CL<sub>EO</sub> showed an increase of specific activity after ADT which is not correlated with the reduction of ECSA of ~23%. These discrepancies suggest the intrinsic activity of active sites on CoIr300-CL<sub>EO</sub> was improved after ADT process which may come from redistribution of Co and Ir during the operation, leading to modification of electron density distribution around the active sites. The commercial IrO<sub>2</sub> samples showed retention of  $71 \pm 7$  % of the initial mass-normalized current after ADT. The CoIr300-CL<sub>EO</sub> catalysts exhibited a relative stability of  $70 \pm 8$  %, indicating a comparable stability with IrO<sub>2</sub>.

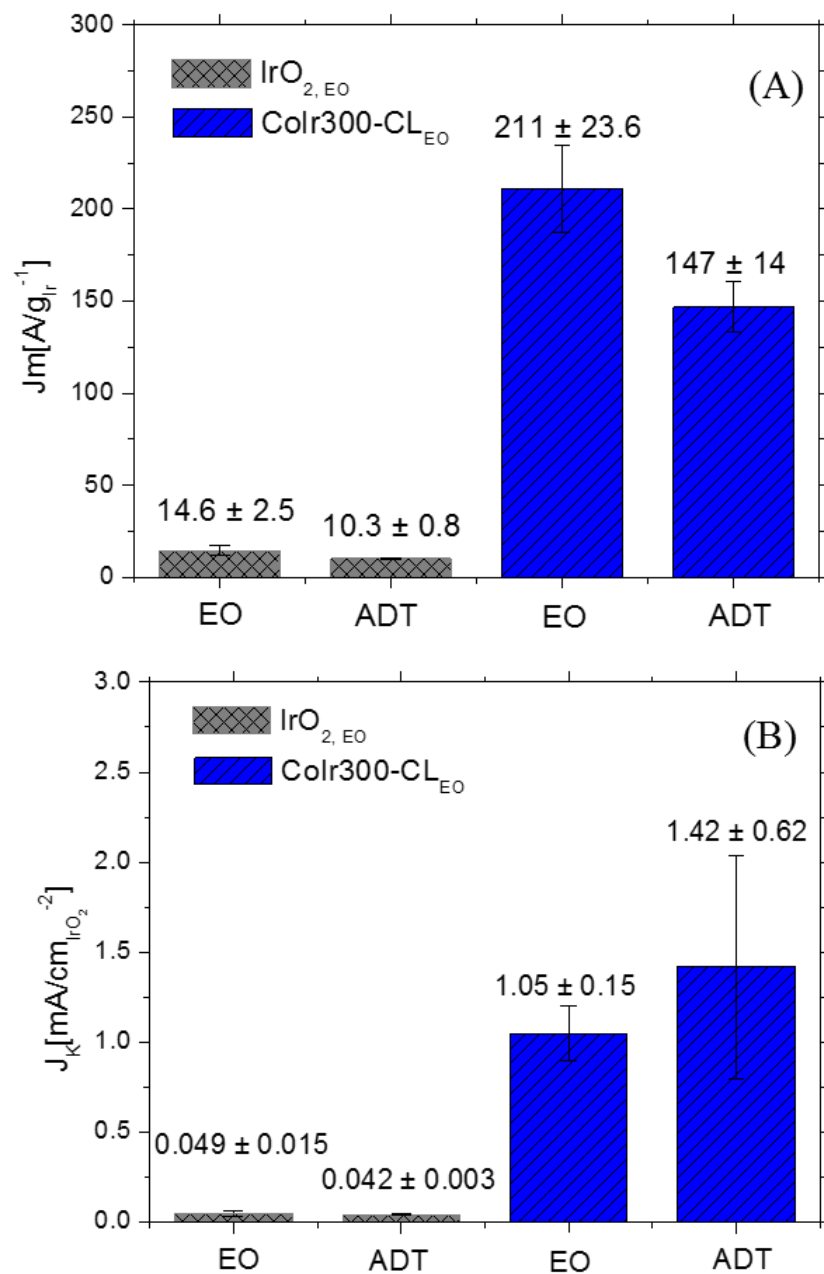


**Figure 28.** Comparison of OER mass activities at 1.51 V<sub>RHE</sub> before and after accelerated durability testing (A); and comparison of OER specific activities at 1.51 V<sub>RHE</sub> before and after accelerated durability testing (B).

**Table 2.** Inductively Coupled Plasma Mass Spectrometry (ICP-MS) analysis of iridium in electrolytes after electrochemical oxidation (EO) and after accelerated durability testing (ADT) of CoIr300-CL and commercial IrO<sub>2</sub>. “-” indicate not measured.

Material	After electrochemical oxidation (EO)		After accelerated durability testing (ADT)	
	Ir wt. % Lost	Ir Degradation rate [pg/s]	Ir wt. % Lost	Ir Degradation rate [pg/s]
IrO <sub>2</sub> -AA	-	-	12.5 ± 0.7	5.4 ± 0.4
CoIr300-CL	10.4 ± 0.3	105 ± 18	20.7 ± 4.9	15 ± 6

Multiple studies have shown that iridium dissolution occurs under the highly oxidative potentials and highly acidic conditions used for acidic oxygen evolution.<sup>117-119</sup> The Ir dissolution rate is also affected by the presence of non-noble metals (i.e. Co, Ni etc.)<sup>57</sup> within the structure as well as the experimental processes used during the electrochemical conditioning and testing of the electrode. The analysis of the percent of iridium dissolved into the electrolyte and its corresponding iridium degradation rate were determined using ICP-MS, and the results are summarized in Table 2. ICP-MS measurements showed that CoIr300-CL catalyst had 20.7 wt % Ir lost within the electrolyte after ADT, which was higher than 12.5 wt % Ir for IrO<sub>2</sub> tested under similar conditions.<sup>57</sup> This shows that some of the activity degradation of the catalyst is due to dissolution of Ir. The high activity of CoIr300-CL<sub>EO</sub> nanoframes may result in higher dissolution as supported by a prior study suggests a direct correlation between the oxygen evolution activity and the corrosion of metal oxides based on the thermodynamic instability of the oxygen anion in the metal oxide lattice.<sup>120</sup>

Due to significant surface changes that occurred for CoIr300-CL during EO, the Ir lost and the degradation rate of Ir after EO were also investigated. Due to the very low degree of changes of IrO<sub>2</sub> during EO, the iridium concentration was not analyzed after

EO. The high dissolution rate of Ir of CoIr300-CL during EO was correlated with the leaching of Co. The lowering of the Ir leaching rate after ADT was attributed to the formation of a passivating surface oxide.

**Table 3.** Comparison of electrode loadings and oxygen evolution reaction (OER) mass activities (normalized for mass of Ir) at 1.51 V<sub>RHE</sub> and 1.55 V<sub>RHE</sub> for electrocatalysts tested in this study and previously reported values.

Material	Support material	Loading ( $\mu\text{g}_{\text{Ir}} \text{cm}^{-2}_{\text{geo}}$ )	$I_m^{1.51V}$ ( $\text{A gr}^{-1}$ )	$I_m^{1.55V}$ ( $\text{A gr}^{-1}$ )	$\eta$ vs RHE, 0.5 mA $\text{cm}^{-2}$	$\eta$ vs RHE, 10 mA $\text{cm}^{-2}$	Tafel slope ( $\text{mV dec}^{-1}$ )	Ref.
CoIr300-CL <sup>(a)</sup>	None	18.8	211 ± 24	823 ± 63	0.23	0.29	45 ± 4	This work
IrO <sub>2</sub> -AA <sup>(a)</sup>	None	11.7	12 ± 4	76 ± 22	0.27	0.36	37 ± 3	<sup>57</sup>
IrCo/C <sup>(b)</sup>	Carbon	10.0	-	-	-	~0.30	76.9	<sup>121</sup>
IrCoNi/C <sup>(b)</sup>	Carbon	10.0	-	-	-	0.303	53.8	
leached-Ir <sub>0.7</sub> Co <sub>0.3</sub> O <sub>x</sub> <sup>(c)</sup>	None	102	-	-	0.26	~0.32	40	<sup>58</sup>
CoIr nanowires <sup>(d)</sup>	None	30.6	594	2327	-	-	-	<sup>60</sup>

(a) Chronoamperometry, argon-saturated 0.1 M HClO<sub>4</sub>, 2500 rpm, iR-corrected

(b) Linear sweep voltammetry, O<sub>2</sub>-saturated 0.1 M HClO<sub>4</sub>; scan rate of 5 mV s<sup>-1</sup>, 95% iR-compensation

(c) Linear sweep voltammetry, O<sub>2</sub>-saturated 0.5 M H<sub>2</sub>SO<sub>4</sub>; scan rate of 5 mV s<sup>-1</sup>, 1600 rpm

(d) Linear sweep voltammetry, 0.1 M HClO<sub>4</sub>, scan rate of 20 mVs<sup>-1</sup>, 2500 rpm, iR-corrected; no-background subtraction

In addition to direct comparison of the OER activity of CoIr300-CL<sub>EO</sub> with IrO<sub>2</sub> from our testing,<sup>91</sup> the OER catalytic activities of CoIr300-CL<sub>EO</sub> were compared with previously reported Co and Ir-based catalysts in Table 3. A direct comparison is difficult due to differences in the experimental conditions such as the type of electrolyte, electrochemical method (i.e. linear sweep voltammetry or chronoamperometry), catalyst loading, potential of the analysis, ohmic drop correction, background subtraction etc., can influence the activity.<sup>91</sup> The OER mass activity of CoIr300-CL<sub>EO</sub> (211 ± 24 A gr<sup>-1</sup>)

showed one of the highest performances for similar Ir-based materials reported to date.

The electrochemical properties of CoIr300-CL nanoframes were compared with a previous study on similarly prepared NiIr-CL nanoframes.<sup>91</sup> The comparison showed many similarities: *i*) similar CV profile attributed to the formation of hydroxide/oxide species; *ii*) similar Tafel slopes which suggests same mechanism pathway; and *iii*) very similar OER activities. The presence of Co within the Ir structure may modify the electron density distribution around the doped sites in a manner very similar to that of Ni.<sup>91</sup> In comparison with the previous NiIr structure<sup>91</sup>, the catalyst CoIr300-CL demonstrated a significant improvement in the stability with 70% of initial activity compared with 52% for NiIr. Considering similar morphologies and structures, this difference in stability might be related to a stronger Ir-Co interaction in comparison with Ir-Ni. Some computational analysis have demonstrated a higher relative formation energy toward Co-doped IrO<sub>2</sub> structure compared with Ni-doped ones.<sup>100</sup>

### 3.3. Effect of heat treatment temperature on catalytic activity and stability of cobalt-iridium oxygen evolution reaction electrocatalyst

#### 3.3.1. Analysis of the morphology, porosity and elemental composition of heat-treated precursors and catalysts.

The effect of temperature treatment on morphology, composition, phase and structure of the CoIr nanoframe catalyst, and how these properties influence activity and stability were investigated. The SEM images for the catalysts calcined at temperatures of 200, 300 and 400°C are shown in Figure 29(A-C). In the SEM image of the CoIr200 (Figure 29A), the material retained a nanosheet morphology which is similar to its Ir-decorated Co(OH)<sub>2</sub> precursor. After thermal treatment at 300 and 400°C (Figure 29 B and

C), the formation of 2D nanoframe structure was observed. After chemical leaching, the catalysts shown a similar porous morphology in SEM images in Figure 29(D-F).

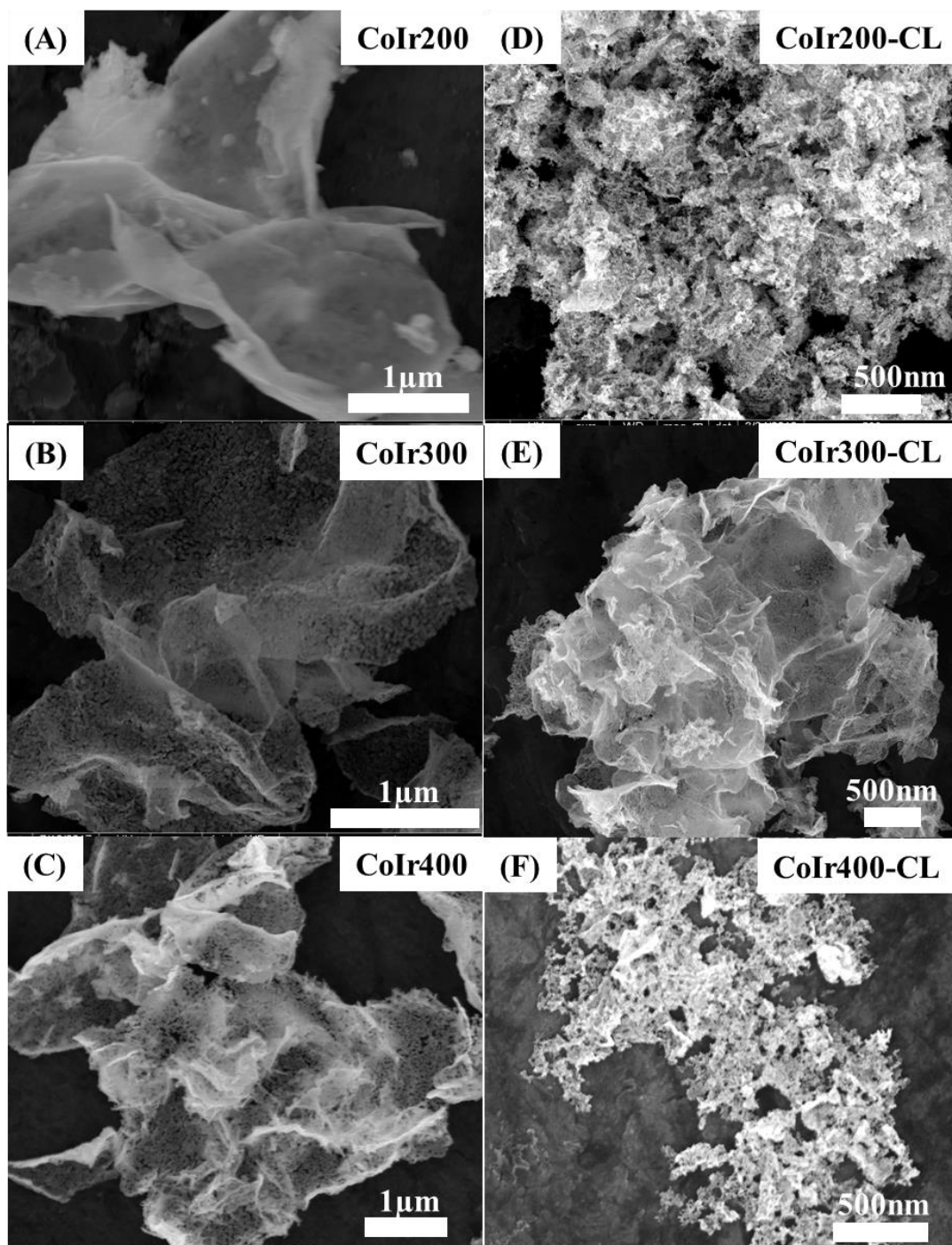


**Figure 29.** Scanning electron microscopy (SEM) images of thermal and chemical treated materials CoIr200(A), CoIr300(B), CoIr400(C), CoIr200-CL(D), CoIr300-CL(E) and CoIr400-CL(F).

**Table 4.** Average Brunauer-Emmett-Teller (BET) surface areas, cumulative pore volumes, and mean pore diameters of precursors.

Material ID	BET surface area ( $\text{m}^2 \text{g}^{-1}$ )	Cumulative pore volume ( $\text{cm}^3 \text{g}^{-1}$ )	Mean pore diameter (nm)
Co(OH) <sub>2</sub> -as prep	70 ± 11	0.31 ± 0.05	18 ± 1
Co(OH) <sub>2</sub> :Ir	43 ± 5	0.15 ± 0.03	13 ± 1
CoIr200	33 ± 3	0.12 ± 0.00	15 ± 1
CoIr300	32 ± 1	0.15 ± 0.03	18 ± 3
CoIr400	15	0.11	21

The BET surface areas of the heat-treated catalysts and precursors shown in Table 4 support that the surface area decreases as the heat treatment temperature increased. The mean pore diameter is increased from 15 nm to 21 nm as the temperature increased from 200 to 400°C. The nitrogen adsorption and desorption isotherms of heat-treated precursors are shown in Figure 30A, C and E. The isotherms can be divided into three regions: low pressure region ( $P/P_0 < 0.1$ ), intermediate pressure region ( $0.1 < P/P_0 < 0.8$ ), and high pressures region ( $0.8 < P/P_0$ ). In the low pressure region, the nitrogen adsorption and desorption increased slowly. In the intermediate region, nitrogen isotherm behavior was very close to linear. In the high pressure region, the nitrogen adsorption and desorption increase sharply to  $P/P_0 = 1$ . The type of isotherm of the heat-treated precursors are Type II according to the international union of pure and applied chemistry (IUPAC) classification of adsorption isotherms.<sup>122</sup> The data in Figure 30A, C and E are shows that the quantity of nitrogen uptake of the heat-treated precursors at each relative pressure follow the order of CoIr300 > CoIr200 > CoIr400. This indicates CoIr300 has the highest porosity and surface area. As shown in Figure 30B, D and F, pore volume trends follow the same order as the quantity of nitrogen uptake.

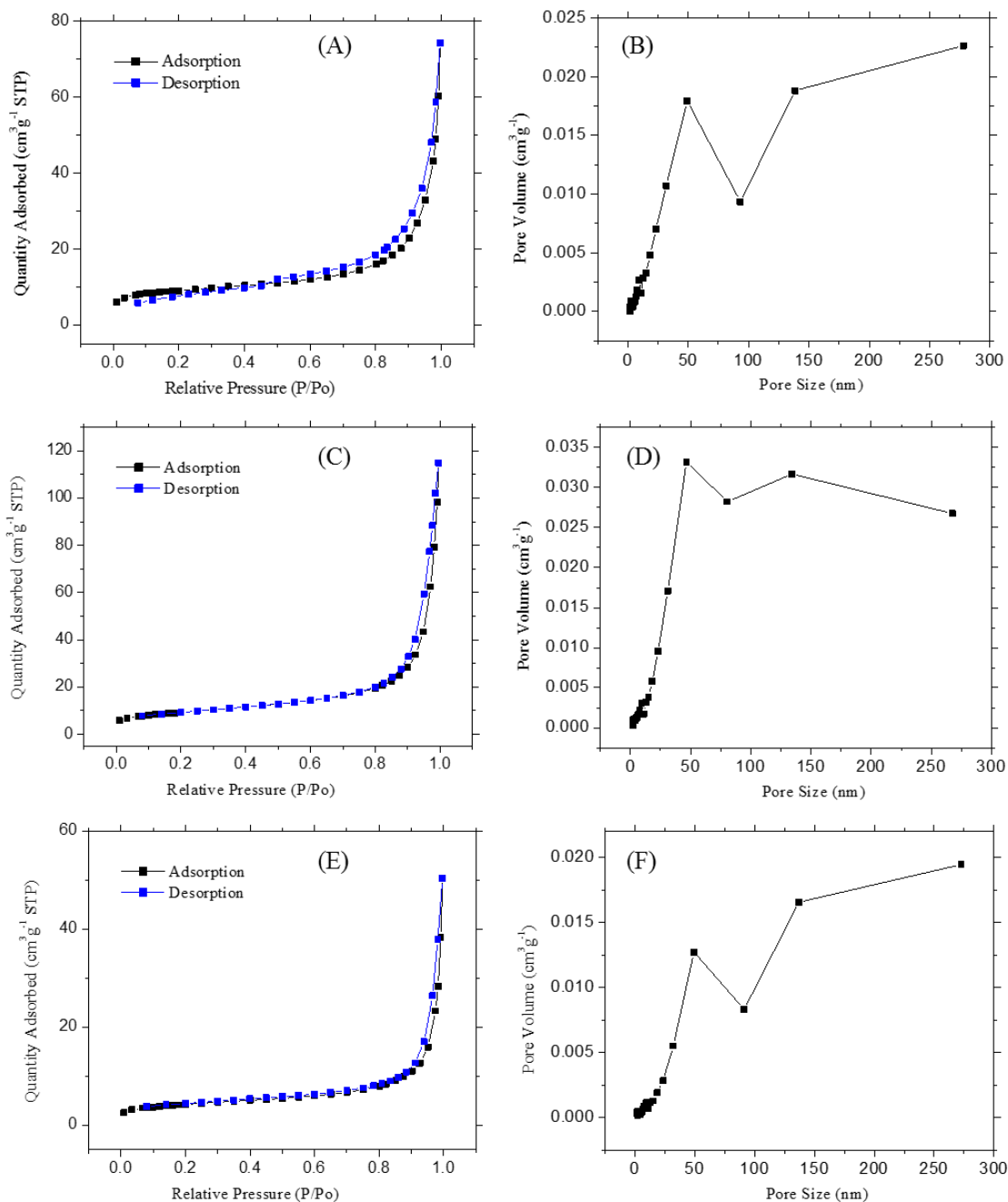


**Figure 30.** Nitrogen physisorption isotherm and pore-size distribution plot of CoIr200 (A-B), CoIr300 (C-D), CoIr400 (E-F).

The EDS measurements were used to perform elemental analyses. The EDS elemental analysis of heat-treated materials is shown in Figure 31. The CoIr200 sample

contained  $30.0 \pm 3.4$  wt. % of O, which is much higher than CoIr300 and CoIr400 ( $17.3 \pm 4.3$  wt. % and  $16.0 \pm 2.4$  wt. % respectively). The elimination of oxygen may come from water releasing from the structure and the transformation of  $\text{Co}(\text{OH})_2$  to  $\text{Co}_3\text{O}_4$  which is supported by XRD analysis.

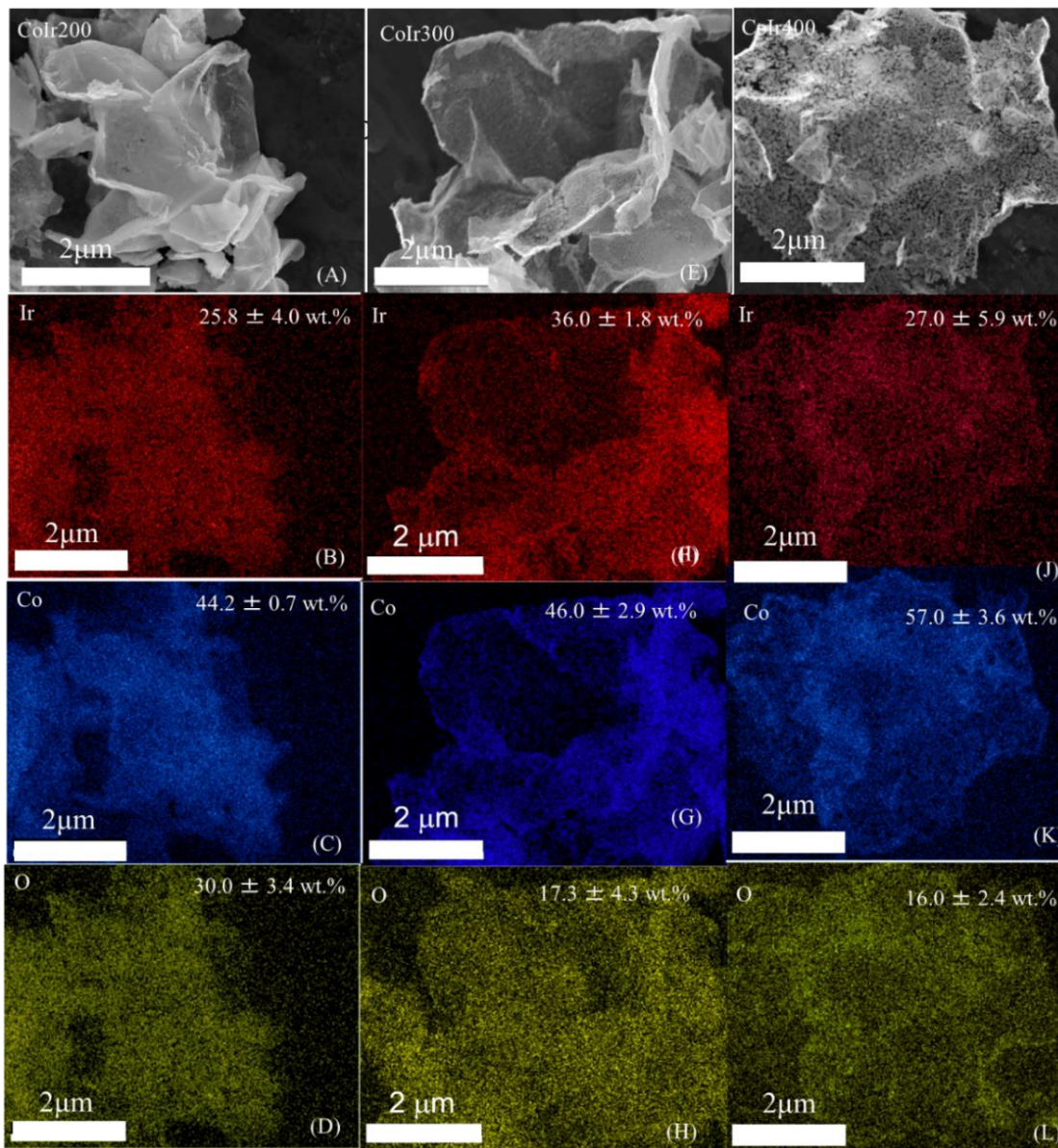


**Figure 31.** Scanning electron microscopy (SEM) images and energy-dispersive x-ray spectroscopy (EDS) mapping analysis of CoIr200 (A-D); CoIr300 (E-H); CoIr400 (I-L), showing iridium, cobalt, and oxygen within the structures.

EDS mapping images of the three catalysts in Figure 32 revealed that Co and Ir

are homogeneously distributed at this scale. In Table 5, the atomic ratios of Ir, Co and O are shown. The Ir:Co atomic ratio in acid leached catalysts were increased compared to heat-treated materials due to the selective removal of Co. The Ir to O atomic ratio in CoIr400-CL (1:2) is lower than CoIr200-CL and CoIr300-CL which were very close to 1:1. Although metallic Co is thermodynamically unstable in acid, Co was observed in chemically leached catalyst, which suggests that Co was stabilized from dissolution in acidic solution through interaction with Ir.<sup>95</sup>

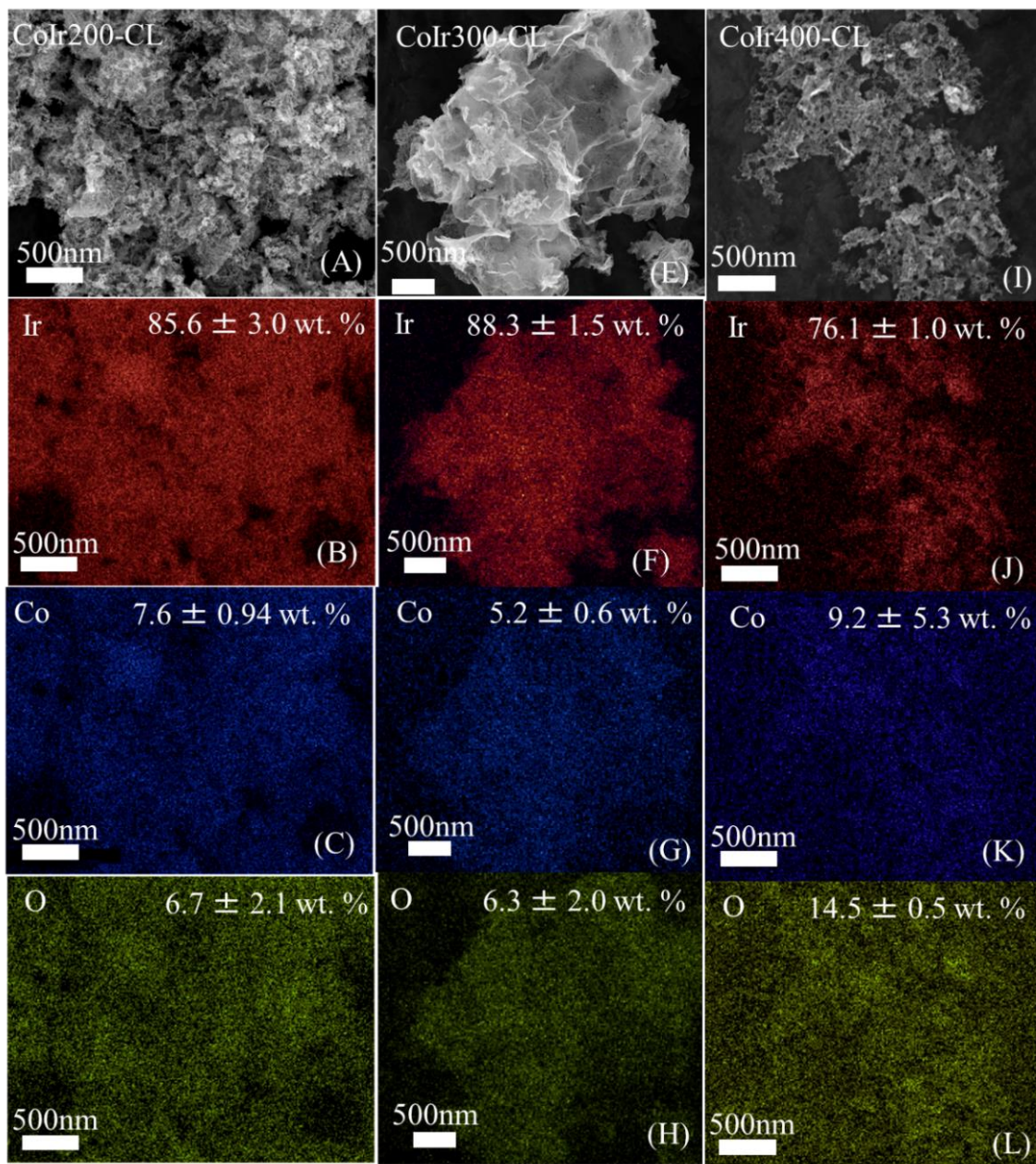


**Figure 32.** Scanning electron microscopy (SEM) images and energy-dispersive x-ray spectroscopy (EDS) mapping analysis of CoIr200-CL (A-D); CoIr300-CL (E-H); CoIr400-CL (I-L), showing iridium, cobalt, and oxygen within the structures.

**Table 5.** Relative elemental composition and ratios of Ir and Co within catalysts determined by Energy Dispersive x-ray Spectroscopy (EDS).

Material	Ir, atomic %	Co, Atomic %	O, atomic %	Ir:Co:O atomic ratio	Formula
CoIr200-CL	45.3 ± 5.4	13.0 ± 0.1	41.7 ± 5.4	1:0.3:0.9	IrCo <sub>0.3</sub> O <sub>0.9</sub>
CoIr300-CL	45.6 ± 4.7	8.7 ± 1.4	45.7 ± 6.0	1:0.2:1	IrCo <sub>0.2</sub> O
CoIr400-CL	27.1 ± 0.7	10.9 ± 0.3	62.0 ± 0.4	1:0.4:2	IrCo <sub>0.4</sub> O <sub>2</sub>

### 3.3.2. X-ray Diffraction Characterization of heat-treated precursors and catalysts

To further study the effects of temperature treatment, the structures of the thermally treated precursors and final catalysts were determined using powder X-ray diffraction (XRD). The powder XRD patterns for CoIr200, CoIr300 and CoIr400 are shown in Figure 33A along with patterns of reference phases: Co<sub>3</sub>O<sub>4</sub>(COD-00-042-1467), metallic Co (COD-00-015-0806) and metallic Ir (COD-00-006-0598). The lack of peaks within CoIr200 revealed an amorphous structure for this material. The XRD pattern of CoIr300 showed the presence of peaks at 32°, 36°, 59° and 65° that were consistent with Co<sub>3</sub>O<sub>4</sub>.<sup>96</sup> The wide peaks between 40° to 50° can be assigned to a poorly crystalline metallic CoIr phase. As the temperature increased up to 400 °C, three peaks in the 40° to 50 ° range were observed which suggested that the amorphous metallic CoIr are crystallized at higher temperature. The peaks at 41° and 47° can be assigned to hexagonal closed-packed (hcp) phase of CoIr alloy, while the peaks at 44° and 74° can be attributed to the mixture phases of hcp and face-centered cubic (fcc) phase.<sup>123, 124</sup> Previous study shown that the reducing atmosphere is beneficial for efficient second metal element incorporation.<sup>125</sup>

After the acidic treatment, most of the unstable Co species within the structure was removed as shown from EDS analysis (Figure 32). The XRD pattern of the catalysts

after acid leaching(Figure 33B) showed peaks with peak position at approximately  $41^\circ$ ,  $47^\circ$  and  $71^\circ$  which were associated with (111) plane ( $2\theta = 40.66^\circ$ ), (200) plane ( $2\theta = 47.31^\circ$ ) and (220) plane ( $2\theta = 69.14^\circ$ ) of metallic Ir. The peak position of the metallic Ir was shifted to higher  $2\theta$  values. The width of the peaks became more narrow as the temperature increased which indicates an increase in the particle size.<sup>126</sup> The XRD results suggested the progressive growth of Ir nanocrystals as temperatures increased for the heat treatment step after acid leaching.

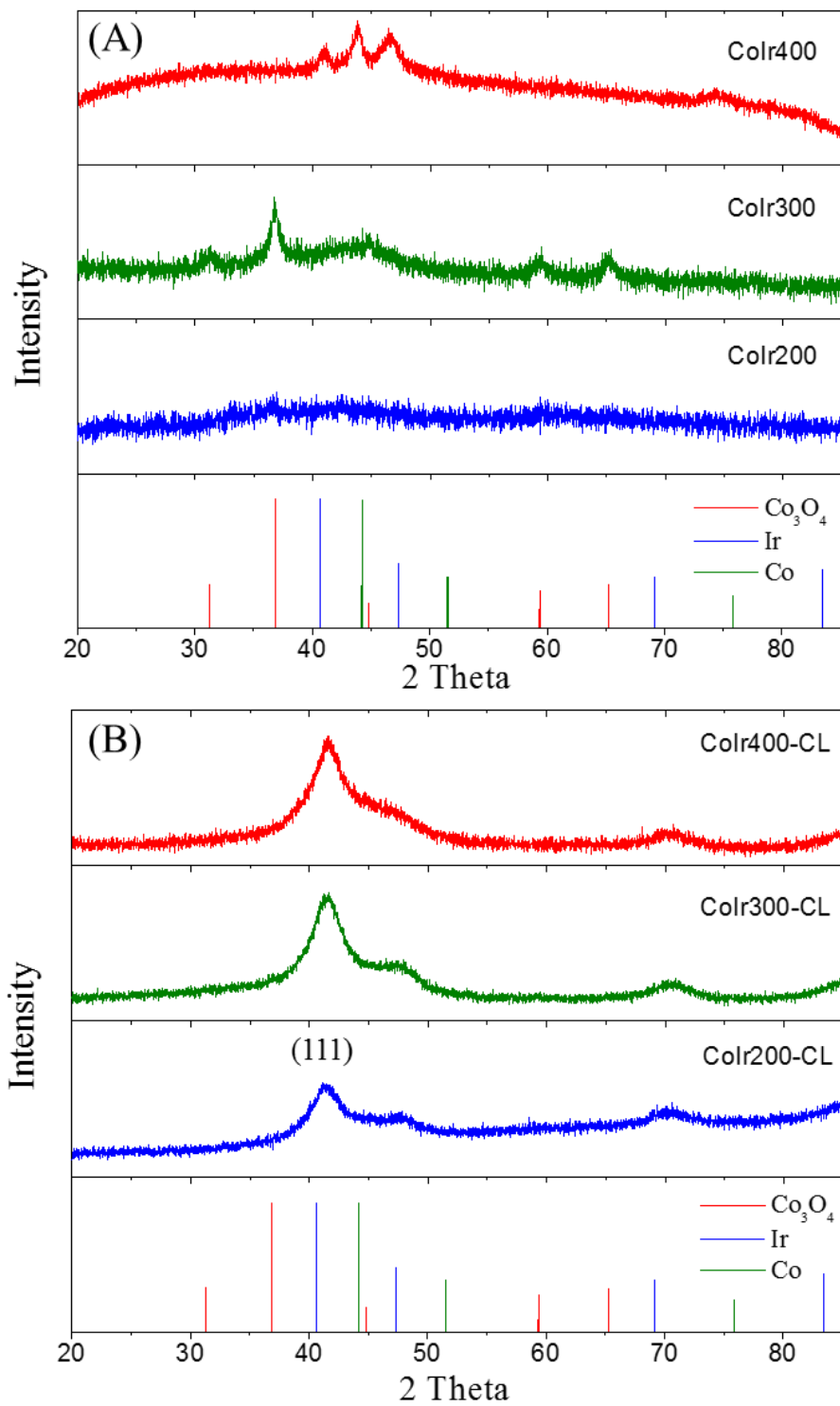


**Figure 33.** X-ray diffraction (XRD) patterns of CoIr materials after different thermal and chemical treatments (CoIr200, CoIr300, CoIr400, CoIr200-CL, CoIr300-CL, CoIr400-CL and their corresponding references:  $\text{Co}_3\text{O}_4$ , Co, and Ir).

**Table 6.** Summary of Peak Positions and Crystallographic Parameters of CoIr200-CL, CoIr300-CL, CoIr400-CL and Reference Standards Obtained from the Crystallography Open Database (COD).

Material	Peak position, $2\theta^\circ$ , (111) peak	d spacing( $\text{\AA}$ )	Lattice constant ( $\text{\AA}$ )	Change in lattice constant ( $\text{\AA}$ ), relative to Ir	FWHM ( $2\theta^\circ$ )	Average particle size (nm)	Reference
CoIr200-CL	41.2976	2.186	3.787	-0.051	0.6298	13.5	-
CoIr300-CL	41.4284	2.178	3.772	-0.066	0.5760	14.7	-
CoIr400-CL	41.5730	2.172	3.763	-0.075	0.5510	15.4	-
Ir std	40.67	2.217	3.838	-	-	-	COD 03-065-9327
Co std	45.92	53.54	3.420	-	-	-	COD 01-088-2325

The d-spacing values and lattice constants of the acid leached catalysts calculated from the (111) peak using a face centered cubic cell are listed in Table 6. The lattice constants are 3.787  $\text{\AA}$ , 3.772  $\text{\AA}$  and 3.763  $\text{\AA}$  for CoIr200-CL, CoIr300-CL and CoIr400-CL, respectively which were smaller than the standard metallic iridium lattice constant of 3.838  $\text{\AA}$ . These observations support a lattice contraction of iridium likely due to the inclusion of residual Co within the Ir structure. From prior work, the interaction of Co would induce lattice strain into the Ir lattice.<sup>68</sup> The higher the temperature is, the more Co remaining in the structure as confirmed by SEM/EDS data of CoIr400-CL (Figure 32).

The crystallite sizes were estimated from the Scherrer equation<sup>76</sup> based on full width at half maximum (FWHM) of the (111) peak. The full width at half maximum (FWHM) intensity in radians is showed in Table 6. The calculated crystallite sizes are about 13.5 nm, 14.7 nm and 15.4 at 200, 300 and 400  $^\circ\text{C}$ , respectively. The results confirmed that increasing the heat treatment temperature leads to an increase in particle size after acid leaching.

### 3.3.3. Characterization of Catalysts Using Cyclic Voltammetry and Carbon Monoxide Stripping Voltammetry

Cyclic voltammetry (CV) was used to characterize the surface of the catalyst (Figure 34A) after different heat treatments. After initial conditioning by cycling at low potential range ( $E \leq 1.0 V_{\text{RHE}}$ ) in argon-saturated 0.1 M HClO<sub>4</sub>, cyclic voltammetry was performed. The current ( $\text{mA}/\text{cm}_{\text{geo}}^{-2}$ ) was normalized using the geometric surface area of electrode. The catalysts treated at different temperatures exhibited similar distinctive H-adsorption and H-desorption features associated with hydrogen underpotential deposition ( $H_{\text{upd}}$ ) on metallic species since hydrogen is not easy to adsorb on oxide surface<sup>126</sup> which supports the formation of metallic Ir-rich surface after chemical leaching.<sup>105</sup> The oxidation-reduction peaks observed at  $\sim 0.5 V_{\text{RHE}}$  corresponds to the redox reaction of surface oxides on iridium.<sup>105</sup> The charge transferred during the hydrogen underpotential deposition is proportional to the number of iridium active sites and can be used to calculate electrochemical surface area.<sup>127</sup> Therefore, the smaller peak areas in CVs of the catalysts at higher temperatures suggest that the electrochemical surface area of the catalysts decreased as the treatment temperature increased.

Carbon monoxide (CO) stripping voltammetry measurements (Figure 34B) also confirmed the presence of metallic Ir surface. CoIr300-CL exhibited the lowest onset potential of CO stripping which may be attributed to weaker CO binding on the surface of the catalyst caused by the modified electronic properties as supported by density functional theory calculations.<sup>128</sup> The electrochemical surface area of Ir ( $\text{ECSA}_{\text{Ir,CO}}$ ) was determined by the integration of the CO stripping peak. The calculated  $\text{ECSA}_{\text{Ir,CO}}$  was 80.9,  $61.2 \pm 3.1$  and  $50.6 \text{ m}^2 \text{ g}^{-1}$  for CoIr200-CL, CoIr300-CL and CoIr400-CL,

respectively. The result implies that the ECSA of the catalyst was reduced with heat treatment temperature which may come from the growth of iridium particles with heat treatment temperature.<sup>73</sup> The smaller particle size of CoIr200-CL was confirmed by XRD analysis. The ECSA of catalysts is a reasonably high value compared with IrO<sub>2</sub> of 25.3 ± 1.5 m<sup>2</sup>g<sup>-1</sup> from Alfa Aesar.<sup>57, 71</sup>

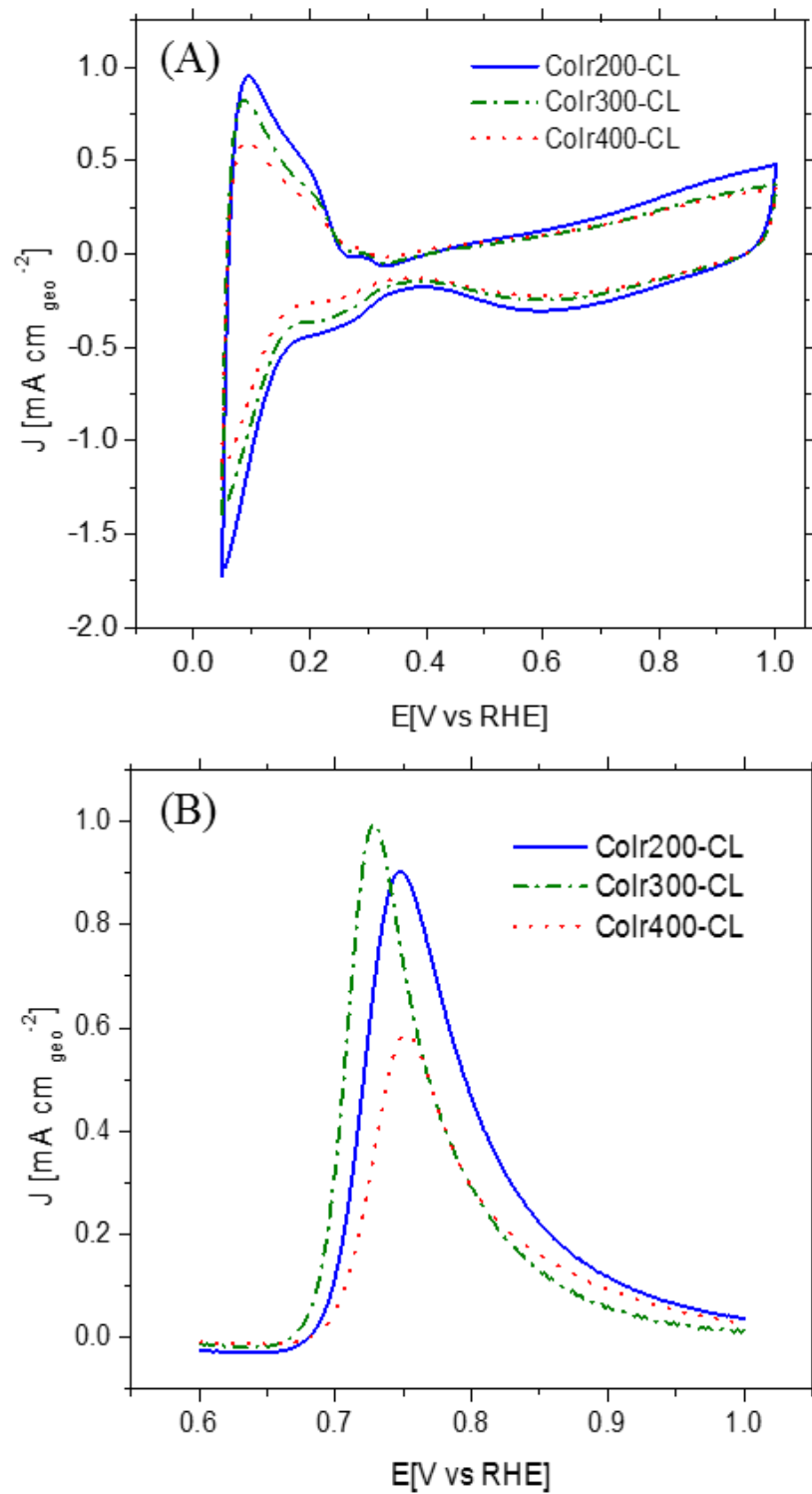


**Figure 34.** Initial cyclic voltammograms (CVs) of CoIr200-CL, CoIr300-CL and CoIr400-CL (A); CO Stripping of CoIr200-CL, CoIr300-CL, CoIr400-CL (B).

After an “electrochemical oxidation” step<sup>57</sup> comprising 60 scans between 0.05-1.5  $V_{RHE}$ , CV was carried out and the catalysts were labeled with the suffix “EO” as CoIr200-CL<sub>EO</sub>, CoIr300-CL<sub>EO</sub> and CoIr400-CL<sub>EO</sub> (Figure 35). After electrochemical oxidation, the peaks due to H<sub>upd</sub> features were eliminated. The anodic peak centered at  $\sim 0.27 V_{RHE}$  and  $\sim 0.82 V_{RHE}$  were attributed to the transition from Ir<sup>3+</sup> to Ir<sup>4+</sup> species.<sup>108, 129, 130</sup> The comparison of the CVs of CoIr200-CL<sub>EO</sub>, CoIr300-CL<sub>EO</sub> and CoIr400-CL<sub>EO</sub> shows the anodic peak at  $\sim 0.27 V_{RHE}$  appears at different potentials which suggests a different local chemical environment and electron density distribution exist for the hydrated Ir<sup>3+</sup>-OH species at the surface of the catalysts. In addition, the peak at  $\sim 0.27 V_{RHE}$  is significantly lower than the peak position within IrO<sub>2</sub> at  $\sim 0.38 V_{RHE}$  which suggests a different surface structure for the CoIr catalysts.

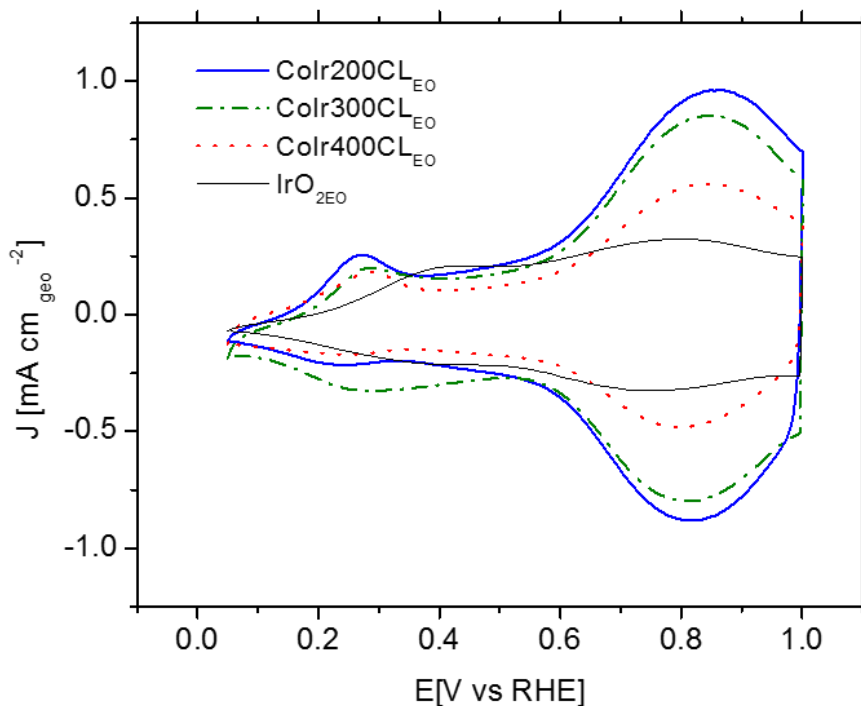


**Figure 35.** Cyclic voltammetry (CV) scans of CoIr200-CL<sub>EO</sub>, CoIr300-CL<sub>EO</sub>, CoIr400-CL<sub>EO</sub> and commercial IrO<sub>2,EO</sub>.

### 3.3.4. Evaluation Electrochemical Oxygen Evolution Activity of Cobalt-iridium nanoframes Catalysts

Pseudocapacitance measurements<sup>85, 93</sup> (Figure 36) were used to determine the effect of temperature on the ECSA of iridium oxide of catalysts. The ECSA<sub>IrO<sub>2</sub></sub> value of CoIr200-CL<sub>EO</sub> calculated from pseudocapacitance measurements was 31.0 m<sup>2</sup> g<sup>-1</sup> which is higher than the other two catalysts treated at 200 and 400 °C as shown in Table 9 at the end of this section.

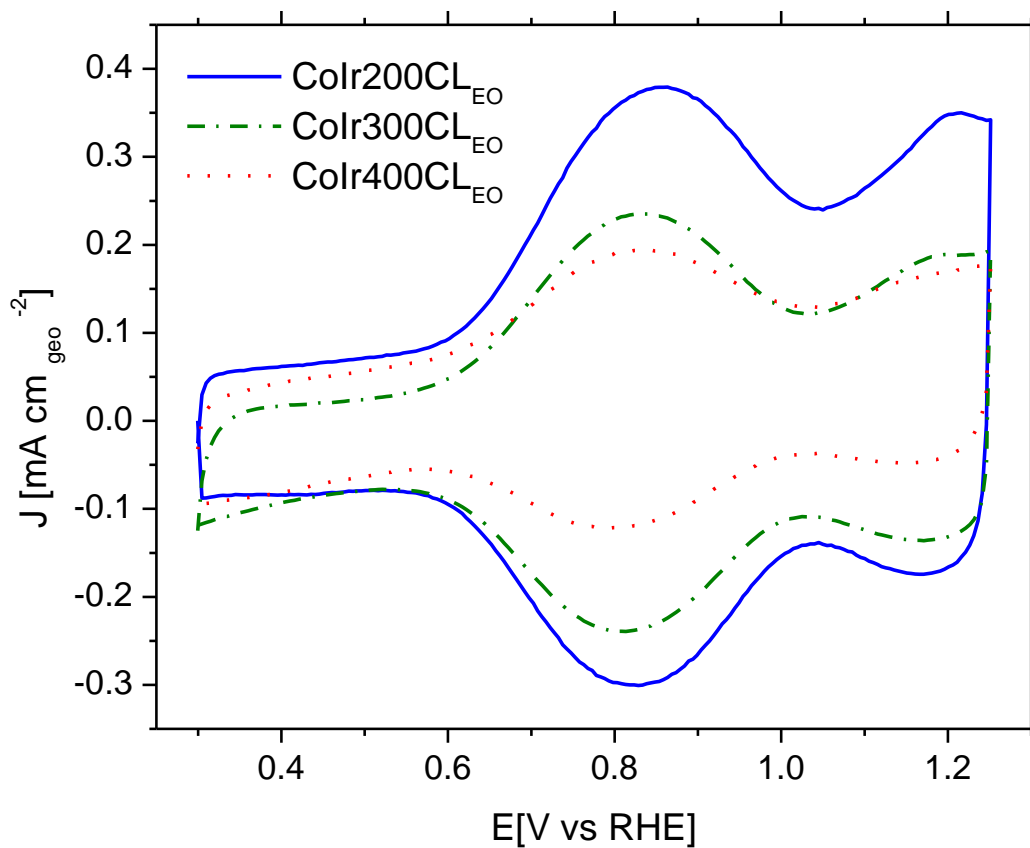


**Figure 36.** Cyclic voltammetric (CV) scans after Au-disk background correction of CoIr200-CL<sub>EO</sub>, CoIr300-CL<sub>EO</sub> and CoIr400-CL<sub>EO</sub> used to determine pseudocapacitive charge. CVs obtained in Ar-saturated 0.1 M HClO<sub>4</sub> using a scan rate of 50 mV s<sup>-1</sup>. Pseudocapacitive charge was determined using the oxidation scan.

Chronoamperometry was used to determine the OER current to minimize the

current from electrochemical double layer capacitance.<sup>57</sup> Figure 37 shows the chronoamperometric polarization curves of CoIr200-CL<sub>EO</sub>, CoIr300-CL<sub>EO</sub>, CoIr400-CL<sub>EO</sub> and commercial IrO<sub>2,EO</sub> normalized versus the mass of Ir obtaining from SEM/EDS (CoIr200-CL<sub>EO</sub> and CoIr300-CL<sub>EO</sub>) or ICP-MS (CoIr300-CL<sub>EO</sub>). The polarization curves for the thermal treated catalysts at 200 and 400 °C had comparable currents, but the catalyst treated at 300°C had the highest current and mass activity. It is clear that the CoIr-based catalysts had higher currents and moved the onset potential of OER toward lower potentials compared to commercial IrO<sub>2,EO</sub>.

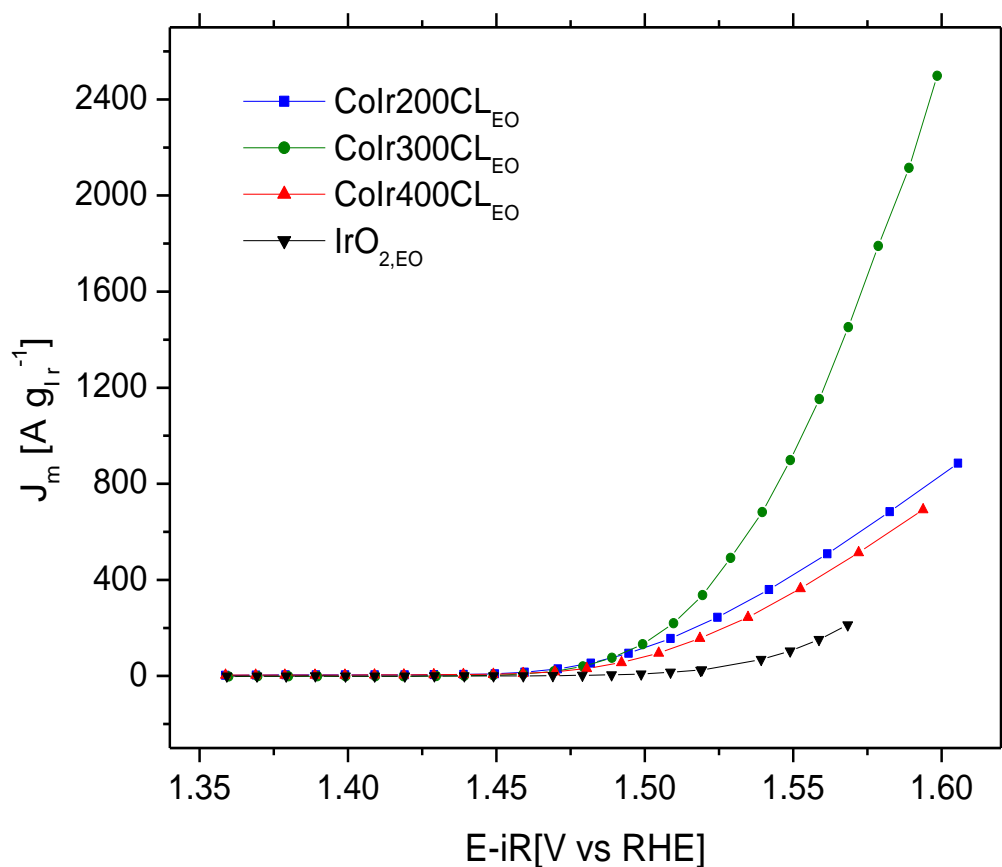


**Figure 37.** Current in the oxygen evolution reaction (OER) voltage region determined from chronoamperometry measurements of CoIr200-CL<sub>EO</sub>, CoIr300-CL<sub>EO</sub>, CoIr400-CL<sub>EO</sub> and commercial IrO<sub>2</sub> after electrochemical oxidation in O<sub>2</sub>-free 0.1 M HClO<sub>4</sub>.

The Tafel slopes within potential range 1.48 to 1.52 V<sub>RHE</sub> of CoIr200-CL<sub>EO</sub>, CoIr300-CL<sub>EO</sub>, CoIr400-CL<sub>EO</sub> and commercial IrO<sub>2,EO</sub> (Figure 6B) were determined to provide information regarding the reaction mechanism.<sup>131, 132</sup> The calculated Tafel slopes are provided in Table 7. The Tafel slope was revealed to be dependent of thermal treatment temperature. The lowest Tafel slope was  $45 \pm 4$  mV dec<sup>-1</sup> for the 300 °C treated catalyst which is close to the Tafel slope of IrO<sub>2,EO</sub> ( $37 \pm 3$  mV dec<sup>-1</sup>) which indicates similar reaction mechanisms occur at the catalysts' surface. The value of the Tafel slope which is close to 40 mV dec<sup>-1</sup> is consistent with the second electron transfer step as the rate determining step predicted by OER mechanistic steps notated as either the “electrochemical oxide path” or the DFT-predicted peroxide path.<sup>21, 114, 131</sup> The Tafel slope was increased to 58 mV dec<sup>-1</sup> and 51 mV dec<sup>-1</sup> for CoIr200-CL<sub>EO</sub> and CoIr400-CL<sub>EO</sub>, respectively. The Tafel slope of CoIr400-CL<sub>EO</sub> was similar to IrO<sub>2</sub>-Ta<sub>2</sub>O<sub>5</sub> mixed oxide (60 mV dec<sup>-1</sup>).<sup>133</sup> The Tafel slope of CoIr200-CL<sub>EO</sub> was comparable with previously reported carbon supported IrCoNi porous hollow nanocrystals (53.8 mV dec<sup>-1</sup>)<sup>134</sup> which suggests the CoIr200-CL<sub>EO</sub> has similar reaction mechanism as previous reported IrCoNi catalyst.

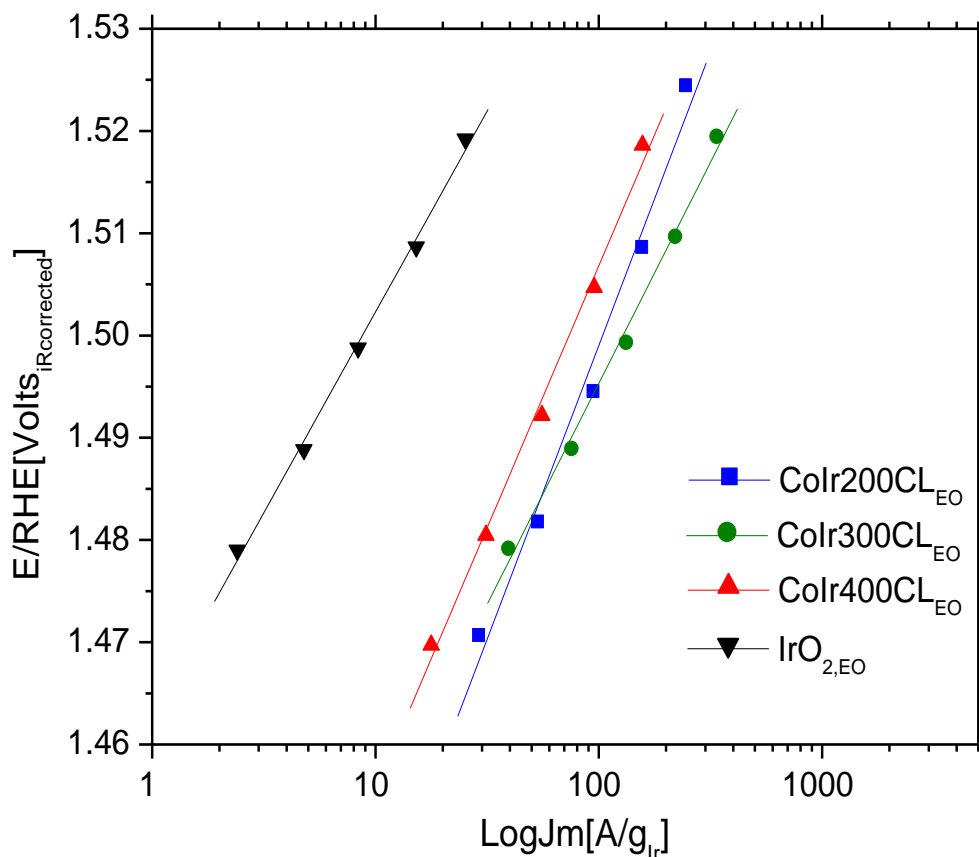


**Figure 38.** Tafel slopes determined by chronoamperometry. The potential (iR-corrected) was set between 1.47 V<sub>RHE</sub> to 1.52 V<sub>RHE</sub> to reduce the mass transport contribution.

The OER specific activity was determined by normalizing the current at 1.51 V<sub>RHE</sub> to the electrochemical surface area obtained from pseudocapacitance. As shown in Figure 39(B), the OER specific activities at 1.51 V<sub>RHE</sub> was  $1.05 \pm 0.15 \text{ A cm}_{\text{IrO}_2}^{-2}$  for CoIr300-CL<sub>EO</sub> which has the highest activity among the four catalysts. The OER specific activity of CoIr300-CL<sub>EO</sub> is 17 times higher in comparison to commercial IrO<sub>2</sub>. CoIr300-CL<sub>EO</sub> also showed 3 and 2 times ( $0.33 \text{ A cm}_{\text{IrO}_2}^{-2}$  for CoIr200-CL<sub>EO</sub> and  $0.53 \text{ A cm}_{\text{IrO}_2}^{-2}$  for CoIr400-CL<sub>EO</sub>) higher OER specific activity compared to the catalysts heated at 200 and 400 °C, respectively. The significantly higher OER specific activity of CoIr300-CL<sub>EO</sub> compared with the catalysts treated at 200 and 400 °C and commercial IrO<sub>2</sub>- may

be attributed to the presence of a high density and the distinct structure of Ir-OH surface species and/or enhanced interaction of Ir with Co within the structure.<sup>116</sup> As shown in XRD analysis (Figure 33), the catalysts treated at different temperature have different particle sizes and lattice constants which may contribute to the differences between the specific activities of the CoIr catalysts.<sup>67</sup>

To compare the mass activities, the current at 1.51 V<sub>RHE</sub> of CoIr200-CL<sub>EO</sub>, CoIr300-CL<sub>EO</sub>, CoIr400-CL<sub>EO</sub> and commercial IrO<sub>2,EO</sub> were compared (Figure 39A). The current was determined from chronoamperometry and normalized for the Ir mass determined by SEM/EDS. As presented in Figure 39(A), the catalyst treated at 300 °C showed a significantly higher mass activity ( $211 \pm 24 \text{ A g}_{\text{Ir}}^{-1}$ ) compared to the other catalysts which is approximately 2 times higher than the catalysts treated at 200 and 400°C of  $121 \text{ A g}_{\text{Ir}}^{-1}$  and  $120 \text{ A g}_{\text{Ir}}^{-1}$ , respectively. All the CoIr-based catalysts exhibited higher mass activities than that of IrO<sub>2</sub> ( $14.6 \pm 2.5 \text{ A g}_{\text{Ir}}^{-1}$ ). The high mass activity of CoIr300-CL<sub>EO</sub> mostly due to its high specific activity as discussed above. Furthermore, the porous nanostructure shown in SEM images and high ECSA of CoIr-based catalysts may provide improved mass transport and access to the active site compared with commercial IrO<sub>2,EO</sub> which is favorable for the oxygen evolution reaction.<sup>67</sup>

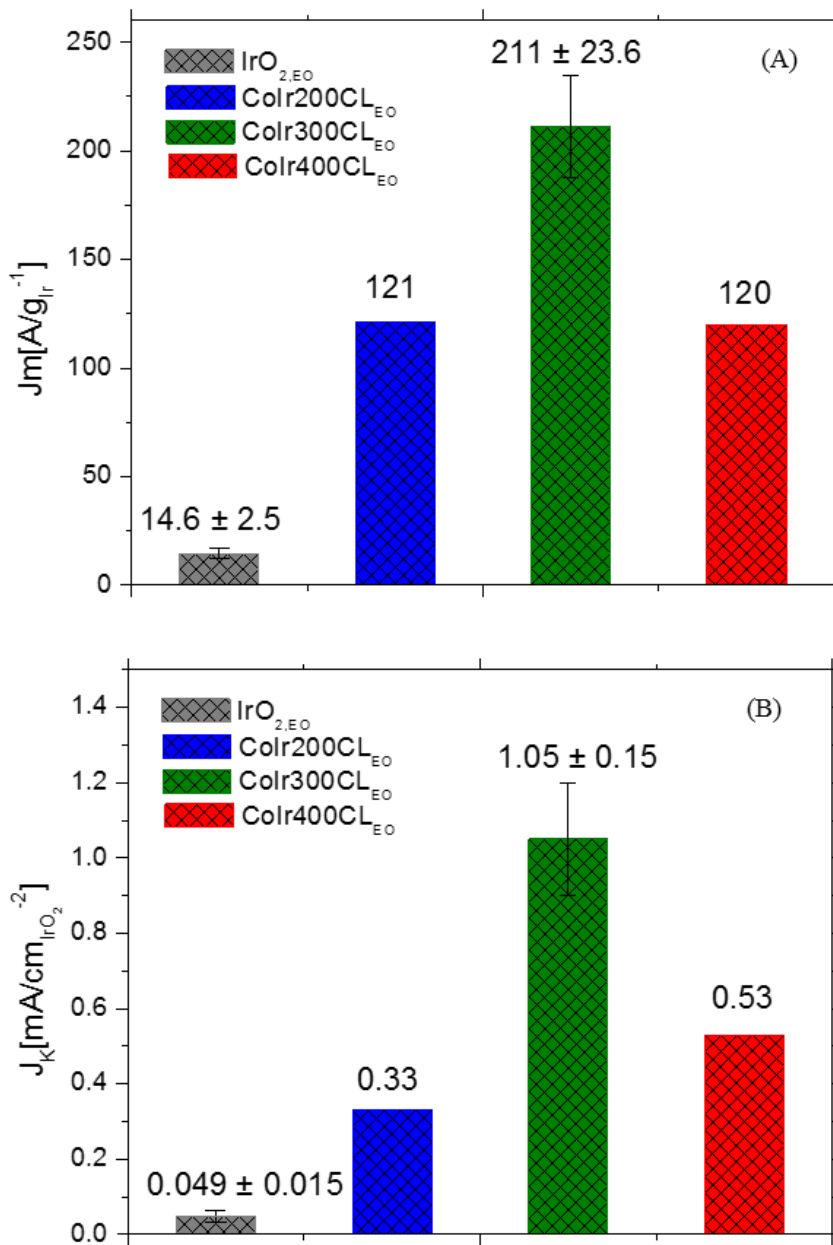


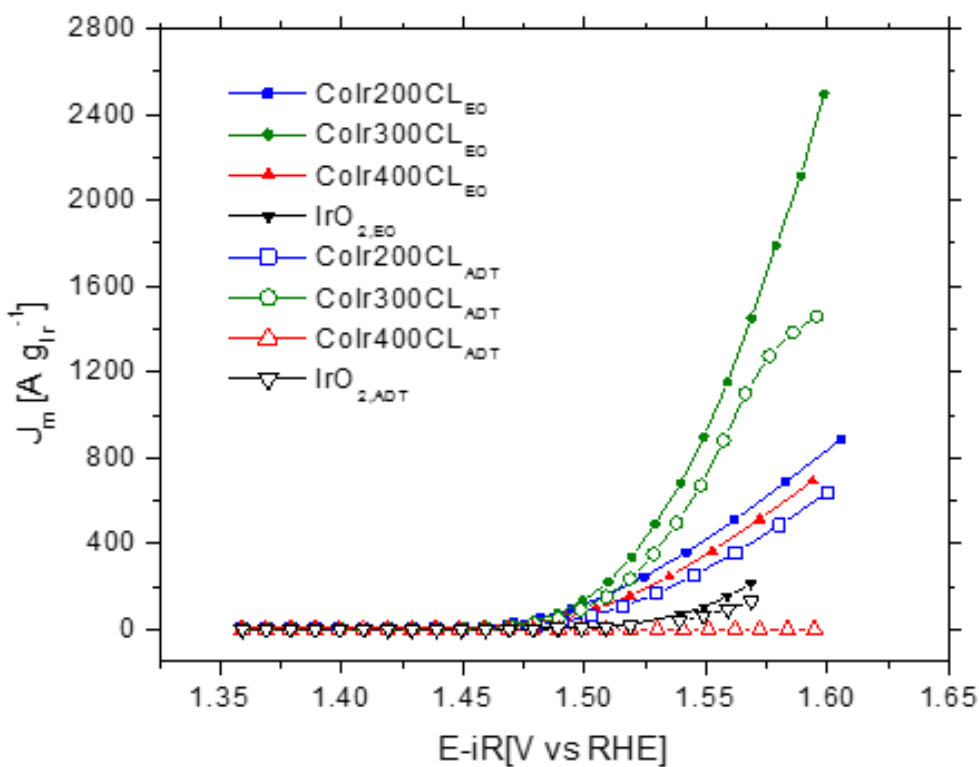
**Figure 39.** Comparison of OER mass activities treated with different temperatures at 1.51 V<sub>RHE</sub> (A); comparison of OER specific activities treated with different temperatures at 1.51 V<sub>RHE</sub> (B).

### 3.3.5. Evaluation Electrochemical Oxygen Evolution Stability of Cobalt-iridium nanoframes Catalysts

After an accelerated durability testing (ADT) protocol, the OER current was

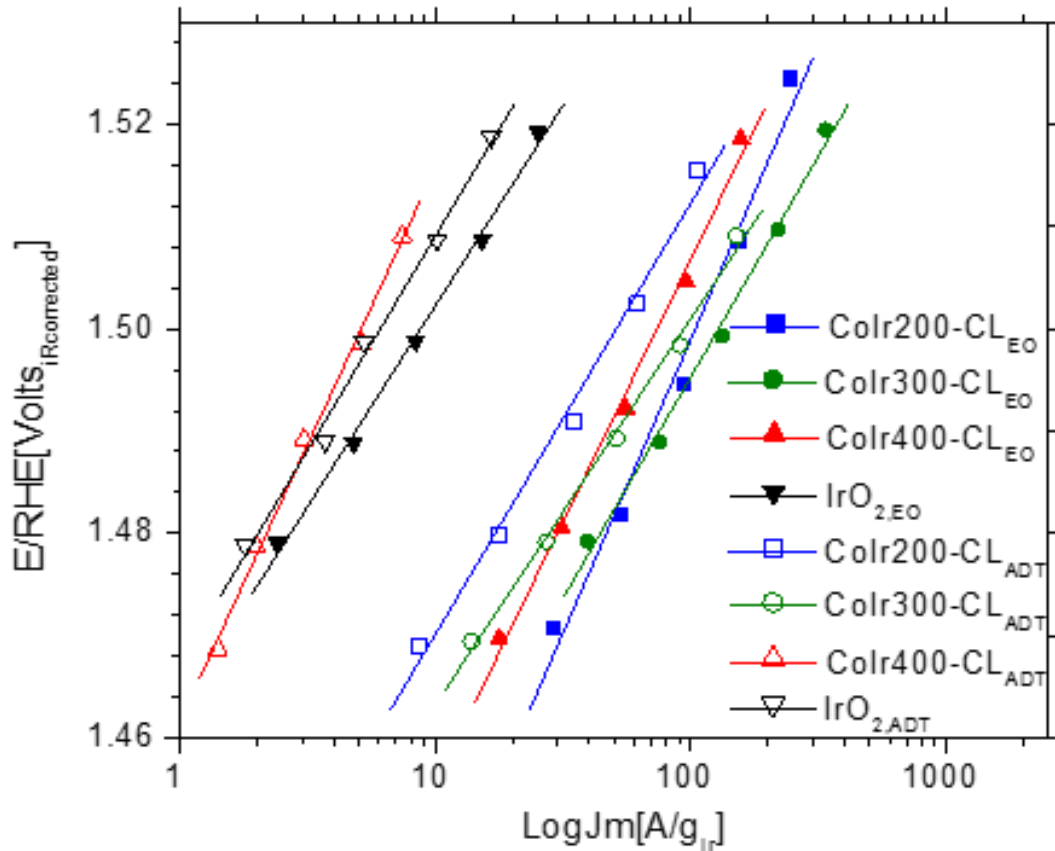
measured to evaluate the stability of the catalysts. The ADT protocol consisted of applying a constant potential of 1.6 V for 13.5 hours which has been previously reported.<sup>60, 110</sup> To eliminate the O<sub>2</sub> bubbles accumulation during the constant potential step,<sup>90</sup> the electrolyte was replaced and purged with argon for 30 minutes to remove bubbles. The catalysts after ADT procedure were labeled as CoIr200-CL<sub>ADT</sub>, CoIr300-CL<sub>ADT</sub> and CoIr400-CL<sub>ADT</sub>.

Figure 40 shows the chronoamperometric polarization curves of CoIr200-CL<sub>ADT</sub>, CoIr300-CL<sub>ADT</sub>, CoIr400-CL<sub>ADT</sub> and commercial IrO<sub>2,ADT</sub>. The CoIr-based catalysts and IrO<sub>2,EO</sub> all showed lower currents after the ADT protocol.



**Figure 40.** Current in the oxygen evolution reaction (OER) voltage region determined from chronoamperometry measurements of CoIr200-CL<sub>EO</sub>, CoIr300-CL<sub>EO</sub>, CoIr400-CL<sub>EO</sub> and commercial IrO<sub>2</sub> before and accelerated durability testing in O<sub>2</sub>-free 0.1 M HClO<sub>4</sub>. The stability was carried out using a potentiostatic procedure by holding the working electrode at 1.6 V<sub>RHE</sub>-iR-corrected for 13.5 hours under rotation at 2500 rpm.

As shown in Figure 41 and Table 7, the Tafel slopes of CoIr300-CL<sub>EO</sub> decreased slightly from 43 to 38 after the durability testing supporting that the reaction mechanism remained similar. The Tafel slope of CoIr200-CL<sub>EO</sub> decreased from 58 to 42 mV dec<sup>-1</sup>, indicating CoIr200-CL<sub>ADT</sub> had a similar Tafel slope compared with CoIr300-CL<sub>EO</sub> which suggests the same reaction mechanistic pathway. The Tafel slope of CoIr400-CL<sub>EO</sub> increased slightly from 51 to 54 mV dec<sup>-1</sup> suggesting that the reaction mechanism was unchanged.<sup>73</sup>



**Figure 41.** Tafel slopes before and after accelerated durability testing determined by chronoamperometry. The potential (iR-corrected) was set between 1.47 V<sub>RHE</sub> to 1.52 V<sub>RHE</sub> to reduce the mass transport contribution.

**Table 7.** Comparison of Tafel slopes of CoIr200-CL, CoIr300-CL and CoIr400-CL after electrochemical oxidation (EO) and after accelerated durability testing (ADT).

Material	Tafel slopes (mV Dec <sup>-1</sup> )	
	After electrochemical oxidation (EO)	After accelerated durability testing (ADT)
CoIr200-CL	58	42
CoIr300-CL	43	38
CoIr400-CL	51	54

The calculated OER specific activity of the catalysts after EO and ADT are shown in Figure 42(B). The specific activity of IrO<sub>2,ADT</sub> decreased from 0.049 to 0.042 mA cm<sup>-2</sup><sub>IrO<sub>2</sub></sub>, while 86% of activity remained after ADT. In contrast with IrO<sub>2</sub>, the OER specific activity of CoIr200-CL<sub>ADT</sub> and CoIr300-CL<sub>ADT</sub> increased while the ECSA<sub>IrO<sub>2</sub></sub> of CoIr200-CL<sub>ADT</sub> and CoIr300-CL<sub>ADT</sub> decreased compared with the catalysts before ADT. The increase in specific activity indicates that the activity of the active sites was increased which may come from redistribution of Co and Ir during the operation, leading to modification of electron density distribution around the active sites. Additionally, the increase of hydroxide/oxide species ratio after ADT shown in Figure 44 may contribute to improving the specific activity.<sup>11</sup> The large drop of the specific activity of CoIr400-CL<sub>ADT</sub> may be related to the higher Co and O ratio (Ir:Co:O–1:0.4:2) relative to Ir compared to the catalysts treated at lower temperature as shown in SEM/EDS(Figure 32). Cobalt is very unstable in a corrosive and high potential environment. Ir particles connected to Co may detach together under extreme conditions, such as start-up/shut-down procedures.<sup>11</sup> Particle coalescence may also contribute to the low specific activity of CoIr400-CL<sub>ADT</sub>.<sup>135</sup>

As shown in Figure 42(A), the OER mass activity of the commercial  $\text{IrO}_{2, \text{EO}}$  catalyst declined with a  $71 \pm 7 \%$  retention of the initial mass activity from  $14.6$  to  $10.3 \text{ A g}_{\text{Ir}}^{-1}$  after ADT. The OER mass activity of the  $\text{CoIr300-CL}_{\text{EO}}$  and commercial  $\text{IrO}_2$  showed a similar retention  $70 \pm 8 \%$  decreased from  $211$  to  $147 \text{ A g}_{\text{Ir}}^{-1}$ . The catalysts treated at  $200$  and  $400^\circ\text{C}$  showed a lower retention of OER mass activity of  $39\%$  and  $8\%$ , respectively. Consequently, the mass activity of  $\text{CoIr300-CL}_{\text{ADT}}$  was  $3$  and  $40$  times higher in comparison to  $\text{CoIr200-CL}_{\text{ADT}}$  and  $\text{CoIr400-CL}_{\text{ADT}}$ , respectively. Even though the specific activity of  $\text{CoIr200-CL}_{\text{ADT}}$  and  $\text{CoIr300-CL}_{\text{ADT}}$  were increased, the decrease of  $\text{ECSA}_{\text{IrO}_2}$  for the catalysts resulted in lowering of the mass activity. The particle agglomeration provided a poor mass transport on the catalyst surface was considered to be a main factor of mass activity loss of CoIr catalysts.<sup>113</sup> In this study,  $\text{CoIr300-CL}_{\text{EO}}$  exhibited high activity and comparable stability relative to commercial  $\text{IrO}_{2, \text{EO}}$ . This observation suggests that there is not necessarily a tradeoff between activity and stability, which is different from a prior study.<sup>120</sup> Another study suggested that it was possible that higher activity and stability can be achieved simultaneously.<sup>57</sup>

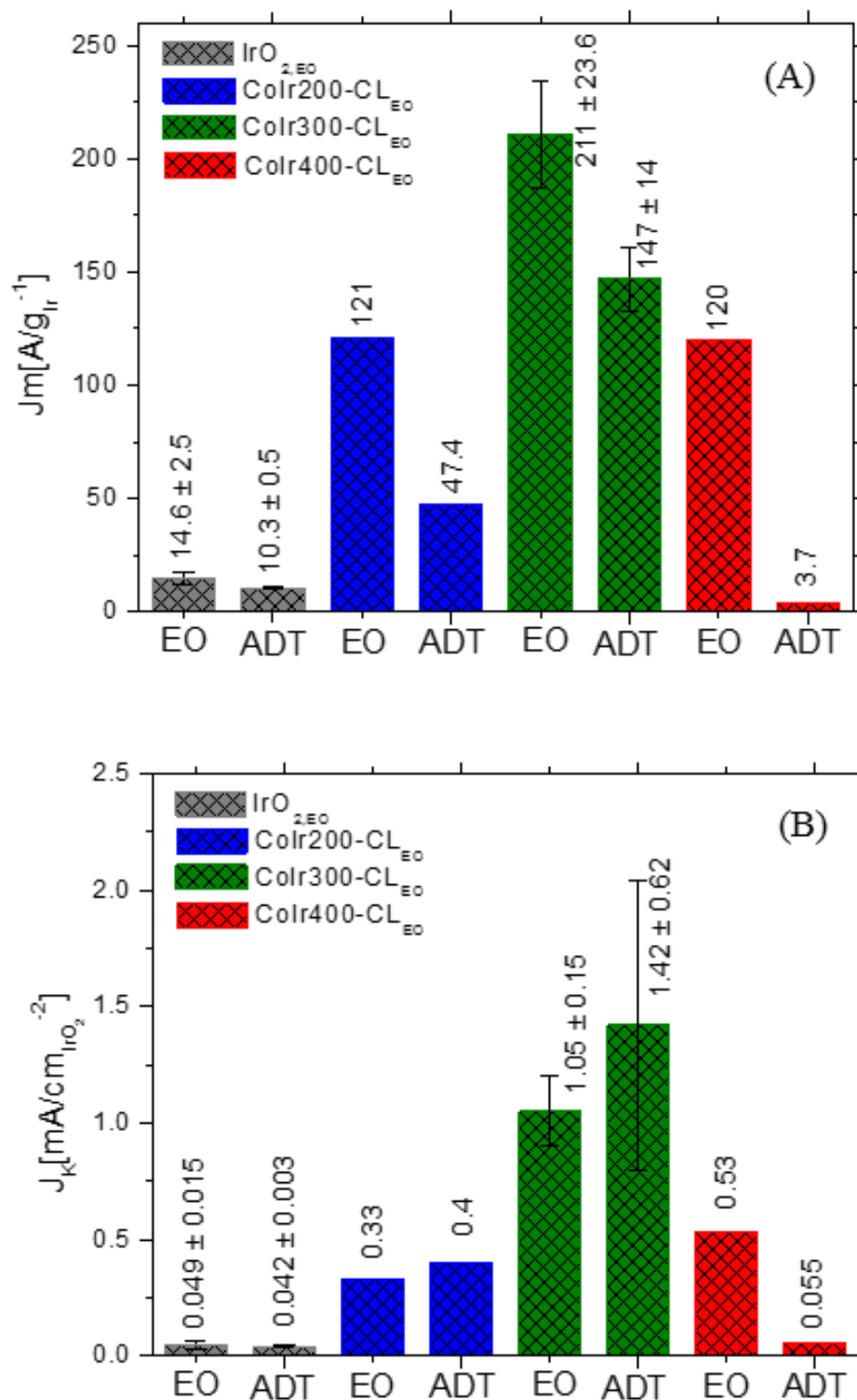


**Figure 42.** Comparison of OER mass activities at 1.51 V<sub>RHE</sub> before and after accelerated durability testing (A); comparison of OER specific activities at 1.51 V<sub>RHE</sub> before and after accelerated durability testing (B).

To understand the degradation of the catalyst, the  $\text{ECSA}_{\text{IrO}_2}$  value of CoIr200- $\text{CL}_{\text{ADT}}$ , CoIr300- $\text{CL}_{\text{ADT}}$  and CoIr400- $\text{CL}_{\text{ADT}}$  were calculated from pseudocapacitance measurements (Figure 43). The calculated values are shown in Table 9. After ADT, the  $\text{ECSA}_{\text{IrO}_2}$  declined with a 30%, 62% and 29% remaining for the 200, 300 and 400 °C heat treated catalysts, respectively. The large reduction of  $\text{ECSA}_{\text{IrO}_2}$  of CoIr200- $\text{CL}_{\text{ADT}}$  may result from the weak interaction between Ir and Co provided by low temperature treatment.<sup>57</sup> Thus, the extent of particle detachment or Ir dissolution during operation may be large. Previous studies suggested that a higher temperature treatment may increase the interaction between Co and Ir, leading to an enhanced stability;<sup>11, 57</sup> however, this does not agree with the CV measurement of CoIr400- $\text{CL}_{\text{ADT}}$ . The dramatic decline of  $\text{ECSA}_{\text{IrO}_2}$  of CoIr400- $\text{CL}_{\text{ADT}}$  can be explained by Ir dissolution, particle detachment, and particle coalescence.<sup>135</sup> More characterization is needed to confirm the factors contributing to CoIr400- $\text{CL}_{\text{ADT}}$  instability.

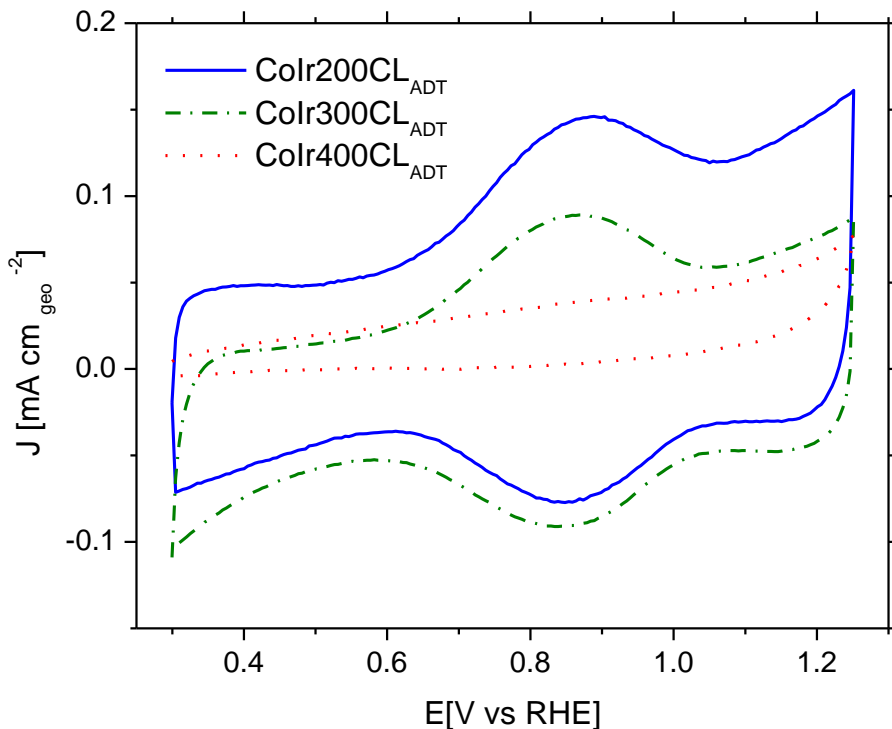


**Figure 43.** Cyclic voltammetric (CV) scans after Au-disk background correction of CoIr200-CL<sub>ADT</sub>, CoIr300-CL<sub>ADT</sub>, CoIr400-CL<sub>ADT</sub> used to determine pseudocapacitive charge. CVs obtained in Ar-saturated 0.1 M HClO<sub>4</sub> using a scan rate of 50 mV s<sup>-1</sup>. Pseudocapacitive charge was determined using the oxidation scan.

The CVs of the CoIr based catalysts after ADT are compared and shown in Figure 44. Both CoIr200-CL<sub>ADT</sub> and CoIr300-CL<sub>ADT</sub> showed a similar profile attributed to the formation of hydroxide/oxide species as before ADT, but the coulombic charge decreased after ADT, which is associated with the loss of active surface electrochemical surface area. In addition, the peak area of the anodic peak centered at  $\sim 0.27$  V<sub>RHE</sub> in CoIr200-CL<sub>ADT</sub> and CoIr300-CL<sub>ADT</sub>, which is attributed to the formation of hydrated Ir<sup>3+</sup>-OH species<sup>105, 116</sup> decreased and shifted to a higher potential compared with the catalysts before ADT. The peak area of the peak at  $\sim 0.82$  V<sub>RHE</sub>, which is attributed to the transition from Ir<sup>3+</sup> to Ir<sup>4+</sup> species<sup>129, 130</sup> also decreased. The ratio between the two peaks also

decreased in comparison to the catalysts before ADT. The decreased hydrated  $\text{Ir}^{3+}\text{-OH}$  species fraction may be connected to the lowering of the activity.<sup>11</sup> The CV of CoIr400- $\text{CL}_{\text{ADT}}$  showed the current decreased dramatically, indicating loss of most of the active site on the surface of catalyst. The change of CVs profiles suggests a different local chemical environment and electron density distribution exist at the surface of the CoIr based catalysts before and after ADT.

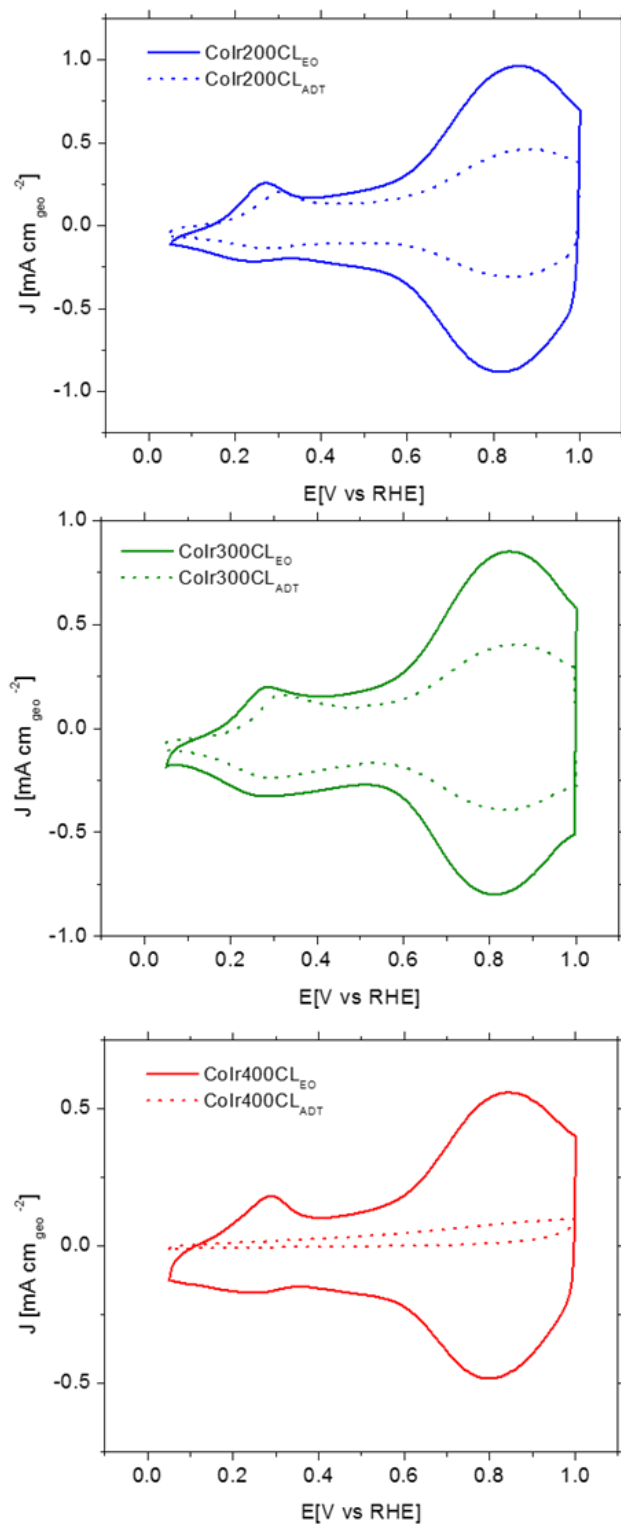


**Figure 44.** Comparison of cyclic voltammetry (CV) scans of CoIr200-CL<sub>EO</sub> and CoIr200-CL<sub>ADT</sub> (A); CoIr300-CL<sub>EO</sub> and CoIr300-CL<sub>ADT</sub> (B); CoIr400-CL<sub>EO</sub> and CoIr400-CL<sub>ADT</sub> (C).

**Table 8.** Inductively Coupled Plasma Mass Spectrometry (ICP-MS) analysis of iridium from CoIr200-CL, CoIr300-CL and CoIr400-CL in electrolytes after electrochemical oxidation (EO) and after accelerated durability testing (ADT).

Material	After electrochemical oxidation (EO)		After accelerated durability testing (ADT)	
	Ir wt. % Lost	Ir Degradation rate [pg/s]	Ir wt. % Lost	Ir Degradation rate [pg/s]
CoIr200-CL	12.8	126	42.7	29.5
CoIr300-CL	10.4 ± 0.3	105 ± 18	20.7 ± 4.9	15 ± 6
CoIr400-CL	9.5	91.6	47.3	31.9

The analysis of the percent of iridium dissolved into the electrolyte and its corresponding iridium degradation rate were calculated and are summarized in Table 8. ICP-MS measurements showed that CoIr300-CL catalyst had the lowest Ir lost (20.7 wt %) within the electrolyte after ADT compared with the catalysts treated at 200 and 400°C of 42.7 wt % and 47.3 wt %, respectively. This may explain why CoIr300-CL maintains most of the activity after ADT compared with CoIr200-CL and CoIr400-CL. The Ir lost and the dissolution rate of Ir decreased as the temperature increased after EO which can be explained by enhanced interaction between Co and Ir under higher temperature treatment. A previous study of Ni-IrO<sub>2</sub> reported higher Ir dissolution for Ni-IrO<sub>2</sub> compare with IrO<sub>2</sub>.<sup>57</sup> It is possible that interreact with Co may increase Ir dissolution.

**Table 9.** Comparison of electrochemical surface areas (ECSA), oxygen evolution reaction (OER) mass activities, and OER specific activities of IrO<sub>2</sub>-AA (Alfa Aesar), CoIr200-CL<sub>EO</sub>, CoIr300-CL<sub>EO</sub> and CoIr400-CL<sub>EO</sub>. The OER mass activities were normalized for the mass of Ir and were determined at 1.51 V<sub>RHE</sub> and 1.55 V<sub>RHE</sub> from chronoamperometry measurements. Data obtained before and after accelerated durability testing (ADT) is included. Percent of initial and final OER mass activities were determined by the ratios of the mass activities at 1.51 V<sub>RHE</sub> before and after ADT.

Value	Parameter (units)	IrO <sub>2</sub> -AA <sup>57</sup>	CoIr200CL	CoIr300CL	CoIr400CL
<b>Electrode loading</b>	Loading ( $\mu\text{g}_{\text{Ir}} \text{cm}^{-2}_{\text{geo}}$ )	11.6	17.1	18.5	16.7
<b>Electrochemical surface area of iridium (ECSA<sub>Ir</sub>)</b>	ECSA <sub>Ir,CO</sub> ( $\text{m}^2 \text{g}^{-1}$ )	–	80.9	61.2 ± 3.12	50.6
<b>Electrochemical surface area of IrO<sub>2</sub> (ECSA<sub>IrO2</sub>), after EO</b>	ECSA <sub>IrO2</sub> ( $\text{m}^2 \text{g}^{-1}$ )	25.3 ± 1.5	31.0	20.1 ± 2.49	19.3
<b>Initial OER activity</b>	J <sub>geo</sub> <sup>1.51V</sup> ( $\text{mA cm}^{-2}_{\text{geo}}$ )	0.17 ± 0.03	2.07	3.79 ± 0.66	2.02
	J <sub>m</sub> <sup>1.51V</sup> ( $\text{A g}_{\text{Ir}}^{-1}$ )	14.6 ± 2.5	121	211 ± 23.6	120
	J <sub>s</sub> <sup>1.51V</sup> ( $\text{mA cm}^{-2}_{\text{IrO2}}$ )	0.049 ± 0.015	0.332	1.05 ± 0.15	0.53
	J <sub>geo</sub> <sup>1.55V</sup> ( $\text{mA cm}^{-2}_{\text{geo}}$ )	1.04 ± 0.3	5.76	16.6 ± 0.73	5.66
	J <sub>m</sub> <sup>1.55V</sup> ( $\text{A g}_{\text{Ir}}^{-1}$ )	89.9 ± 26.7	337	823 ± 62.9	337
	J <sub>s</sub> <sup>1.55V</sup> ( $\text{mA cm}^{-2}_{\text{IrO2}}$ )	0.31 ± 0.10	0.92	4.16 ± 0.72	1.49
<b>Electrochemical surface area of IrO<sub>2</sub> (ECSA<sub>IrO2</sub>), after ADT</b>	ECSA <sub>IrO2</sub> ( $\text{m}^2 \text{g}^{-1}$ )	25.3 ± 1.5	9.96	12.0 ± 3.1	5.6
<b>Final OER activity, After ADT (1.6 V)</b>	J <sub>geo</sub> <sup>1.51V</sup> ( $\text{mA cm}^{-2}_{\text{geo}}$ )	0.12 ± 0.009	0.81	2.57 ± 0.39	0.06
	J <sub>m</sub> <sup>1.51V</sup> ( $\text{A g}_{\text{Ir}}^{-1}$ )	10.3 ± 0.8	47.4	147 ± 14	3.65
	J <sub>s</sub> <sup>1.51V</sup> ( $\text{mA cm}^{-2}_{\text{IrO2}}$ )	0.042 ± 0.003	0.40	1.42 ± 0.62	0.055
	J <sub>geo</sub> <sup>1.55V</sup> ( $\text{mA cm}^{-2}_{\text{geo}}$ )	0.68 ± 0.1	2.99	12.5 ± 2.0	0.43
	J <sub>m</sub> <sup>1.55V</sup> ( $\text{A g}_{\text{Ir}}^{-1}$ )	59.8 ± 10	175	700 ± 93.3	25.8
	J <sub>s</sub> <sup>1.55V</sup> ( $\text{mA cm}^{-2}_{\text{IrO2}}$ )	0.26 ± 0.03	1.50	6.84 ± 3.23	0.39
<b>Percent OER mass activity (Final/Initial)</b>	ADT J <sub>m</sub> <sup>1.51V</sup> / Initial J <sub>m</sub> <sup>1.51V</sup> (%)	71 ± 7	39	70 ± 8	3
	ADT J <sub>m</sub> <sup>1.55V</sup> / Initial J <sub>m</sub> <sup>1.55V</sup> (%)	68 ± 9	52	84 ± 5	8

## IV. CONCLUSIONS

This study demonstrates the ability to make an integrated cobalt-iridium metal alloy nanostructure that can be chemically leached and then electrochemically conditioned to form an oxygen evolution catalyst with very high activity and acceptable stability. Oxygen evolution activity measurements showed that CoIr300-CL exhibited 17 times higher OER mass activity and 16 times higher OER specific activity compared with commercial IrO<sub>2</sub>. The higher OER activities are attributed to the interaction of Ir with Co within the hydrous cobalt-iridium oxide surface that tunes the surface atomic and electronic structure. CV measurements show the presence of an anodic iridium hydroxide peak at lower potential compared with IrO<sub>2</sub> which supports the hypothesis that cobalt-iridium oxide nanoframes have highly active Ir-OH surface species that may contribute to the high OER activity. In addition to higher activity, the hydrous cobalt-iridium oxide nanoframes exhibited similar retention of initial OER mass activity (70 % retention) as commercial IrO<sub>2</sub> (71 % retention) tested using an accelerated durability testing protocol. The hydrous cobalt-iridium oxide nanoframes catalyst showed a higher Ir dissolution rate compared with IrO<sub>2</sub>; however, the specific activity of CoIr300-CL<sub>EO</sub> also increased indicating that the catalyst sites may become more active which contributes to the similar OER stability of CoIr300-CL<sub>EO</sub> compared with IrO<sub>2</sub> under the ADT testing conditions.

The effects of heat treatment temperature on the structural and electrochemical properties of CoIr-based catalysts were also studied. Scanning electron microscopy images showed that the catalysts treated with different temperatures have similar porous morphologies. Energy Dispersive X-ray Spectroscopy elemental mapping revealed that Co and Ir are homogeneously distributed. Additionally, CoIr200-CL and CoIr300-CL

have similar Ir:Co:O atomic ratios, and CoIr400-CL has higher relative amount of Co and O. X-ray diffraction showed that the peak position of the metallic Ir (111) was shifted to higher  $2\theta$  values as the temperature increased which supported a lattice compression due to the incorporation of cobalt. The peak width of the Ir (111) peak became smaller as the temperature increased which indicated an increase in the particle size.

Significant changes in the electrochemical measurements were also observed for the catalysts thermal treated at different temperature. The calculated  $\text{ECSA}_{\text{Ir,CO}}$  was reduced with increasing treatment temperature. After an electrochemical oxidation protocol, the  $\text{ECSA}_{\text{IrO}_2}$  value of catalysts exhibited a similar trend. The CoIr300-CL<sub>EO</sub> catalyst showed the best mass activity and specific activity among the catalysts treated at 200, 300 and 400 °C. The significantly higher OER activity of the CoIr300-CL<sub>EO</sub> catalyst may result from the presence of high density and distinct structure of Ir-OH surface species and/or enhanced interaction of Ir with Co within the structure. After ADT protocol, CoIr300-CL<sub>ADT</sub> also showed the best activity and the highest retention of the initial  $\text{ECSA}_{\text{IrO}_2}$  and activity. Interestingly, the OER specific activity of CoIr200-CL<sub>ADT</sub> and CoIr300-CL<sub>ADT</sub> increased while the  $\text{ECSA}_{\text{IrO}_2}$  of CoIr200-CL<sub>ADT</sub> and CoIr300-CL<sub>ADT</sub> decreased compared with the catalysts before ADT. The specific activity increase for CoIr200-CL<sub>ADT</sub> and CoIr300-CL<sub>ADT</sub> may come from redistribution of Co and Ir during the ADT, leading to modification of the electron density distribution around the active sites. Additionally, the increase of hydroxide/oxide species ratio may contribute to improving the specific activity. The Tafel slopes after ADT exhibited same trend as the specific activity, suggesting no significant change in reaction mechanism. The major loss in the stability occurred when the temperature was increased to 400 °C. The large drop of

the specific activity of CoIr400-CL<sub>ADT</sub> can be related to the high Co and O ratio (Ir:Co:O of 1:0.4:2) relative to Ir. Iridium dissolution was considered to be the main factor of mass activity loss. Cobalt is unstable in acidic and high potential environments, and iridium connected to cobalt may exhibit enhanced dissolution under these conditions. Particle coalescence may also contribute to the low specific activity of CoIr400-CL<sub>ADT</sub>. The ECSA<sub>IrO<sub>2</sub></sub> of the catalysts decreased, and consequently, the mass activity of the catalysts decreasing after ADT. Particle agglomeration can result in reduced active sites and poor mass transport to the catalyst surface.

This work supports that bimetallic structures may be able to provide higher activity and similar stability compared to commercial IrO<sub>2</sub>. The heat treatment temperatures can significantly affect the morphological and structural properties of cobalt-iridium based catalyst and its activity and durability toward oxygen evolution reaction.

## V. FUTURE RESEARCH DIRECTIONS

The CoIr catalysts studied for OER underwent an electrochemical oxidation (EO) step before RDE tests. However, the morphology and atomic structure on the surface of the catalysts after electrochemical oxidation and after ADT remain unclear. Therefore, this study suggests the following research directions. First, investigation of the morphology and atomic structure of final catalysts using scanning transmission electron microscopy (STEM). The information on elemental distribution, phase segregation and lattice spacing of the catalysts after EO and ADT treated with different temperatures can be obtained using STEM combined with high angle annular dark-field scanning transmission electron microscopy (HAADF-STEM), energy dispersive X-ray spectroscopy (EDX), and tomography STEM. The variations on structure can be used to further explain the surface structure and catalytic performance of the catalysts.

Second, to study the effect of the interaction of cobalt with iridium on surface structure, X-ray photoelectron spectroscopy (XPS) can be used to identify and perform semi-quantitative analysis of chemical species within the surface region of the catalysts and evaluate the effects of temperature on the surface structure. The XPS signal intensity mostly arises from the top few nanometers of the surface. There are three major things that can be obtained from XPS analysis: 1) the presence and relative atomic percentages of metallic, oxide, and hydroxide surface species; 2) peak fitting analysis of the XPS spectrum after EO and ADT in the Ir 4f, Co 2p, and O 1s spectral regions to obtain binding energies, relative areas; and 3) relative weight and atomic percentages of iridium, cobalt, oxygen within the surface region of catalysts after EO and ADT.

## LITERATURE CITED

1. Gurney, J.; Petroleum Company, B., *BP Statistical Review of World Energy*. 2005; Vol. 4, p 283.
2. Ibrahim, H.; Ilinca, A.; Perron, J., Energy storage systems—Characteristics and comparisons. *Renew. Sust. Energ. Rev* **2008**, *12* (5), 1221-1250.
3. Rashid, M.; Al Mesfer, M.; Naseem, H.; Danish, M., *Hydrogen Production by Water Electrolysis: A Review of Alkaline Water Electrolysis, PEM Water Electrolysis and High Temperature Water Electrolysis*. 2015; Vol. ISSN, p 2249-8958.
4. LeRoy, R. L., Industrial water electrolysis: Present and future. *International Journal of Hydrogen Energy* **1983**, *8* (6), 401-417.
5. Abdol Rahim, A. H.; Tijani, A. S.; Kamarudin, S. K.; Hanapi, S., An overview of polymer electrolyte membrane electrolyzer for hydrogen production: Modeling and mass transport. *Journal of Power Sources* **2016**, *309*, 56-65.
6. Hydrogen Production From Water Electrolysis: Current Status and Future Trends. *Proceedings of the IEEE, Proc. IEEE* **2012**, (2), 410.
7. Butler, A.; Spliethoff, H., Current status of water electrolysis for energy storage, grid balancing and sector coupling via power-to-gas and power-to-liquids: A review. *Renewable and Sustainable Energy Reviews* **2018**, *82* (Part 3), 2440-2454.
8. Bernt, M.; Hartig-Weiß, A.; Tovini, M. F.; El-Sayed, H. A.; Schramm, C.; Schröter, J.; Gebauer, C.; Gasteiger, H. A. J. C. I. T., Current Challenges in Catalyst Development for PEM Water Electrolyzers. **2019**.
9. Meyer, T. J., The art of splitting water. *Nature* **2008**, *451*, 778.

10. Katsounaros, I.; Cherevko, S.; Zeradjanin, A. R.; Mayrhofer, K. J., Oxygen electrochemistry as a cornerstone for sustainable energy conversion. *Angew Chem Int Ed Engl* **2014**, *53* (1), 102-21.
11. Spöri, C.; Kwan, J. T. H.; Bonakdarpour, A.; Wilkinson, D. P.; Strasser, P., The Stability Challenges of Oxygen Evolving Catalysts: Towards a Common Fundamental Understanding and Mitigation of Catalyst Degradation. **2017**, *56* (22), 5994-6021.
12. Over, H., Surface Chemistry of Ruthenium Dioxide in Heterogeneous Catalysis and Electrocatalysis: From Fundamental to Applied Research. *Chemical Reviews* **2012**, *112* (6), 3356-3426.
13. Rossmeisl, J.; Logadottir, A.; Nørskov, J. K., Electrolysis of water on (oxidized) metal surfaces. *Chemical Physics* **2005**, *319* (1), 178-184.
14. Rossmeisl, J.; Qu, Z. W.; Zhu, H.; Kroes, G. J.; Nørskov, J. K., Electrolysis of water on oxide surfaces. *J. Electroanal. Chem.* **2007**, *607* (1), 83-89.
15. Bockris, J. O. M., Kinetics of Activation Controlled Consecutive Electrochemical Reactions: Anodic Evolution of Oxygen. **1956**, *24* (4), 817-827.
16. Doyle, R. L.; Lyons, M. E. G., The Oxygen Evolution Reaction: Mechanistic Concepts and Catalyst Design. In *Photoelectrochemical Solar Fuel Production: From Basic Principles to Advanced Devices*, Giménez, S.; Bisquert, J., Eds. Springer International Publishing: Cham, 2016; pp 41-104.
17. Dau, H.; Risch, M.; Limberg, C.; Roggan, S.; Reier, T.; Strasser, P., The Mechanism of Water Oxidation: From Electrolysis via Homogeneous to Biological Catalysis. *ChemCatChem* **2010**, *2* (7), 724-761.

18. Danilovic, N.; Subbaraman, R.; Chang, K.-C.; Chang, S. H.; Kang, Y. J.; Snyder, J.; Paulikas, A. P.; Strmcnik, D.; Kim, Y.-T.; Myers, D.; Stamenkovic, V. R.; Markovic, N. M., Activity–Stability Trends for the Oxygen Evolution Reaction on Monometallic Oxides in Acidic Environments. *The Journal of Physical Chemistry Letters* **2014**, *5* (14), 2474-2478.
19. Miles, M., *Periodic Variations of Overvoltages for Water Electrolysis in Acid Solutions from Cyclic Voltammetric Studies*. 1976; Vol. 123.
20. Reier, T.; Oezaslan, M.; Strasser, P., Electrocatalytic Oxygen Evolution Reaction (OER) on Ru, Ir, and Pt Catalysts: A Comparative Study of Nanoparticles and Bulk Materials. *ACS Catalysis* **2012**, *2* (8), 1765-1772.
21. Reier, T.; Nong, H. N.; Teschner, D.; Schlögl, R.; Strasser, P., Electrocatalytic Oxygen Evolution Reaction in Acidic Environments – Reaction Mechanisms and Catalysts. **2017**, *7* (1), 1601275.
22. Cherevko, S.; Zeradjanin, A. R.; Topalov, A. A.; Kulyk, N.; Katsounaros, I.; Mayrhofer, K. J. J., Dissolution of Noble Metals during Oxygen Evolution in Acidic Media. *ChemCatChem* **2014**, *6* (8), 2219-2223.
23. Trasatti, S., Electrocatalysis by oxides — Attempt at a unifying approach. *Journal of Electroanalytical Chemistry and Interfacial Electrochemistry* **1980**, *111* (1), 125-131.
24. Lee, Y.; Suntivich, J.; May, K. J.; Perry, E. E.; Shao-Horn, Y., Synthesis and Activities of Rutile IrO<sub>2</sub> and RuO<sub>2</sub> Nanoparticles for Oxygen Evolution in Acid and Alkaline Solutions. *J. Phys. Chem. Lett.* **2012**, *3* (3), 399-404.

25. Cherevko, S.; Geiger, S.; Kasian, O.; Kulyk, N.; Grote, J.-P.; Savan, A.; Shrestha, B. R.; Merzlikin, S.; Breitbach, B.; Ludwig, A.; Mayrhofer, K. J. J., Oxygen and hydrogen evolution reactions on Ru, RuO<sub>2</sub>, Ir, and IrO<sub>2</sub> thin film electrodes in acidic and alkaline electrolytes: A comparative study on activity and stability. *Catal. Today* **2016**, *262*, 170-180.
26. Rogers, D. B.; Shannon, R. D.; Sleight, A. W.; Gillson, J. L., Crystal chemistry of metal dioxides with rutile-related structures. *Inorganic Chemistry* **1969**, *8* (4), 841-849.
27. Hackwood, S.; Schiavone, L. M.; Dautremont-Smith, W. C.; Beni, G., Anodic Evolution of Oxygen on Sputtered Iridium Oxide Films. **1981**, *128* (12), 2569-2573.
28. Carmo, M.; Fritz, D. L.; Mergel, J.; Stolten, D., A comprehensive review on PEM water electrolysis. *International Journal of Hydrogen Energy* **2013**, *38* (12), 4901-4934.
29. Antolini, E.; Gonzalez, E. R., Ceramic materials as supports for low-temperature fuel cell catalysts. *Solid State Ionics* **2009**, *180* (9), 746-763.
30. Huang, S.-Y.; Ganesan, P.; Jung, H.-Y.; Popov, B. N., Development of supported bifunctional oxygen electrocatalysts and corrosion-resistant gas diffusion layer for unitized regenerative fuel cell applications. *Journal of Power Sources* **2012**, *198*, 23-29.
31. Fuentes, R. E.; Farrell, J.; Weidner, J. W., Multimetallic Electrocatalysts of Pt, Ru, and Ir Supported on Anatase and Rutile TiO<sub>2</sub> for Oxygen Evolution in an Acid Environment. **2011**, *14* (3), E5-E7.

32. Oakton, E.; Lebedev, D.; Povia, M.; Abbott, D. F.; Fabbri, E.; Fedorov, A.; Nachttegaal, M.; Copéret, C.; Schmidt, T. J., IrO<sub>2</sub>-TiO<sub>2</sub>: A High-Surface-Area, Active, and Stable Electrocatalyst for the Oxygen Evolution Reaction. *ACS Catalysis* **2017**, *7* (4), 2346-2352.
33. Fuentes, R. E.; Rau, S.; Smolinka, T.; Weidner, J. W., Bimetallic Electrocatalysts Supported on TiO<sub>2</sub> for PEM Water Electrolyzer. **2010**, *28* (26), 23-35.
34. Bernsmeier, D.; Bernicke, M.; Schmack, R.; Sachse, R.; Paul, B.; Bergmann, A.; Strasser, P.; Ortel, E.; Kraehnert, R., Oxygen Evolution Catalysts Based on Ir-Ti Mixed Oxides with Templated Mesopore Structure: Impact of Ir on Activity and Conductivity. *ChemSusChem* **2018**, *11* (14), 2367-2374.
35. Mazúr, P.; Polonský, J.; Paidar, M.; Bouzek, K., Non-conductive TiO<sub>2</sub> as the anode catalyst support for PEM water electrolysis. *International Journal of Hydrogen Energy* **2012**, *37* (17), 12081-12088.
36. García, B. L.; Fuentes, R.; Weidner, J. W., Low-Temperature Synthesis of a PtRu/Nb<sub>0.1</sub>Ti<sub>0.9</sub>O<sub>2</sub> Electrocatalyst for Methanol Oxidation. **2007**, *10* (7), B108-B110.
37. Oh, H.-S.; Nong, H. N.; Reier, T.; Bergmann, A.; Gliech, M.; Ferreira de Araújo, J.; Willinger, E.; Schlögl, R.; Teschner, D.; Strasser, P., Electrochemical Catalyst–Support Effects and Their Stabilizing Role for IrO<sub>x</sub> Nanoparticle Catalysts during the Oxygen Evolution Reaction. *Journal of the American Chemical Society* **2016**, *138* (38), 12552-12563.

38. Reier, T.; Pawolek, Z.; Cherevko, S.; Bruns, M.; Jones, T.; Teschner, D.; Selve, S.; Bergmann, A.; Nong, H. N.; Schlögl, R.; Mayrhofer, K. J. J.; Strasser, P., Molecular Insight in Structure and Activity of Highly Efficient, Low-Ir Ir–Ni Oxide Catalysts for Electrochemical Water Splitting (OER). *Journal of the American Chemical Society* **2015**, *137* (40), 13031-13040.
39. Halck, N. B.; Petrykin, V.; Krtil, P.; Rossmeisl, J., Beyond the volcano limitations in electrocatalysis – oxygen evolution reaction. *Physical Chemistry Chemical Physics* **2014**, *16* (27), 13682-13688.
40. Nong, H. N.; Gan, L.; Willinger, E.; Teschner, D.; Strasser, P., IrOx core-shell nanocatalysts for cost- and energy-efficient electrochemical water splitting. *Chemical Science* **2014**, *5* (8), 2955-2963.
41. Kwon, T.; Hwang, H.; Sa, Y. J.; Park, J.; Baik, H.; Joo, S. H.; Lee, K., Cobalt Assisted Synthesis of IrCu Hollow Octahedral Nanocages as Highly Active Electrocatalysts toward Oxygen Evolution Reaction. **2017**, *27* (7), 1604688.
42. Fu, L.; Cai, P.; Cheng, G.; Luo, W., Colloidal synthesis of iridium-iron nanoparticles for electrocatalytic oxygen evolution. *Sustainable Energy & Fuels* **2017**, *1* (5), 1199-1203.
43. Park, S.-A.; Kim, K.-S.; Kim, Y.-T., Electrochemically Activated Iridium Oxide Black as Promising Electrocatalyst Having High Activity and Stability for Oxygen Evolution Reaction. *ACS Energy Letters* **2018**, *3* (5), 1110-1115.
44. Lim, J.; Yang, S.; Kim, C.; Roh, C.-W.; Kwon, Y.; Kim, Y.-T.; Lee, H., Shaped Ir–Ni bimetallic nanoparticles for minimizing Ir utilization in oxygen evolution reaction. *Chemical Communications* **2016**, *52* (32), 5641-5644.

45. Nong, H. N.; Oh, H.-S.; Reier, T.; Willinger, E.; Willinger, M.-G.; Petkov, V.; Teschner, D.; Strasser, P., Oxide-Supported IrNiOx Core–Shell Particles as Efficient, Cost-Effective, and Stable Catalysts for Electrochemical Water Splitting. **2015**, *54* (10), 2975-2979.
46. Corona-Guinto, J. L.; Cardeño-García, L.; Martínez-Casillas, D. C.; Sandoval-Pineda, J. M.; Tamayo-Meza, P.; Silva-Casarin, R.; González-Huerta, R. G., Performance of a PEM electrolyzer using RuIrCoOx electrocatalysts for the oxygen evolution electrode. *International Journal of Hydrogen Energy* **2013**, *38* (28), 12667-12673.
47. Zaman, W. Q.; Wang, Z.; Sun, W.; Zhou, Z.; Tariq, M.; Cao, L.; Gong, X.-Q.; Yang, J., Ni–Co Codoping Breaks the Limitation of Single-Metal-Doped IrO<sub>2</sub> with Higher Oxygen Evolution Reaction Performance and Less Iridium. *ACS Energy Letters* **2017**, *2* (12), 2786-2793.
48. Zhang, Y.; Wu, C.; Jiang, H.; Lin, Y.; Liu, H.; He, Q.; Chen, S.; Duan, T.; Song, L., Atomic Iridium Incorporated in Cobalt Hydroxide for Efficient Oxygen Evolution Catalysis in Neutral Electrolyte. *Advanced materials (Deerfield Beach, Fla.)* **2018**, *30* (18), e1707522.
49. Petrykin, V.; Bastl, Z.; Franc, J.; Macounova, K.; Makarova, M.; Mukerjee, S.; Ramaswamy, N.; Spirovova, I.; Krtil, P., Local Structure of Nanocrystalline Ru<sub>1-x</sub>Ni<sub>x</sub>O<sub>2-δ</sub> Dioxide and Its Implications for Electrocatalytic Behavior—An XPS and XAS Study. *The Journal of Physical Chemistry C* **2009**, *113* (52), 21657-21666.

50. Sun, W.; Song, Y.; Gong, X.-Q.; Cao, L.-m.; Yang, J., An efficiently tuned d-orbital occupation of IrO<sub>2</sub> by doping with Cu for enhancing the oxygen evolution reaction activity. *Chemical Science* **2015**, *6* (8), 4993-4999.
51. González-Huerta, R. G.; Ramos-Sánchez, G.; Balbuena, P. B., Oxygen evolution in Co-doped RuO<sub>2</sub> and IrO<sub>2</sub>: Experimental and theoretical insights to diminish electrolysis overpotential. *Journal of Power Sources* **2014**, *268*, 69-76.
52. Feng, J.; Lv, F.; Zhang, W.; Li, P.; Wang, K.; Yang, C.; Wang, B.; Yang, Y.; Zhou, J.; Lin, F.; Wang, G.-C.; Guo, S., Iridium-Based Multimetallic Porous Hollow Nanocrystals for Efficient Overall-Water-Splitting Catalysis. *Adv. Mater.* **2017**, *29* (47), 1703798.
53. Arán-Ais, R. M.; Solla-Gullón, J.; Gocyla, M.; Heggen, M.; Dunin-Borkowski, R. E.; Strasser, P.; Herrero, E.; Feliu, J. M., The effect of interfacial pH on the surface atomic elemental distribution and on the catalytic reactivity of shape-selected bimetallic nanoparticles towards oxygen reduction. *Nano Energy* **2016**, *27*, 390-401.
54. Stamenkovic, V. R.; Mun, B. S.; Mayrhofer, K. J.; Ross, P. N.; Markovic, N. M., Effect of surface composition on electronic structure, stability, and electrocatalytic properties of Pt-transition metal alloys: Pt-skin versus Pt-skeleton surfaces. *J Am Chem Soc* **2006**, *128* (27), 8813-9.
55. Luc, W.; Jiao, F., Nanoporous Metals as Electrocatalysts: State-of-the-Art, Opportunities, and Challenges. *ACS Catalysis* **2017**, *7* (9), 5856-5861.
56. Tian, N.; Zhou, Z. Y.; Sun, S. G.; Ding, Y.; Wang, Z. L., Synthesis of tetrahedral platinum nanocrystals with high-index facets and high electro-oxidation activity. *Science* **2007**, *316* (5825), 732-5.

57. Godínez-Salomón, F.; Albiter, L.; Alia, S. M.; Pivovar, B. S.; Camacho-Forero, L. E.; Balbuena, P. B.; Mendoza-Cruz, R.; Arellano-Jimenez, M. J.; Rhodes, C. P., Self-Supported Hydrous Iridium–Nickel Oxide Two-Dimensional Nanoframes for High Activity Oxygen Evolution Electrocatalysts. *ACS Catalysis* **2018**, *8* (11), 10498-10520.
58. Hu, W.; Zhong, H.; Liang, W.; Chen, S., Ir-Surface enriched porous Ir-Co oxide hierarchical architecture for high performance water oxidation in acidic media. *ACS applied materials & interfaces* **2014**, *6* (15), 12729-36.
59. Xu, S.; Chen, S.; Tian, L.; Xia, Q.; Hu, W., Selective-leaching method to fabricate an Ir surface-enriched Ir-Ni oxide electrocatalyst for water oxidation. *Journal of Solid State Electrochemistry* **2016**, *20* (7), 1961-1970.
60. Alia, S. M.; Shulda, S.; Ngo, C.; Pylypenko, S.; Pivovar, B. S., Iridium-Based Nanowires as Highly Active, Oxygen Evolution Reaction Electrocatalysts. *ACS Catalysis* **2018**, *8* (3), 2111-2120.
61. Godínez-Salomón, F.; Albiter, L.; Mendoza-Cruz, R.; Rhodes, C. P., Bimetallic Two-Dimensional Nanoframes: High Activity Acidic Bifunctional Oxygen Reduction and Evolution Electrocatalysts. *ACS Applied Energy Materials* **2020**, *3* (3), 2404-2421.
62. da Silva, G. C.; Fernandes, M. R.; Ticianelli, E. A., Activity and Stability of Pt/IrO<sub>2</sub> Bifunctional Materials as Catalysts for the Oxygen Evolution/Reduction Reactions. *ACS Catalysis* **2018**, *8* (3), 2081-2092.
63. Ahmadi, M.; Behafarid, F.; Cui, C.; Strasser, P.; Cuenya, B. R., Long-Range Segregation Phenomena in Shape-Selected Bimetallic Nanoparticles: Chemical State Effects. *ACS Nano* **2013**, *7* (10), 9195-9204.

64. Zhao, Z.; Wang, F.-H.; Fisher, A.; Shen, Y.; Cheng, D., Phase stability and segregation behavior of nickel-based nanoalloys based on theory and simulation. *J. Alloys Compd.* **2017**, *708*, 1150-1160.
65. Guisbiers, G.; Mendoza-Pérez, R.; Bazán-Díaz, L.; Mendoza-Cruz, R.; Velázquez-Salazar, J. J.; José-Yacamán, M., Size and Shape Effects on the Phase Diagrams of Nickel-Based Bimetallic Nanoalloys. *The Journal of Physical Chemistry C* **2017**, *121* (12), 6930-6939.
66. Reier, T.; Teschner, D.; Lunkenbein, T.; Bergmann, A.; Selve, S.; Kraehnert, R.; Schlögl, R.; Strasser, P., Electrocatalytic Oxygen Evolution on Iridium Oxide: Uncovering Catalyst-Substrate Interactions and Active Iridium Oxide Species. **2014**, *161* (9), F876-F882.
67. Chandra, D.; Takama, D.; Masaki, T.; Sato, T.; Abe, N.; Togashi, T.; Kurihara, M.; Saito, K.; Yui, T.; Yagi, M. J. A. C., Highly Efficient Electrocatalysis and Mechanistic Investigation of Intermediate IrO<sub>x</sub>(OH)<sub>y</sub> Nanoparticle Films for Water Oxidation. **2016**, *6* (6), 3946-3954.
68. Xu, W.; Haarberg, G. M.; Sunde, S.; Seland, F.; Ratvik, A. P.; Zimmerman, E.; Shimamune, T.; Gustavsson, J.; Åkre, T., Calcination Temperature Dependent Catalytic Activity and Stability of IrO<sub>2</sub>-Ta<sub>2</sub>O<sub>5</sub> Anodes for Oxygen Evolution Reaction in Aqueous Sulfate Electrolytes. *Journal of The Electrochemical Society* **2017**, *164* (9), F895-F900.
69. Cherevko, S., Stability and dissolution of electrocatalysts: Building the bridge between model and "real world" systems. *Curr. Opin. Electrochem.* **2018**, *8*, 118-125.

70. Spori, C.; Kwan, J. T. H.; Bonakdarpour, A.; Wilkinson, D. P.; Strasser, P., The Stability Challenges of Oxygen Evolving Catalysts: Towards a Common Fundamental Understanding and Mitigation of Catalyst Degradation. *Angew. Chem.-Int. Edit.* **2017**, *56* (22), 5994-6021.
71. Alia, S. M.; Hurst, K. E.; Kocha, S. S.; Pivovar, B. S., Mercury Underpotential Deposition to Determine Iridium and Iridium Oxide Electrochemical Surface Areas. **2016**, *163* (11), F3051-F3056.
72. Yu, A.; Lee, C.; Kim, M. H.; Lee, Y., Nanotubular Iridium–Cobalt Mixed Oxide Crystalline Architectures Inherited from Cobalt Oxide for Highly Efficient Oxygen Evolution Reaction Catalysis. *ACS Applied Materials & Interfaces* **2017**, *9* (40), 35057-35066.
73. Karimi, F.; Bazylak, A.; Peppley, B. A., Effect of Calcination Temperature on the Morphological and Electrochemical Characteristics of Supported Iridium Hydroxyoxide Electrocatalysts for the PEM Electrolyzer Anode. *Journal of The Electrochemical Society* **2017**, *164* (4), F464-F474.
74. Bragg, W. L., *The Crystalline State: Volume I*. The Macmillan Company: New York, 1934.
75. Ashcroft, N. W., *Solid state physics*. Holt, Rinehart and Winston: New York, 1976.
76. Patterson, A. L., The Scherrer Formula for X-Ray Particle Size Determination. *Physical Review* **1939**, *56* (10), 978-982.

77. Denuault, G.; Sosna, M.; Williams, K.-J., 11 - Classical Experiments. In *Handbook of Electrochemistry*, Zoski, C. G., Ed. Elsevier: Amsterdam, 2007; pp 431-469.
78. Albery, W. J., *Ring-disc electrodes [by] W. J. Albery and M. L. Hitchman*. Clarendon Press: Oxford, 1971.
79. Nikolic, J.; Expósito, E.; Iniesta, J.; González-García, J.; Montiel, V., Theoretical Concepts and Applications of a Rotating Disk Electrode. *Journal of Chemical Education* **2000**, 77 (9), 1191.
80. Elgrishi, N.; Rountree, K. J.; McCarthy, B. D.; Rountree, E. S.; Eisenhart, T. T.; Dempsey, J. L., A Practical Beginner's Guide to Cyclic Voltammetry. *Journal of Chemical Education* **2018**, 95 (2), 197-206.
81. Costentin, C.; Saveant, J.-M., Cyclic Voltammetry Analysis of Electrocatalytic Films. *The Journal of Physical Chemistry C* **2015**, 119 (22), 12174-12182.
82. Offer, G.; Kucernak, A., Calculating the coverage of saturated and sub-saturated layers of carbon monoxide adsorbed onto platinum. *Journal of Electroanalytical Chemistry* **2008**, 613 (2), 171-185.
83. Grgur, B. N.; Markovic, N. M.; Lucas, C. A.; ROSS, P. N., Electrochemical oxidation of carbon monoxide: from platinum single crystals to low temperature fuel cells catalysts. Part I: Carbon monoxide oxidation onto low index platinum single crystals. *Journal of the Serbian Chemical Society* **2001**, 66 (11-12), 785-797.
84. Trasatti, S., Electrocatalysis in the anodic evolution of oxygen and chlorine. *Electrochimica Acta* **1984**, 29 (11), 1503-1512.

85. Grupioni, A. A. F.; Arashiro, E.; Lassali, T. A. F., Voltammetric characterization of an iridium oxide-based system: the pseudocapacitive nature of the Ir<sub>0.3</sub>Mn<sub>0.7</sub>O<sub>2</sub> electrode. *Electrochimica Acta* **2002**, *48* (4), 407-418.
86. Zhao, S.; Yu, H.; Maric, R.; Danilovic, N.; Capuano, C. B.; Ayers, K. E.; Mustain, W. E., Calculating the Electrochemically Active Surface Area of Iridium Oxide in Operating Proton Exchange Membrane Electrolyzers. **2015**, *162* (12), F1292-F1298.
87. Doyle, R. L.; Lyons, M. E., The oxygen evolution reaction: mechanistic concepts and catalyst design. In *Photoelectrochemical solar fuel production*, Springer: 2016; pp 41-104.
88. Guidelli, R.; Compton, R. G.; Feliu, J. M.; Gileadi, E.; Lipkowsky, J.; Schmickler, W.; Trasatti, S., Defining the transfer coefficient in electrochemistry: An assessment (IUPAC Technical Report). *Pure and Applied Chemistry* **2014**, *86* (2), 245-258.
89. Godínez-Salomón, F.; Mendoza-Cruz, R.; Arellano-Jimenez, M. J.; Jose-Yacaman, M.; Rhodes, C. P., Metallic Two-Dimensional Nanoframes: Unsupported Hierarchical Nickel–Platinum Alloy Nanoarchitectures with Enhanced Electrochemical Oxygen Reduction Activity and Stability. *ACS applied materials & interfaces* **2017**, *9* (22), 18660-18674.
90. El-Sayed, H.; Weiß, A.; Olbrich, L.; Putro, G.; Gasteiger, H., OER Catalyst Stability Investigation Using RDE Technique: A Stability Measure or an Artifact? *Journal of The Electrochemical Society* **2019**, *166*, F458-F464.

91. Godínez-Salomón, F.; Albiter, L.; Alia, S. M.; Pivovar, B. S.; Camacho-Forero, L. E.; Balbuena, P. B.; Mendoza-Cruz, R.; Arellano-Jimenez, M. J.; Rhodes, C. P., Self-Supported Hydrous Iridium–Nickel Oxide Two-Dimensional Nanoframes for High Activity Oxygen Evolution Electrocatalysts. *ACS Catal.* **2018**, *8* (11), 10498-10520.
92. Rolison, D. R., Catalytic Nanoarchitectures--the Importance of Nothing and the Unimportance of Periodicity. *Science* **2003**, *299* (5613), 1698.
93. Zhao, S.; Yu, H.; Maric, R.; Danilovic, N.; Capuano, C. B.; Ayers, K. E.; Mustain, W. E., Calculating the Electrochemically Active Surface Area of Iridium Oxide in Operating Proton Exchange Membrane Electrolyzers. *J. Electrochem. Soc.* **2015**, *162* (12), F1292-F1298.
94. Parsons, R., Atlas of electrochemical equilibria in aqueous solutions: by Marcel Pourbaix, Pergamon Press, Oxford etc, Cebelcor, Brussels, 1966, 644 pages, £ 12. Elsevier: 1967.
95. Oh, H.-S.; Nong, H. N.; Reier, T.; Bergmann, A.; Gliech, M.; Ferreira de Araújo, J.; Willinger, E.; Schlögl, R.; Teschner, D.; Strasser, P., Electrochemical Catalyst–Support Effects and Their Stabilizing Role for IrOx Nanoparticle Catalysts during the Oxygen Evolution Reaction. *J. Am. Chem. Soc.* **2016**, *138* (38), 12552-12563.
96. Yang, J.; Liu, H. W.; Martens, W. N.; Frost, R. L., Synthesis and Characterization of Cobalt Hydroxide, Cobalt Oxyhydroxide, and Cobalt Oxide Nanodiscs. *J. Phys. Chem. C* **2010**, *114* (1), 111-119.

97. Godinez-Salomon, F.; Mendoza-Cruz, R.; Arellano-Jimenez, M. J.; Jose-Yacaman, M.; Rhodes, C. P., Metallic Two-Dimensional Nanoframes: Unsupported Hierarchical Nickel-Platinum Alloy Nanoarchitectures with Enhanced Electrochemical Oxygen Reduction Activity and Stability. *ACS Appl. Mater. Interfaces* **2017**, *9* (22), 18660-18674.
98. Hall, D. S.; Lockwood, D. J.; Bock, C.; MacDougall, B. R., Nickel hydroxides and related materials: a review of their structures, synthesis and properties. *P ROY SOC A-MATH PHY* **2015**, *471* (2174), 65.
99. Yin, H. J.; Tang, Z. Y., Ultrathin two-dimensional layered metal hydroxides: an emerging platform for advanced catalysis, energy conversion and storage. *Chem. Soc. Rev.* **2016**, *45* (18), 4873-4891.
100. Zaman, W. Q.; Wang, Z.; Sun, W.; Zhou, Z.; Tariq, M.; Cao, L.; Gong, X.-Q.; Yang, J., Ni-Co Codoping Breaks the Limitation of Single-Metal-Doped IrO<sub>2</sub> with Higher Oxygen Evolution Reaction Performance and Less Iridium. *ACS Energy Lett.* **2017**, *2* (12), 2786-2793.
101. Klarstrom, D.; Crook, P.; Sharif, A., Cobalt Alloys: Alloying and Thermomechanical Processing. In *Reference Module in Materials Science and Materials Engineering*, 2017.
102. Makhlof, S. A.; Bakr, Z. H.; Aly, K. I.; Moustafa, M. S., Structural, electrical and optical properties of Co<sub>3</sub>O<sub>4</sub> nanoparticles. *Superlattices Microstruct.* **2013**, *64*, 107-117.

103. Salavati-Niasari, M.; Khansari, A.; Davar, F., Synthesis and characterization of cobalt oxide nanoparticles by thermal treatment process. *Inorg. Chim. Acta* **2009**, *362* (14), 4937-4942.
104. Music, S.; Popovic, S.; Maljkovic, M.; Skoko, Z.; Furic, K.; Gajovic, A., Thermochemical formation of IrO<sub>2</sub> and Ir. *Mater. Lett.* **2003**, *57* (29), 4509-4514.
105. Cherevko, S.; Geiger, S.; Kasian, O.; Mingers, A.; Mayrhofer, K. J. J., Oxygen evolution activity and stability of iridium in acidic media. Part 1. – Metallic iridium. *J. Electroanal. Chem.* **2016**, *773*, 69-78.
106. Abbott, D. F.; Lebedev, D.; Waltar, K.; Povia, M.; Nachtegaal, M.; Fabbri, E.; Copéret, C.; Schmidt, T. J., Iridium Oxide for the Oxygen Evolution Reaction: Correlation between Particle Size, Morphology, and the Surface Hydroxo Layer from Operando XAS. *Chem. Mater.* **2016**, *28* (18), 6591-6604.
107. Cherevko, S.; Geiger, S.; Kasian, O.; Mingers, A.; Mayrhofer, K. J. J., Oxygen evolution activity and stability of iridium in acidic media. Part 2. – Electrochemically grown hydrous iridium oxide. *J. Electroanal. Chem.* **2016**, *774*, 102-110.
108. Steegstra, P.; Busch, M.; Panas, I.; Ahlberg, E., Revisiting the Redox Properties of Hydrous Iridium Oxide Films in the Context of Oxygen Evolution. *J. Phys. Chem. C* **2013**, *117* (40), 20975-20981.
109. Reier, T.; Nong, H. N.; Teschner, D.; Schlögl, R.; Strasser, P., Electrocatalytic Oxygen Evolution Reaction in Acidic Environments – Reaction Mechanisms and Catalysts. *ACS Energy Lett.* **2017**, *7* (1), 1601275.

110. Alia, S. M.; Rasimick, B.; Ngo, C.; Neyerlin, K. C.; Kocha, S. S.; Pylypenko, S.; Xu, H.; Pivovar, B. S., Activity and Durability of Iridium Nanoparticles in the Oxygen Evolution Reaction. *Journal of The Electrochemical Society* **2016**, *163* (11), F3105-F3112.
111. Grupioni, A. A. F.; Arashiro, E.; Lassali, T. A. F., Voltammetric characterization of an iridium oxide-based system: the pseudocapacitive nature of the Ir<sub>0.3</sub>Mn<sub>0.7</sub>O<sub>2</sub> electrode. *Electrochim. Acta* **2002**, *48* (4), 407-418.
112. Koresh, J.; Soffer, A., Double Layer Capacitance and Charging Rate of Ultramicroporous Carbon Electrodes. *J. Electrochem. Soc.* **1977**, *124* (9), 1379-1385.
113. Spöri, C.; Kwan, J. T. H.; Bonakdarpour, A.; Wilkinson, D. P.; Strasser, P., The Stability Challenges of Oxygen Evolving Catalysts: Towards a Common Fundamental Understanding and Mitigation of Catalyst Degradation. *Angew. Chem. Int. Ed.* **2017**, *56* (22), 5994-6021.
114. Doyle, R.; Lyons, M., The Oxygen Evolution Reaction: Mechanistic Concepts and Catalyst Design. In *Photoelectrochemical Solar Fuel Production*, 2016; pp 41-104.
115. Rossmeisl, J.; Qu, Z. W.; Zhu, H.; Kroes, G. J.; Nørskov, J. K., Electrolysis of water on oxide surfaces. *J. Electroanal. Chem.* **2007**, *607* (1), 83-89.
116. Abbott, D. F.; Lebedev, D.; Waltar, K.; Povia, M.; Nachttegaal, M.; Fabbri, E.; Copéret, C.; Schmidt, T. J., Iridium Oxide for the Oxygen Evolution Reaction: Correlation between Particle Size, Morphology, and the Surface Hydroxo Layer from Operando XAS. *Chemistry of Materials* **2016**, *28* (18), 6591-6604.

117. Cherevko, S.; Geiger, S.; Kasian, O.; Mingers, A.; Mayrhofer, K. J. J., Oxygen evolution activity and stability of iridium in acidic media. Part 1. – Metallic iridium. *Journal of Electroanalytical Chemistry* **2016**, *773*, 69-78.
118. Kim, Y. T.; Lopes, P. P.; Park, S. A.; Lee, A. Y.; Lim, J.; Lee, H.; Back, S.; Jung, Y.; Danilovic, N.; Stamenkovic, V.; Erlebacher, J.; Snyder, J.; Markovic, N. M., Balancing activity, stability and conductivity of nanoporous core-shell iridium/iridium oxide oxygen evolution catalysts. *Nat. Commun.* **2017**, *8*, 8.
119. Geiger, S.; Kasian, O.; Ledendecker, M.; Pizzutilo, E.; Mingers, A. M.; Fu, W. T.; Diaz-Morales, O.; Li, Z. Z.; Oellers, T.; Fruchter, L.; Ludwig, A.; Mayrhofer, K. J. J.; Koper, M. T. M.; Cherevko, S., The stability number as a metric for electrocatalyst stability benchmarking. *Nat. Catal.* **2018**, *1* (7), 508-515.
120. Binninger, T.; Mohamed, R.; Waltar, K.; Fabbri, E.; Levecque, P.; Kotz, R.; Schmidt, T. J., Thermodynamic explanation of the universal correlation between oxygen evolution activity and corrosion of oxide catalysts. *Sci Rep* **2015**, *5*, 7.
121. Feng, J.; Lv, F.; Zhang, W.; Li, P.; Wang, K.; Yang, C.; Wang, B.; Yang, Y.; Zhou, J.; Lin, F.; Wang, G.-C.; Guo, S., Iridium-Based Multimetallic Porous Hollow Nanocrystals for Efficient Overall-Water-Splitting Catalysis. **2017**, *29* (47), 1703798.
122. Thommes, M.; Kaneko, K.; Neimark, A. V.; Olivier, J. P.; Rodriguez-Reinoso, F.; Rouquerol, J.; Sing, K. S. W., Physisorption of gases, with special reference to the evaluation of surface area and pore size distribution (IUPAC Technical Report). **2015**, *87* (9-10), 1051.

123. Xiao, H.; Fu, Z.; Chen, K.; Long, Q.; Deng, Y.; Xie, K., Preparation of broccoli-like ferromagnetic cobalt microstructures with superior coercivity via an aqueous reduction strategy. *RSC Advances* **2016**, *6* (70), 66152-66160.
124. Filatov, E. Y.; Cherepanova, S. V.; Kochetygov, I. V.; Shubin, Y. V.; Korenev, S. V., Domain structure of CoIr nanoalloys. *Powder Diffraction* **2017**, *32* (S1), S155-S159.
125. Huy, H. A.; Aradi, B.; Frauenheim, T.; Deák, P., Comparison of Nb- and Ta-doping of anatase TiO<sub>2</sub> for transparent conductor applications. **2012**, *112* (1), 016103.
126. Felix, C.; Maiyalagan, T.; Pasupathi, S.; Bladergroen, B.; Linkov, V., Synthesis, Characterisation and Evaluation of IrO<sub>2</sub> Based Binary Metal Oxide Electrocatalysts for Oxygen Evolution Reaction. *International Journal of Electrochemical Science* **2012**, *7*, 12064-12077.
127. Kuttiyiel, K. A.; Sasaki, K.; Choi, Y.; Su, D.; Liu, P.; Adzic, R. R., Nitride Stabilized PtNi Core–Shell Nanocatalyst for high Oxygen Reduction Activity. *Nano Letters* **2012**, *12* (12), 6266-6271.
128. Strmcnik, D. S.; Tripkovic, D. V.; van der Vliet, D.; Chang, K.-C.; Komanicky, V.; You, H.; Karapetrov, G.; Greeley, J. P.; Stamenkovic, V. R.; Marković, N. M., Unique Activity of Platinum Adislands in the CO Electrooxidation Reaction. *Journal of the American Chemical Society* **2008**, *130* (46), 15332-15339.
129. Cherevko, S.; Geiger, S.; Kasian, O.; Mingers, A.; Mayrhofer, K. J. J., Oxygen evolution activity and stability of iridium in acidic media. Part 2. – Electrochemically grown hydrous iridium oxide. *Journal of Electroanalytical Chemistry* **2016**, *774*, 102-110.

130. Steegstra, P.; Busch, M.; Panas, I.; Ahlberg, E., Revisiting the Redox Properties of Hydrated Iridium Oxide Films in the Context of Oxygen Evolution. *The Journal of Physical Chemistry C* **2013**, *117* (40), 20975-20981.
131. Doyle, R.; Lyons, M., The Oxygen Evolution Reaction: Mechanistic Concepts and Catalyst Design. 2016; pp 41-104.
132. Shinagawa, T.; Garcia-Esparza, A. T.; Takanabe, K., Insight on Tafel slopes from a microkinetic analysis of aqueous electrocatalysis for energy conversion. *Sci Rep* **2015**, *5*, 21.
133. Hu, J.-M.; Zhang, J.-Q.; Cao, C.-N., Oxygen evolution reaction on IrO<sub>2</sub>-based DSA® type electrodes: kinetics analysis of Tafel lines and EIS. *International Journal of Hydrogen Energy* **2004**, *29* (8), 791-797.
134. Feng, J.; Lv, F.; Zhang, W.; Li, P.; Wang, K.; Yang, C.; Wang, B.; Yang, Y.; Zhou, J.; Lin, F.; Wang, G.-C.; Guo, S., Iridium-Based Multimetallic Porous Hollow Nanocrystals for Efficient Overall-Water-Splitting Catalysis. *Adv. Mater.* **2017**, *29* (47), 1703798.
135. Cherevko, S.; Reier, T.; Zeradjanin, A. R.; Pawolek, Z.; Strasser, P.; Mayrhofer, K. J. J., Stability of nanostructured iridium oxide electrocatalysts during oxygen evolution reaction in acidic environment. *Electrochemistry Communications* **2014**, *48*, 81-85.